Mitigation of Harmonic Downmixing Images using Digital Signal Processing Techniques

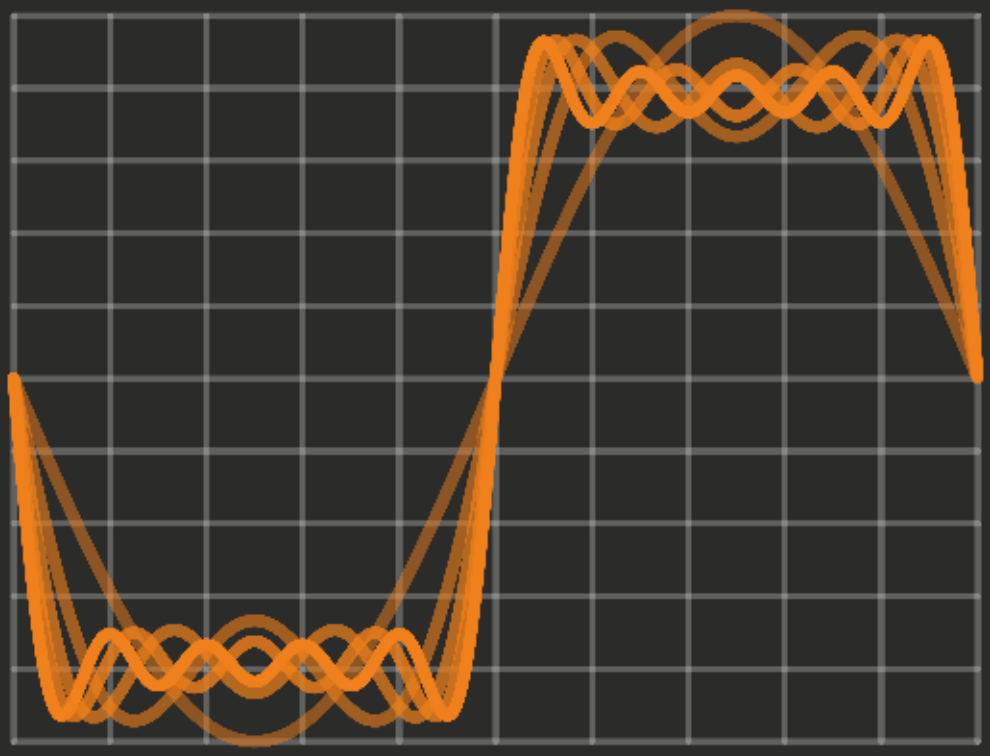

Niels A. Moseley

Mitigation of Harmonic Down-mixing Images using Digital Signal Processing Techniques

Niels A. Moseley

Committee:

Chairman:
Prof.dr.ir. P.G.M. Apers — Universiteit Twente

Secretary:
Prof.dr.ir. P.G.M. Apers — Universiteit Twente

Promotor:
Prof.dr.ir. B. Nauta — Universiteit Twente

Assistant Promotor:
Dr.ing. E.A.M. Klumperink — Universiteit Twente

Members:
Prof.dr.ir. J.W.M. Bergmans — TU Eindhoven
Prof.dr.ir. C.H. Slump — Universiteit Twente
Prof.dr.ir. G.J.M. Smit — Universiteit Twente
Prof.dr.ir. F.E. van Vliet — TNO / Universiteit Twente

CTIT

CTIT Ph.D. Thesis Series No. 14-294
Centre for Telematics and Information Technology
P.O. Box 217, 7500 AE
Enschede, The Netherlands

ISSN 1381-3617
ISBN 978-90-365-3613-4
DOI: 10.3990/1.9789036536134

This work was supported by Freeband/WiComm:
Microelectronics for the Next Generation of Wireless Communication.

Typeset using LaTeX/ MikTex. Vector graphics produced using IPE 7, MATLAB. Bitmap graphics produced by The Gimp and Python/PyCairo.

Printed by: Gildeprint Drukkerijen - www.gildeprint.nl

Mitigation of Harmonic Down-mixing Images using Digital Signal Processing Techniques

DISSERTATION

to obtain
the degree of doctor at the University of Twente,
on the authority of the rector magnificus,
Prof.dr. H. Brinksma,
on account of the decision of the graduation committee,
to be publicly defended
on Thursday January 30th 2014 at 12:45

by

Niels Alexander Moseley

born on the 9th of December 1973
in Alphen aan den Rijn, The Netherlands.

This disseration has been approved by

the promotor,
prof.dr.ir. Bram Nauta

and the assistant promotor,
dr.ing. Eric A. M. Klumperink

Abstract

There is a growing demand for wireless communications at increased data rates. This has necessitated the development of new communication standards. New electronic devices must support a growing number of wireless standards and their various frequency bands, as the new standards do not replace the older ones. Together with the desire for small portable devices, this means that a single-chip solution supporting all existing wireless standards and featuring a wide tuning range, is highly desirable.

The software-defined radio (SDR) concept, where almost all radio functions are implemented in software running on an embedded processor, is purportedly the most promising way to achieve a single-chip design, mainly because software is seen as flexible and extensible. Such a radio would consists of an analog front-end, primarily performing the frequency translation and the relatively large digital embedded processor with associated memory and peripherals.

In receive mode, a frequency synthesizer comprising a high frequency oscillator and programmable digital output divider generates the required wide tuning range. Highly linear switching mixers perform the frequency translation, thereby generating the baseband signals for the embedded processor. However, owing to the pulse-like nature of the synthesizer output and the switching action of the mixer, additional frequency bands are mixed down to baseband together with the desired signal, causing interference. These additional frequency bands, termed *harmonic images* are related to the harmonics of the desired frequency.

In regular receive applications, harmonic image interference corrupts the desired signal causing bit errors to occur. Harmonic images are also problematic in spectral sensing applications; they cause signal energy to be detected when there actually is none.

In narrow-band receivers, harmonic images are avoided by using an external RF filter at the antenna. However, in the wideband systems targeted by this thesis, many such external filters would be needed, making this infeasible for cost sensitive consumer products. A different approach is needed.

This thesis presents a method, based on interference cancelling, to significantly reduce the interference caused by the dominating harmonic image. A harmonic-rejection radio front-end, which offers up to 40 dB of rejection, is used to generate two complex baseband signals. An interference estimate is generated based on these baseband signals. After equalization to remove amplitude and phase differences, the interference estimate is subtracted from the contaminated received signal, thereby

producing a received signal containing less interference. This method was successfully tested using two different front-ends, one built using off-the-shelf components and one fully integrated 65nm CMOS front-end. Using the latter front-end more than 80 dB of harmonic rejection was observed for the dominating harmonic image.

A method for dealing with harmonic image interference was proposed for spectrum sensing applications. The method consists of an analog front-end that uses two quadrature down-converters to generate two complex baseband signals and a digital subband cross-correlator. The second down-converter is tuned Δf Hz higher than the first, resulting in the desired signal band experiencing a shift of Δf, while the harmonic images shift by $n \cdot \Delta f$, where n is the harmonic image number. This second baseband signal is shifted by $-\Delta f$ Hz in the digital domain, thereby spectrally re-aligning the desired signal band with the first baseband signal. The harmonic images, however, experience the same $-\Delta f$ Hz shift, irrespective of their harmonic number. Therefore, all harmonic images in the second baseband signal are not spectrally aligned with respect to the first baseband signal. The end result is that only energy found in the desired signal band will produce an output at the cross-correlator, while the harmonic images are rejected. The effectiveness of this method was shown by experimental simulations.

Samenvatting

Er is een groeiende behoefte aan draadloze communicatie en daardoor ook een groeiende vraag naar hogere communicatie snelheden. Om aan deze behoefte te kunnen voldoen, zijn nieuwe draadloze communicatiestandaarden nodig. Nieuwe electronische apparatuur moet zowel deze nieuwe standaarden ondersteunen als ook de oudere standaarden, omdat deze doorgaans niet vervangen worden door de nieuwe maar naast elkaar gebruikt worden. De draadloze systemen in deze apparatuur worden dus steeds complexer. Samen met de vraag naar steeds compacte apparatuur leidt dit tot de wens om alle radio functies onder te brengen in slechts één geïntegreerd circuit.

Het software-defined radio (SDR) concept, waarbij bijna alle radio functies in software zijn geïmplementeerd en door middel van een digitale signaal processor worden uitgevoerd, is naar alle waarschijnlijkheid de beste manier om het bovengenoemde radio ontwerp te kunnen realiseren, vooral omdat software als flexibel en uitbreidbaar is. Zo'n ontwerp bestaat uit een analoog front-end, dat verantwoordelijk is voor het omlaag mengen van de te ontvangen signaal, en een relatief grote digitale processor met bijbehorend geheugen en randapparatuur voor de verdere verwerking.

Tijdens ontvangst genereert een frequentiesynthesizer, die bestaat uit een hoogfrequent oscillator en een programeerbare digitale deler aan zijn uitgang, het benodigde mixersignaal. Schakelende mixers produceren met behulp van frequentietranslatie de basisband signalen voor de digitale processor. Deze schakelende mixers hebben de voorkeur vanwege hun uitstekende grootsignaal gedrag. Vanwege de pulsvormige signalen van de frequentiesynthesizer en de schakelende werking van de mixers, verschijnen echter niet alleen de gewenste frequentieband in het basisband signaal, maar ook andere frequentiebanden waardoor er storing onstaat. Deze ongewenste extra banden zijn harmonisch gerelateerd aan de gewenste frequentieband en worden daarom ookwel *harmonische banden* genoemd.

Tijdens ontvangst zorgen deze harmonische banden voor bitfouten in het gewenste signaal. Ook zorgen ze voor problemen bij het detecteren van lege plekken in de frequentieruimte (ookwel *spectrum sensing* genoemd); er wordt onterecht energie gedetecteerd in een frequentiegebied waar geen energie zit. In smalbandige ontvangers kan deze storing voorkomen worden door een extern hoogfrequent filter op te nemen tussen de antenne en de mixer. Voor breedbandige ontvangers, zoals SDR ontvangers, is een groot aantal van deze filters nodig. Dat maakt deze ontstoringsmethode onwerkbaar en vaak te duur voor toepassing in consumentenprodukten. Een andere aanpak is noodzakelijk.

In dit proefschrift wordt een methode gepresenteerd die gebaseerd is op *interference cancelling* om de storing, die veroorzaakt wordt door de sterkste harmonisch band, significant te verminderen. Hiervoor gebruiken we een analoog front-end met ongeveer 40 dB harmonische band onderdrukking dat twee complexe basebandsignalen genereert. Met behulp van deze twee signalen wordt er een signaal opgewekt dat de storing zo goed mogelijk benadert. Na egalisatie, om amplitude- en faseveschillen te verminderen, wordt deze benadering van het verstoorde ontvangen signaal afgetrokken, wat tot een schoner gewenst signaal moet leiden.

Deze methode is succesvol getest met behulp van twee verschillende analoge front-ends; één opgebouwd uit commercieel verkrijgbare componenten en één bestaande uit een volledig geïntegreerde 65nm CMOS implementatie. Metingen hebben aangetoond dat de harmonische band onderdrukking meer dan 80 dB bedraagt wanneer één harmonische band actief is.

Ook voor het verminderen van de storingsgevoeligheid van *spectrum sensing* toepassingen wordt een methode gepresenteerd. Er wordt een analog front-end voorgesteld dat bestaat uit twee kwadratuur down-converters en een digitale subband kruiscorrelator. Met behulp van de down-converters worden twee complexe basisbandsignalen gegenereerd. De tweede down-converter is Δf Hz hoger afgestemd ten opzichte van de eerste. Hierdoor ondergaat de gewenste band een verstemming van Δf Hz. De harmonische banden ondergaan een verstemming van $n \cdot \Delta f$ Hz, waarbij n het harmonische nummer is. In het digitale domein wordt het tweede basisband signal weer met $-\Delta f$ Hz terugverstemd waardoor de gewenste band spectraal gezien op een gelijke positie uitkomt ten opzichte van het eerste basisbandsignaal. De harmonische banden ondergaan echter eenzelfde verstemming van $-\Delta f$ Hz, ongeacht het harmonische nummer. De harmonische banden liggen hierdoor spectraal gezien niet op een gelijk positie. Het gevolg is dat alleen energie uit de gewenste band een significante responsie aan de uitgang van de kruiscorrelator zal laten zien, terwijl de harmonische banden onderdrukt worden. De effectiviteit van deze methods is met behulp van experimentele simulaties vastgesteld.

Contents

Chapter 1

Introduction

1.1 Introduction

Over the past few decades, wireless communication has seen tremendous growth. In many cases, wireless technology has all but replaced wired communication systems as is evident by the widespread adoption of cellular telephones and the use of wireless internet. This growth has resulted in the development of many wireless communication standards, such as IEEE 802.11a/b/g/n [1] for high-speed wireless LAN and GSM, DECT, Bluetooth, UMTS, and 4G LTE [2] for voice and data communications. In fact, new standards are continually being developed.

New standards do not replace their predecessors. An example of this is the GSM cellphone standard, which has been superseded,in a technical sense, by UMTS. In practice, however, GSM and its variants are still in widespread use. In effect, the number of wireless standards that devices such as cellphones, laptops and tablets must support, is growing.

To accommodate the new wireless standards, new frequency bands are allocated to the already existing allocations. The following non-exhaustive table lists a number of popular wireless standards and their allocated frequency band:

Standard	Purpose	Frequency
AM	broadcast radio	0.5-30 MHz
FM	broadcast radio	88-108 MHz
DVB	digital TV	50-860 MHz
T-DAB 3	broadcast radio	174-230 MHz
GSM-900	cell phone	890-915 MHz
T-DAB L	broadcast radio	1450-1480 MHz
GSM-1800	cell phone	1710-1880 MHz
DECT	short-range phone	1880-1900 MHz
UMTS	cell phone	1900-2025 MHz
802.11b/g/n	WLAN	2400-2500 MHz
802.11a/n	WLAN	4915-5825 MHz

As can be seen in the above table, wireless communication takes place over a wide range of frequencies.

Until recently, manufacturers of wireless devices and chipsets supported each wireless standard or family of standards separately by employing narrow-band transceivers in dedicated integrated circuits (ICs) with external filters, resulting in relatively large and costly systems. To reduce the size and costs of such devices, research and development effort has focused on ways to integrate as many different standards as possible onto a single IC. Given the wide variety of frequenties, the various modulation formats and related standard-specific requirements, this is a formidable task.

Software radio [3], a popular paradigm for achieving such a single-chip do-it-all radio was introduced by Joseph Mitola in the early 90's. The idea is to implement the radio completely in software, which is seen as flexible and can be updated to support new and emerging standards. The only hardware required for this type of radio is an antenna, an analog-to-digital converter (ADC) with anti-aliasing filter and a digital signal processor (DSP), which runs the software, see Fig. 1.1.

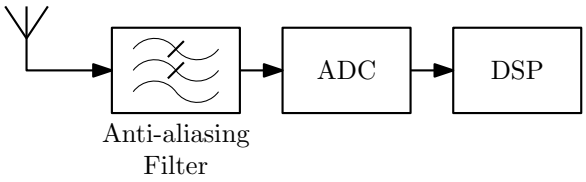

Figure 1.1: A block diagram of a software radio.

Unfortunately, the demands put on the ADC with respect to sampling rate and dynamic range currently makes the software radio paradigm impractical. For example, assuming a minimum sampling rate of 10 GS/s and 16-bit resolution to receive signals up to 5 GHz, the ADC would need more than 600 W of power, based on a figure-of-merit of 1 pJ per conversion[1].

[1] $Power = 2^{bits} \cdot F_s \cdot FoM$, where F_s is the sample rate in Hertz.

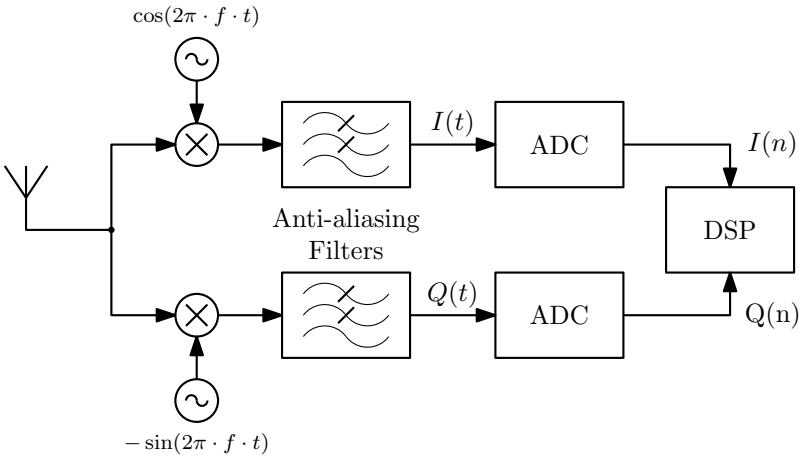

Figure 1.2: A block diagram of the ideal software-defined radio.

A more practical approach, also suggested by Mitola, is the software-defined radio (SDR) [3]. Here, a (quadrature) down-converter is used to translate the frequency band of interested to a much lower frequency, thereby considerably reducing the sampling rate, see Fig. 1.2

Both radio paradigms rely heavily on the DSP to realize flexible multi-standard intelligent radio transceivers. Given that CMOS is the dominant and most cost-effective IC technology for large scale integration of digital circuits, there is a strong desire to implement SDR transceivers in CMOS. Such a solution is hoped to bring down cost and increase the integration of embedded wireless sub-systems. Recently, several research groups have presented SDR architectures in CMOS that support multiple narrow-band radio standards [4, 5]

1.2 Problem Statement: Harmonic Down-mixing

The SDR front-end shown in Fig. 1.2 is wideband in nature; there is no RF filter before the down-converter. Consider the ideal case where the mixers are perfect multipliers. When the local oscillator (LO) driving the mixers produces pure sinusoidal signals, only the desired signal band, centered around the oscillator frequency, f, is translated down to zero Hertz. The ADCs convert this down-converted band to the digital domain for further processing by the DSP.

In reality, mixers are not perfect multipliers and pure sinusoidal signals are impossible to make. Thus, the local oscillator signal contains harmonics. Futhermore, even if a perfect sinusoidal were available, distortion of the LO signal within the mixer will cause the *effective* LO signal to have harmonics. These LO harmonics will cause

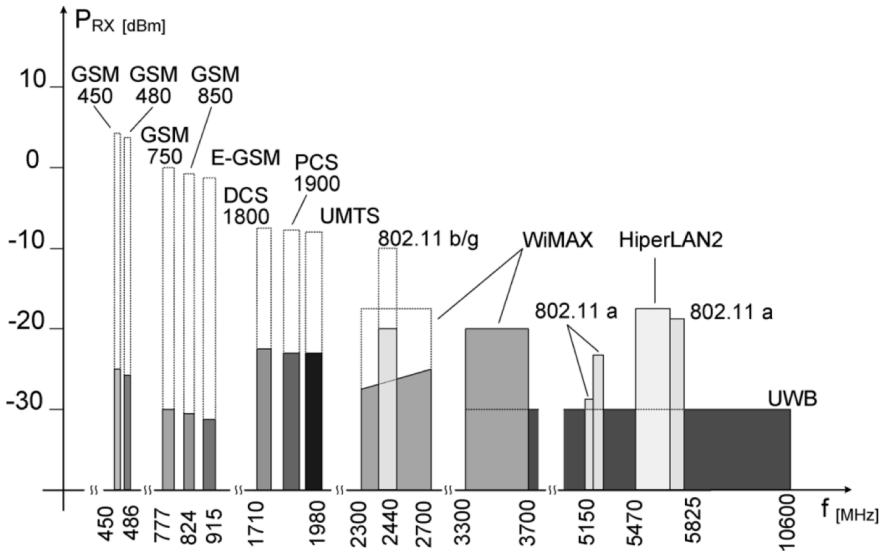

Figure 1.3: Signal powers found at the receive antenna in wireless bands covering 450 to 10600 MHz - dotted: without filtering - solid: with ultra-wideband preselection filter (3 to 10.6 GHz passband). The receive antenna is located 1 m away from the transmit antenna. [6]

down-mixing of frequency bands other than the desired signal band, which leads to interference in the form of *harmonic images*.

Although an absolute upper bound on the maximum received signal power cannot be given, Manstretta [6] reports a maximum received signal power of around +4 dBm within a frequency range of 450 to 10600 MHz, see Fig. 1.3, but without specifying the antenna used. Some radio standards specify 0 dBm as the maximum out-of-band signal. Should such strong signals appear in one of the image bands without taking countermeasures, the harmonic down-mixing effect will cause the desired signal to be swamped.

To illustrate the severity of the problem, consider a 0 dBm interferer and a receiver with a bandwidth of 10 MHz and a noise figure of 4 dB. Then the thermal noise power is -100 dBm. To reduce the interferer to the same power level as the noise floor, the interferer must be attenuated by 100 dB. This scenario shows that considerable attenuation of the harmonic images is needed, in order to recover the desired signal.

The traditional way around the harmonic down-mixing problem is to filter out the unwanted bands before they reach the mixer. This way, the harmonic image bands contain negligible signal power and will not cause interference to the desired signal when they are down-mixed to baseband.

In a receivers with a wide tuning range spanning multiple octaves, such as the SDRs,

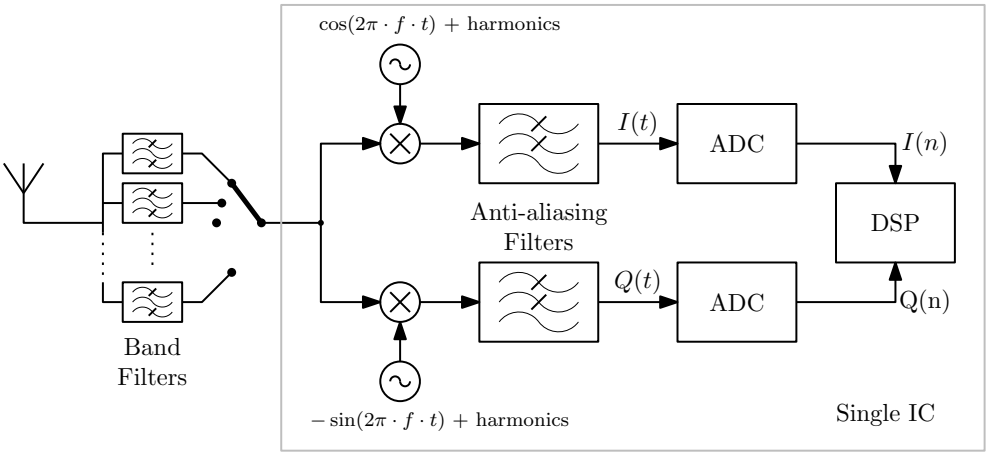

Figure 1.4: A block diagram of a real-world software-defined radio.

multiple high-Q band- or lowpass filters must be used to remove the unwanted image bands, as shown in Fig. 1.4. Furthermore, filters with steep skirts are needed to give sufficient attenuation of the closest, i.e. second and third, harmonic bands. Usually, integration of these filters in standard CMOS technology is not feasible as they are implemented in a dedicated passive filter technology and are therefore external to the main SDR chip. These external filters and the required switching arrangement, shown in Fig. 1.4, makes this solution bulky and prohibitively expensive for consumer applications. Clearly, a more practical solution, where the number of needed external filters is considerably reduced or made redundant, is desirable.

Harmonic down-mixing in CMOS based front-ends

Given that CMOS IC technology is optimized for digital circuits, it is often a challenge to implement traditional RF front-end circuits, such as high dynamic range wide-band RF amplifiers and active mixers. It can be advantageous to exploit the switching characteristics of the transistors, rather than operating them in their "linear" transconductive region. For example, a wide-band non-sinusoidal LO waveform is easier to generate than a harmonically clean sinusoid; the output of a high-frequency Voltage Controlled Oscillator (VCO) is divided down, using a digital programmable divider, to produce the lower octaves and the required quadrature LO signals. This produces a harmonically rich square- or pulse-wave LO, see Fig. 1.5.

Besides using digital circuits to generate LO signals, switch-based passive mixers are often used because of their excellent RF-to-IF port linearity compared to true four-quadrant multiplying mixers, such as a "Gilbert" cell [7]. In addition, these switching mixers integrate well in current CMOS processes. As a result, the switching mixer driven by a frequency synthesizer with a digitally divided output, see Fig. 1.6 (b), is

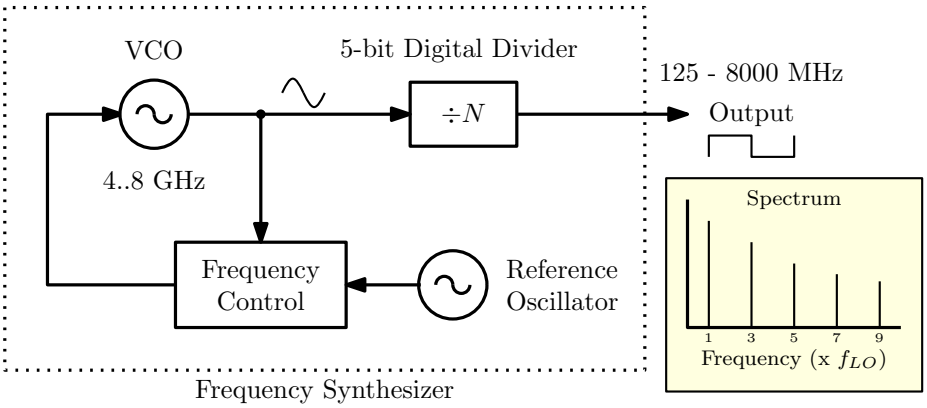

Figure 1.5: Block diagram of a frequency synthesizer employing a voltage-controlled oscillator (VCO) which generates a frequency f_{LO}. A digital programmable divide-by-N divider is used to generate lower frequencies.

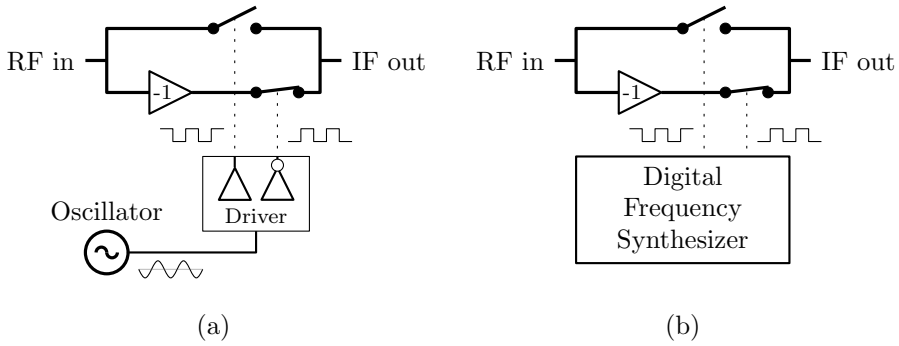

Figure 1.6: Block diagram of a switching mixer: (a) an oscillator with sinusoidal output is used to drive the switching mixer through a driver circuit. (b) a digital frequency synthesizer directly drives the switching mixer.

a popular mixer topology in nanometer CMOS implementations [8, 9], and is often used even when the LO waveform is sinusoidal, see Fig.1.6 (a).

As will be shown in Chapter 3, when the effective LO waveform of the mixer is a 50% duty-cycle square wave, a common situation when employing switching mixers, the third and fifth harmonic image bands are rejected by only 9.5 and 14 dB, respectively. These figures are related to the third and fifth harmonic amplitudes (1/3 and 1/5) of the square wave, which can be determined by Fourier series analysis. Considering the empirically determined worst-case signal strength of +4 dBm, the post-mixer signal can contain up to -5.5 dBm of harmonic image interference.

Harmonic image interference is not only a problem for regular receive applications.

It also a problem in cognitive radios [10], which use intelligent techniques to adapt to their RF surroundings. One particular adaptation technique is scanning, or *spectrum sensing*, for unused parts of the radio spectrum, also referred to as *white spaces*, to setup a radio network in an ad-hoc fashion. The presence of harmonic downmixing interference may cause the spectrum sensing algorithms to incorrectly classify unused spectrum as occupied, thereby reducing the available white space.

In conclusion, harmonic image interference is a significant problem that arises in TV tuners[2], cognitive radios and wide-band cost sensitive receiver applications, such as mobile phones, tablets, laptops and other consumer gadgets, where many front-end RF filters are undesirable.

1.3 Previous Work: Harmonic-rejection mixers

In the last decade, several solutions based on polyphase topologies were proposed to increase the harmonic rejection of the CMOS switching mixer, first in transmitters by Weldon [11] and then in receivers [4, 12, 13] and others.

The principle of the harmonic rejection polyphase mixer is based on a set of switching mixers connected in parallel, where each switching mixer is driven by its own (digital) LO waveform and weighted by an amplifier, as shown in Fig. 1.7. In this way, the effective LO waveform is a staircase waveform which can be designed such that certain harmonics are not present, thereby eliminating the associated harmonic image bands. Using an eight-phase clock, which enables an eight-level staircase LO waveform, the third and fifth harmonics are eliminated, making the first uncancelled harmonic image band that appears at the mixer output the seventh-order harmonic image [11, 4].

As will be explained in Chapter 3, complete elimination only occurs when the amplifiers have exactly the desired gain and the individual switching mixer waveforms have exactly the desired timing characteristic. In practice, these conditions are never met because of (unkown) parasitic components, temperature effects, aging and process variations in IC production. Real-world third-order and fifth-order harmonic rejection figures, as reported in literature [4, 12, 13], are limited to roughly 30 to 40 dB.

While the extra harmonic image attenuation provided by the polyphase harmonic rejection mixer reduces the amount of RF-side filtering necessary, clearly more attenuation is needed. The attenuation can be boosted to more than 60 dB by employing a second stage of mixers, by targeting amplitude errors but not phase and timing errors [14, 15]. This research was done in parallel with the work presented in this thesis.

The harmonic rejection mixer techniques described above rely on achieving precise phase and amplitude relations of the signals reaching the summing point at the output of the mixer. Even with highly effective circuit design and layout techniques, such

[2]Televisions were the first consumer oriented devices where harmonic downmixing had to be addressed because of their wideband tuning range.

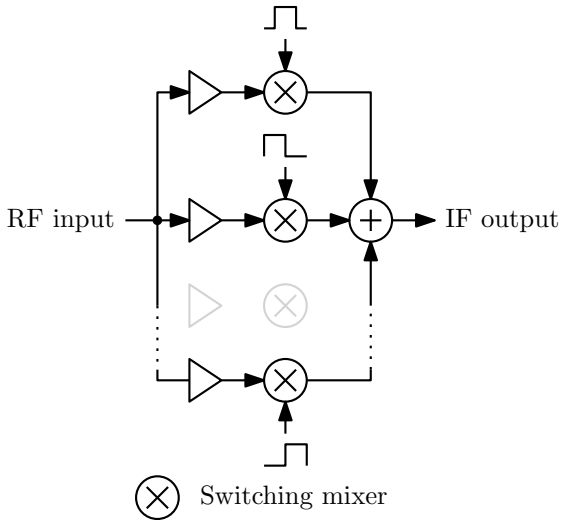

Figure 1.7: A harmonic rejection receive mixer based on the polyphase topology. The mixer consists of multiple switching mixers, each driven by their own switching waveform. The switching mixers are isolated by amplifiers, which allows different weighting of each mixer.

as those presented in [14], process and fabrication variations will always negatively affect the attainable harmonic rejection.

1.4 Research Objectives

As stated earlier, harmonic rejection figures in the order of 100 dB or greater are desired. Rather than relying only on circuit design and layout techniques to minimize the harmonic down-mixing image interference, the objective of this research is to develop signal processing algorithms to further increase the downstream harmonic rejection, or increase the immunity to this type of interference. By making the algorithms adaptive, the total system performance will be less dependent on process and fabrication variations, temperature effects and circuit aging.

To simplify system integration, the signal processing algorithms must not use properties defined in the wireless standards, such as modulation format, training sequences, pilot tones or use data-aided techniques. That is, the algorithms must be *blind*. Furthermore, the use of digitally assisted analog calibration was ruled out, again to ease system integration and reduce risk. The algorithms should be easy to add onto existing systems in a "bolt on" fashion.

In addition to the above constraints, the algorithms must be simple to implement, use as little hardware and software resources as possible, i.e. be of low complexity.

1.5 Related work

At the time this research started (mid-2007), to the best of our knowledge, there was no publicly available prior art that uses signal processing to deal with harmonic image interference. However, digital signal processing has been successfully used to reduce I/Q imbalance [16, 17], reduce IM3 products in receivers [18], linearize RF power amplifiers [19] and reduce the effect of jammers [20]. The IEEE online digital library [21] contains many more examples of the application of adaptive signal processing to increase the performance of analog circuitry. In fact, there are too many examples to list here.

Since publishing the results of this research at conferences and in journals, few publications have appeared that extend or make use of this work. The most notable are [22], which uses a six-phase mixer and aims to cancel second-order harmonic images, and the work by Mark Oude Alink on spectrum sensing using cross-correlation [23].

1.6 Thesis organization

This thesis is organized as follows. Chapter 2 introduces the concepts of baseband-equivalent signals and adaptive signal processing techniques. Its target audience are designers who are not familiar with these subjects. It also defines the notations used in the remainder of this thesis.

The main body of work is presented in Chapters 3, 4, 5 and 6, where the former three describe adaptive interference cancelling techniques to increase the performance of polyphase harmonic rejection mixers and the latter addresses the problem of spectrum sensing in the presence of harmonic image interference. These chapters are reprints of articles or conference contributions. References to the original publications can be found at the beginning of these chapters.

Chapters 3, 4 and 5 are presented in order of development, starting with the theoretical side of harmonic rejection enhancement in Chapter 3. In Chapter 4, a frequency scaled experiment based on off-the-shelf discrete ICs is presented. This work was done to convince ourselves of the feasibility of the solution without developing a custom IC. Chapter 5 describes a more efficient implementation of the signal processing algorithm and the harmonic rejection results based on a polyphase analog front-end developed by Dr. Z. Ru [24].

Chapters 7 offers the conclusions, the summary, a list of original contributions and presents ideas for future work.

Chapter 2

Adaptive Signal Processing Techniques

2.1 Introduction

Adaptive digital signal processing techniques are widely used throughout this thesis. This chapter attempts to show, in an intuitive way, the basic operation of feed-forward and feed-back adaptive signal processing techniques. For a more formal treatment, the reader should consult the appropriate literature [25, 20, 26]. A secondary goal of this chapter is to introduce the mathematical notation used.

Adaptive signal processing algorithms use statistical information, such as variance and cross-correlation of the input, internal or output signals, to change their behavior in such a way that it benefits their performance. Section 2.5 demonstrates how the aforementioned statistics can be applied to implement an adaptive interference canceller using feedback. Section 2.4 shows how a feed-forward I/Q imbalance compensator may be constructed.

The algorithms presented in this thesis operate on down-converted signals, which have been discretized by analog-to-digital converters (ADC), the so-called *baseband* signals. The (low-frequency) baseband signals and their radio-frequency (RF) counterpart are mathematically linked through the baseband-equivalent signal theory. Before discussing the adaptive signal processing algorithms, baseband-equivalent signal theory is addressed.

2.2 Baseband-equivalent signals

A time-varying RF signal $x(t)$ spectrally centered around a frequency f Hz, also termed a *passband signal*, can be decomposed into its center frequency f and a

complex-valued lowpass signal, $z(t)$. The latter signal is referred to as the *baseband-equivalent signal*, or simply, the *baseband signal*.

The baseband signal, $z(t)$, captures the information which has been modulated on the RF carrier. Given the carrier's frequency f and the baseband signal $z(t)$, the original RF signal, $x(t)$, can be represented by [27, 28, 29]:

$$x(t) = \Re\{z(t) \cdot e^{j \cdot 2\pi \cdot f \cdot t}\}, \tag{2.1}$$

where $\Re\{\}$ denotes the taking of the real part of its argument.

Or equivalently:

$$x(t) = \frac{1}{2}\left[z(t) \cdot e^{j \cdot 2\pi \cdot f \cdot t} + z^*(t) \cdot e^{-j \cdot 2\pi \cdot f \cdot t}\right], \tag{2.2}$$

where * denotes a complex conjugation.

Equation (2.2) shows that the baseband signal, $z(t)$, appears in two forms: once in its regular form and once in its conjugated form. An important property of complex baseband signals is that a conjugation operation is equivalent to spectrally mirroring the signal around 0 Hz. In other words, the lower sideband becomes the upper sideband and vice versa.

An example of the decomposition is shown in Fig. 2.1, where a 1 GHz modulated carrier is decomposed into its baseband signal. Also shown is the conjugated version of the baseband signal.

2.2.1 Examples of signals

Several RF signals and their baseband-equivalent counterparts are given here as examples of the kind of signals that one encounters frequently in literature and in practical situations.

An unmodulated sub-carrier signal offset by δf from the center frequency appears as a complex exponential term:

$$z(t) = a \cdot e^{j \cdot (2\pi \cdot \delta f \cdot t + \phi)}, \tag{2.3}$$

where a is the real-valued amplitude and ϕ is the staring phase at $t = 0$. When plotted in the complex plane, the result is a perfect circle with radius a.

Table 2.1 gives an overview of often encountered RF signals and their baseband-equivalent version and associated frequency.

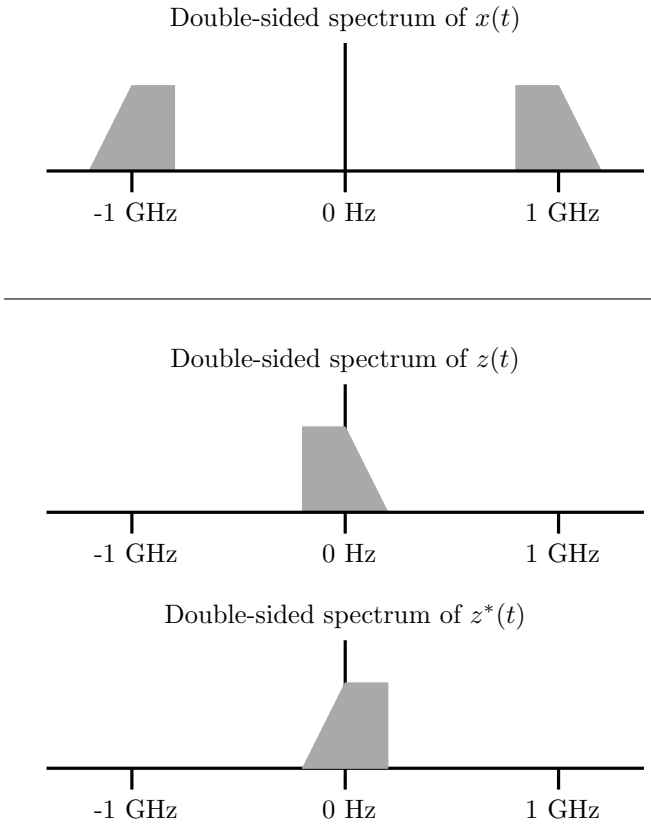

Figure 2.1: Example: double-sided spectra of a time-domain and corresponding baseband signal.

Table 2.1: Baseband-equivalent versions of often encountered signals

$x(t)$	$z(t)$	f
c	c	0
$\cos(2\pi \cdot f_c \cdot t)$	1	f_c
$\sin(2\pi \cdot f_c \cdot t)$	$-j$	f_c
$a(t) \cdot \cos(2\pi \cdot f_c \cdot t)$	$a(t)$	f_c

2.2.2 Quadrature upconverter equivalency

Most interestingly, the RF reconstruction expression (2.2) is the mathematical version of the well-known quadrature direct-conversion transmitter. This can be shown by splitting the baseband signal $z(t)$ into its real and imaginary components, $z_I(t)$ and $z_Q(t)$ respectively, and writing (2.2) following the same principle:

$$\begin{aligned} x(t) &= \frac{1}{2}\left[z(t)\cdot e^{j\cdot 2\pi\cdot f\cdot t} + z^*(t)\cdot e^{-j\cdot 2\pi\cdot f\cdot t}\right] \\ &= \frac{1}{2}\left[(z_I(t)+j\cdot z_Q(t))\cdot e^{j\cdot 2\pi\cdot f\cdot t} + (z_I(t)-j\cdot z_Q(t))\cdot e^{-j\cdot 2\pi\cdot f\cdot t}\right] \\ &= \frac{1}{2}\left[z_I(t)\cdot\left(e^{j\cdot 2\pi\cdot f\cdot t}+e^{-j\cdot 2\pi\cdot f\cdot t}\right) + j\cdot z_Q(t)\cdot\left(e^{j\cdot 2\pi\cdot f\cdot t}-e^{-j\cdot 2\pi\cdot f\cdot t}\right)\right] \\ &= \frac{1}{2}\left[z_I(t)\cdot 2\cos(2\pi\cdot f\cdot t) + z_Q(t)\cdot 2\sin(-2\pi\cdot f\cdot t)\right] \\ &= z_I(t)\cdot\cos(2\pi\cdot f\cdot t) - z_Q(t)\cdot\sin(2\pi\cdot f\cdot t), \end{aligned} \tag{2.4}$$

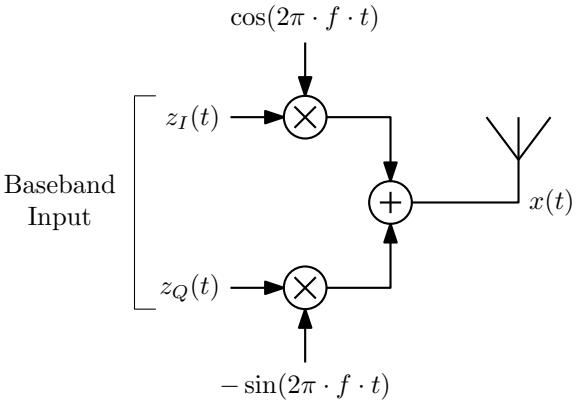

Figure 2.2: The system-level diagram of a quadrature up-converter.

2.2.3 Advantages to modeling and simulation

The advantage of using baseband-equivalent signals for modeling and analysis of communication systems lies in the fact that frequency shifting operations on $x(t)$, by means of mathematical multiplication, only affects the translation frequency f of the signal, resulting in simple mathematical expressions [27]; the use of trigonometric functions is largely avoided. In effect, mathematical models based on baseband signals are compact, easy to read and therefore less prone to mistakes.

A second advantage of baseband-equivalent signals lies in the simulation of communication systems. By employing baseband-equivalent signals and models, the simula-

tion engine can use a (much) larger time step, as the highest frequency is much lower than in the regular time domain case.

Care must be taken when simulating non-linear systems as they introduce new frequency products through intermodulation and other distortion effects [27]. These new products can be part of existing baseband-equivalent signals but often new baseband-equivalent signals must be introduced to represent these products.

2.2.4 Weighted baseband signals

Throughout this thesis, weighted baseband signals in the form of

$$y(t) = \alpha \cdot z(t) \tag{2.5}$$

or

$$y(t) = \alpha \cdot z^*(t) \tag{2.6}$$

are encountered, where α is a complex-valued weighting coefficient. Complex weighting results in a scaled and rotated version of the original signal. This can be shown mathematically by writing the weighting factor α as a complex exponential:

$$\alpha = a \cdot e^{j2\pi \cdot b}, \tag{2.7}$$

where a is the vector length of α and $2\pi \cdot b$ is the vector angle in radians. Given this reformulation, the output $y(t)$ can be rewritten as a matrix equation:

$$\begin{bmatrix} y_I(t) \\ y_Q(t) \end{bmatrix} = a \cdot \begin{bmatrix} \cos(2\pi b) & -\sin(2\pi b) \\ \sin(2\pi b) & \cos(2\pi b) \end{bmatrix} \begin{bmatrix} z_I(t) \\ z_Q(t) \end{bmatrix}, \tag{2.8}$$

where $z_I(t)$, $z_Q(t)$, $y_I(t)$ and $y_Q(t)$ are the real and imaginary parts of z and y respectively. The 2-by-2 matrix is a 2D rotation matrix, see [30] page 203, and multiplication by a performs the scaling.

2.3 Adaptive signal processing algorithms

Adaptive signal processing algorithms are algorithms that adapt their behavior to optimally perform under varying and unknown operating conditions. For these algorithms to be widely applicable, it is highly desirable to have well-performing algorithms that do not rely on specific properties, such as the shape, phase, frequency or modulation scheme, of the signals they process. Rather than operating on the basis of the aforementioned properties, many adaptive algorithms use statistics of the input or output signals to identify the current operating condition and periodically update their behavior accordingly.

The statistics on which most adaptive algorithms are based are often the *mean*, *variance* and *cross-correlation*, but *skewness*, *kurtosis* and related high-order statistics

are also used [31]. This work uses only the first and second-order statistical properties as they lead to good results and require fewer assumptions to be made about the processed signals.

In general, the aim of an adaptive algorithm is to find a set of parameters under which a certain performance measure is maximized, or a cost function is minimized. For example, a phase-locked loop (PLL) is an adaptive system that aims to minimize a phase error by finding a suitable voltage for its voltage-controlled oscillator.

2.3.1 Feed-forward and feedback algorithms

There are two classes of adaptive algorithms. The first class is the feed-forward class, where the optimal parameters are determined directly from input signal statistics. The second class is the feedback algorithm, where the input signals are processed first, based on previously established parameters. The parameters are then updated by using the statistics of intermediate or the *output* signals, as shown in Fig. 2.3.

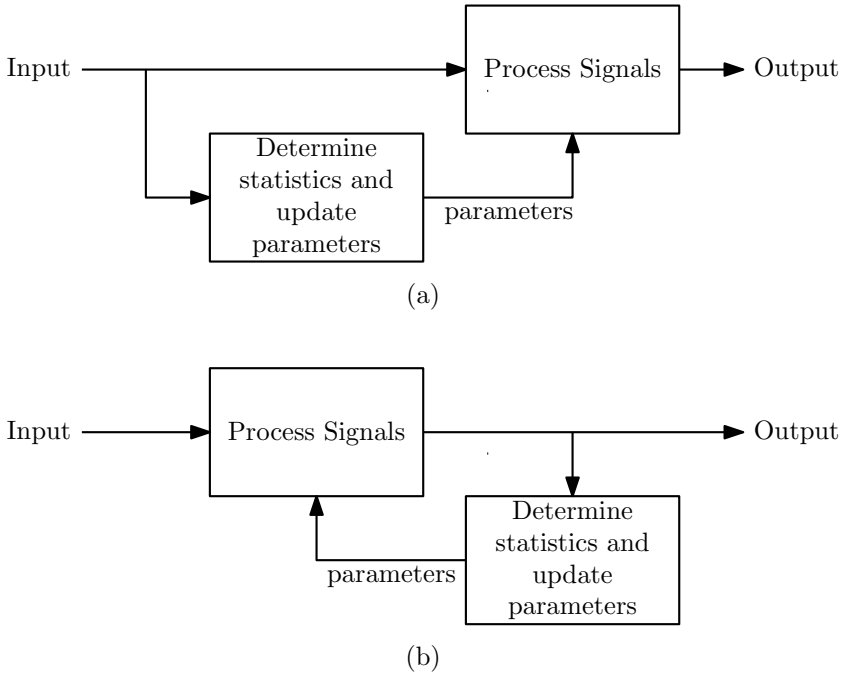

Figure 2.3: (a) a feed-forward adaptive algorithm. (b) a feedback adaptive algorithm.

As an example of how statistics are applied to create an adaptive system, a feed-forward algorithm for reducing receiver I/Q imbalance is shown and a feedback algo-

rithm for interference canceling is evaluated. The examples will introduce the trade-offs and important properties of both types of algorithms.

2.4 Feed-forward Adaptive Signal Processing: I/Q imbalance compensation

A quadrature direct-conversion receiver has I/Q imbalance when the received signal undergoes unequal gain in the I and Q branches, or when the local oscillator does not produce a quadrature signal that is exactly 90 degrees out of phase. The result of this gain or phase imbalance is that interference is caused to the desired baseband signal $z(t)$ due to the presence of its spectrally mirrored counterpart $z^*(t)$ [32]. Receiver I/Q imbalance compensation is related to harmonic image rejection as both problems involve unwanted image signals distorting the desired signal.

Figure 2.4 shows a system-level model of a quadrature down-converter with a frequency-independent gain imbalance g and an LO phase imbalance of ϕ radians. Without loss of generality, the I path has been normalized in gain and phase, which transfers any imbalances found there to the Q path [32].

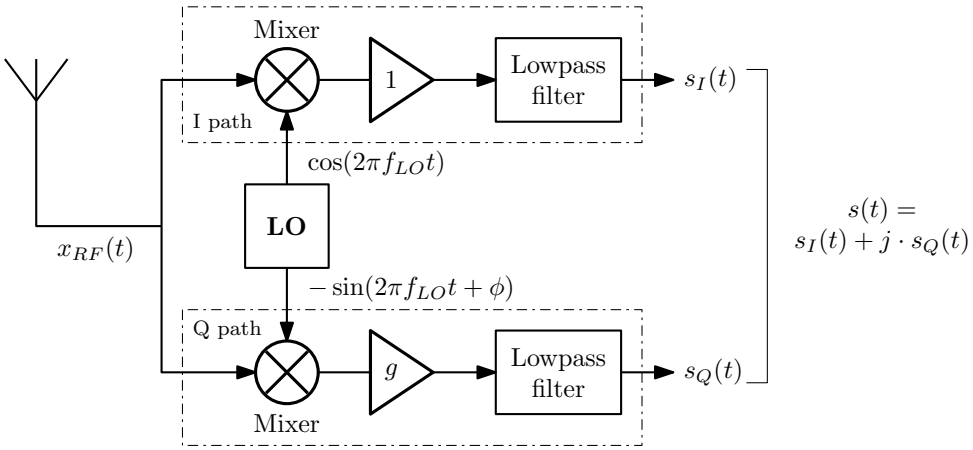

Figure 2.4: Quadrature down-converter with gain imbalance g and LO phase imbalance ϕ.

2.4.1 Baseband equivalent analysis

To analyze the effects of the gain and phase imbalance parameters, an modulated RF signal, $x_{RF}(t)$, is applied at the antenna. The RF signal is generated by modulating a carrier of f_{LO} Hz with a generic baseband signal $z(t)$:

$$\begin{aligned} x_{RF}(t) &= 2\Re\{z(t) \cdot e^{j2\pi \cdot f_{LO} \cdot t}\} \\ &= z(t) \cdot e^{j2\pi \cdot f_{LO} \cdot t} + z^*(t) \cdot e^{-j2\pi \cdot f_{LO} \cdot t}. \end{aligned} \tag{2.9}$$

The baseband output of the down-converter is given by [32]:

$$s(t) = K_1 \cdot z(t) + K_2 \cdot z^*(t), \tag{2.10}$$

with $K_1 = \frac{1+g}{2} e^{-j\phi}$ and $K_2 = \frac{1-g}{2} e^{j\phi}$.

Equation 2.10 shows that the output signal $s(t)$ of the down-converter contains the desired baseband signal $z(t)$, but also its spectrally mirrored image in the form of the complex conjugate term, $z^*(t)$. Having both terms present at the output $s(t)$ leads to self-interference.

When there are no imbalances present in the down-converter, $g = 1$ and $\phi = 0$. In this case, $K_1 = 1$ and $K_2 = 0$, which reduces the output of the down-converter to $s(t) = z(t)$ and the transmitted baseband signal is completely recovered.

An interesting and often neglected fact is that when $g = -1$ and $\phi = 0$ the output becomes $s(t) = z^*(t)$, where only the mirrored baseband signal is present. In this situation, the transmitted baseband signal can be recovered by conjugating the output signal $s^*(t) = z(t)$; a very simple operation indeed.

Summarizing the above, the effect of an LO phase and gain imbalance is the appearance of an additional baseband term at the output of the down-converter, which causes interference. Thus, to remove the I/Q imbalance effects, we must remove this additional term.

2.4.2 Real-valued analysis

Additional insight into the I/Q imbalance problem is obtained by splitting the complex-valued equation (2.9) into its real and imaginary parts:

$$x_{RF}(t) = 2 \cdot z_I(t) \cdot \cos(2\pi \cdot f_{LO} \cdot t) - 2 \cdot z_Q(t) \cdot \sin(2\pi \cdot f_{LO} \cdot t). \tag{2.11}$$

Then, by inspection of Fig. 2.4 and some algebraic manipulation, the down-converter output is equal to:

$$s_I(t) = z_I(t) \tag{2.12}$$

$$s_Q(t) = g \cdot \cos(\phi) \cdot z_Q(t) - g \cdot \sin(\phi) \cdot z_I(t). \tag{2.13}$$

This analysis shows that the in-phase channel of the down-converter, $s_I(t)$, is unaffected by the I/Q imbalance and that $s_Q(t)$ contains energy from both the real and imaginary parts of the transmitted baseband signal $z(t)$, while only the imaginary part of $z(t)$ is desired. A graphical representation of the I/Q imbalance equations is shown in Fig. 2.5.

Given that the undesired real part, $z_I(t)$, is directly available as $s_I(t)$, it is easily removed from $s_Q(t)$ when the gain imbalance and LO phase imbalance parameters, g and ϕ, are known. The required compensator is given by:

$$z'_I(t) = s_I(t) \tag{2.14}$$

$$z'_Q(t) = \frac{1}{g \cdot \cos(\phi)} \cdot \left(s_Q(t) + g \cdot \sin(\phi) \cdot s_I(t)\right), \tag{2.15}$$

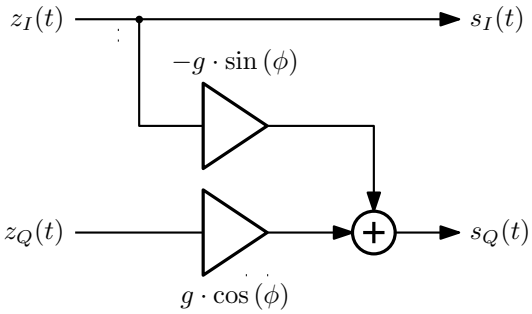

Figure 2.5: Graphical representation of I/Q imbalance model (2.12) *and* (2.13)

where $z'_I(t)$ and $z'_Q(t)$ are the compensated baseband outputs. Figure 2.6 shows the compensator structure.

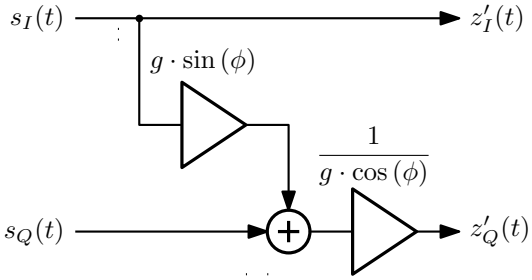

Figure 2.6: Graphical representation of the I/Q imbalance compensator

Unfortunately, the I/Q imbalance parameters are determined by errors in component values in the down-converter circuits owing to process spread and other factors, such as temperature. Therefore, the required compensation factors $\frac{1}{g \cdot \cos(\phi)}$ and $g \cdot \sin(\phi)$ are unknown and must be obtained though estimation.

2.4.3 I/Q imbalance parameter estimation

Estimation of the compensation factors is possible by means of the variance and covariance of $s_I(t)$ and $s_Q(t)$, but only after introducing a number of (statistical) assumptions on the transmitted baseband signal, $z(t)$. The first assumption is that the real and imaginary parts, $z_I(t)$ and $z_Q(t)$ respectively, have zero mean, i.e. there is no DC offset. The second assumption is that both parts have equal variance, i.e. their powers are identical. Thirdly, it is assumed that $z_I(t)$ and $z_Q(t)$ are independent so that their co-variance is zero. The final assumption is that all signals are wide-sense stationary (WSS).

The above assumptions may seem restrictive. However, most modern independent-sideband modulation formats featuring point-symmetric four-quadrant constellations, such as M-PSK, M-QAM and their OFDM variants, do not violate these assumptions.

Given the zero-mean, independence and WSS assumptions, the variances of $s_I(t)$ and $s_Q(t)$ are:

$$\mathbf{E}\{s_I \cdot s_I\} = \sigma_{z_I}^2 \tag{2.16}$$

$$\mathbf{E}\{s_Q \cdot s_Q\} = g^2 \cos^2(\phi) \cdot \sigma_{z_Q}^2 + g^2 \sin^2(\phi) \cdot \sigma_{z_I}^2, \tag{2.17}$$

and the covariance is:

$$\mathbf{E}\{s_I \cdot s_Q\} = -g \cdot \sin(\phi) \cdot \sigma_{z_I}^2, \tag{2.18}$$

where $\mathbf{E}\{\}$ denotes the expectation operator, $\sigma_{z_I}^2$ is the variance of $z_I(t)$ and $\sigma_{z_Q}^2$ is the variance of $z_Q(t)$.

Under the assumption that the variances of $z_I(t)$ and $z_Q(t)$ are equal, i.e. $\sigma_{z_Q}^2 = \sigma_{z_I}^2$, equation (2.17) can be simplified to:

$$\mathbf{E}\{s_Q \cdot s_Q\} = g^2 \cdot \sigma_{z_I}^2. \tag{2.19}$$

Obtaining $g \cdot \sin(\phi)$ is straight forward:

$$\frac{-\mathbf{E}\{s_I \cdot s_Q\}}{\mathbf{E}\{s_I \cdot s_I\}} = g \cdot \sin(\phi). \tag{2.20}$$

The second factor, $\dfrac{1}{g \cdot \cos(\phi)}$, is determined by making use of the fact that $g \cdot \cos(\phi) = \sqrt{g^2 - g^2 \cdot \sin^2(\phi)}$:

$$\left[\sqrt{\frac{\mathbf{E}\{s_Q \cdot s_Q\}}{\mathbf{E}\{s_I \cdot s_I\}} - \left(\frac{\mathbf{E}\{s_I \cdot s_Q\}}{\mathbf{E}\{s_I \cdot s_I\}} \right)^2} \right]^{-1} = \frac{1}{g \cdot \cos(\phi)}. \tag{2.21}$$

Interestingly, the expressions given for $\dfrac{1}{g \cdot \cos(\phi)}$ and $g \cdot \sin(\phi)$ are exact under the condition that the assumptions hold. The problem now is to obtain accurate estimates for the variances (2.16), (2.17) and the covariance (2.18). A popular way of estimating these, is by using the sample variance [33] and sample covariance.

Sample variance and covariance

The sample variance and sample covariance are based on averaging multiple samples, taken at different times, of the variables. In this particular case, the sample variances

and sample co-variance lead to the following expressions:

$$\mathbf{E}\{s_I \cdot s_I\} \approx \frac{1}{N}\sum_{i=1}^{N} s_I^2(i) \tag{2.22}$$

$$\mathbf{E}\{s_Q \cdot s_Q\} \approx \frac{1}{N}\sum_{i=1}^{N} s_Q^2(i) \tag{2.23}$$

$$\mathbf{E}\{s_I \cdot s_Q\} \approx \frac{1}{N}\sum_{i=1}^{N} s_I(i) \cdot s_Q(i), \tag{2.24}$$

where N denotes the number of samples taken. The time variable t has been replaced by a sample index i to identify each sample. In most applications, the samples are taken over time and at regular intervals using a analog-to-digital converter (ADC).

In general, the more samples that are used, the better the estimate. Herein lies a time versus accuracy trade-off; taking more samples leads to a better estimate, but it takes more time for the system to adapt to a new situation and uses more memory to accumulate the samples.

It can be shown, see Appendix A, that the sample variance estimator

$$T : \frac{1}{N}\sum_{i=1}^{N-1} x^2(i)$$

has a variance of

$$\mathrm{var}(T) = \frac{2\sigma^4}{N},$$

when the samples $x(n)$ are drawn from a zero-mean normally distributed random process with variance σ^2. Thus, as the number of samples N tends to infinity, the estimation error tends to zero.

Given the expressions of the sample variance and sample covariance, the necessary I/Q imbalance compensation parameters can be estimated. To empirically evaluate the I/Q imbalance compensator, discrete-time simulations were performed. Note that the previous continuous-time equations for $s(t)$ and $z'(t)$ can be used in discrete time, simply by replacing the continuous-time variable t with a sample index n.

2.4.4 Simulation setup and results

Using MATLAB, a complex-valued discrete-time baseband signal $z(n)$ was generated using two 3-bit random number generators; one for the I component, the other for the Q component. This signal was fed through our I/Q imbalance model, (2.12) and (2.13), using 1 dB of gain imbalance and 10 degrees of LO phase imbalance[1].

[1]These imbalance figures have purposely been chosen large in order to show the warping of the constellation.

Then, the I/Q imbalance compensator parameters were estimated, with the number of samples $N = 1000$, and used in the compensator to compensate the I/Q imbalance.

The effect of I/Q imbalance are shown by Fig. 2.7, where the constellations of the transmitted baseband signal $z(n)$ and the received baseband signal $s(n)$ are plotted; the perfectly square constellation is severely warped. After compensation, the constellation is almost returned to its original form, as shown in Fig. 2.8. The compensation is not perfect, due to slight errors in the parameter estimators caused by the finite number of samples used.

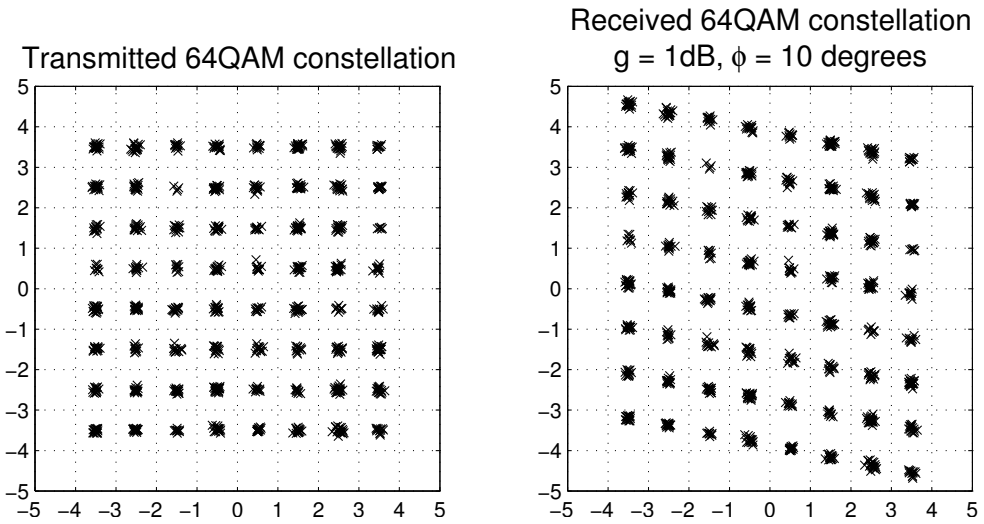

Figure 2.7: Plots of a transmitted constellation (left) and the received constellation which underwent 10 degrees of LO phase imbalance and 1 dB of gain imbalance at the receiver.

2.4.5 Practical considerations

The previous subsections showed how to estimate the I/Q imbalance parameters and apply them to the compensate I/Q imbalance using a feed-forward compensator. They also show the necessity of obtaining the compensator parameters by explicit expressions. This undesirable requirement is not specific to the problem of I/Q imbalance, but exists in general for feedforward systems.

The sample-variance and covariance estimators operate on blocks of samples and are mathematically simple. This might give the impression that algorithms based on these estimators are simple, elegant and easily implemented in hardware. However, there are three important implementation aspects to consider.

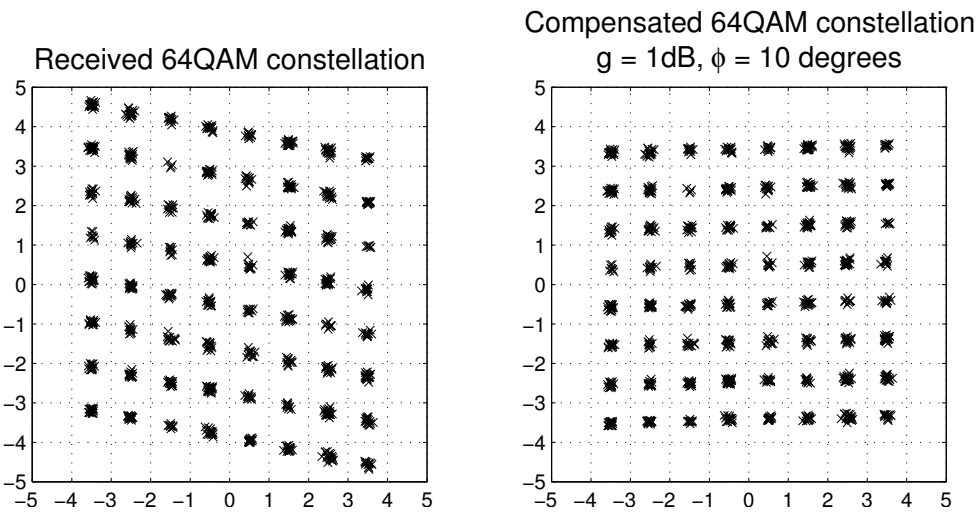

Figure 2.8: Plots of a received constellation (left) and the constellation at the output of the compensator, based on $N = 1000$ samples.

Firstly, when implemented in on-chip hardware, the estimators require random access memory (RAM) to hold N number of samples. These RAMs take up a relatively large portion of the die area, given that they need a storage cell per bit, row & column drivers and sense amplifiers. In addition, RAMs are tested using on-chip built-in self test (BIST) circuitry, which presents an area overhead. In effect, use of RAM is to be avoided whenever possible to keep the die area small and thus the system cost low. For example, when incoming data must be summed over N samples and the sum is only used once every N samples, a resettable accumulator as shown in Fig. 2.9 is more are efficient.

Secondly, the sample-variance and covariance estimators have a latency that is at least as large as the time it takes to sample N samples. Therefore, the compensation scheme will always lag behind the actual environment. When the environment changes slowly with respect to the acquisition time of N samples, such as in the I/Q imbalance scenario described above, the compensator can usually track the changes adequately.

Finally, as the accuracy of the sample-variance and covariance estimators are dependent on the number of samples N, and N determines the size of the buffer RAM needed, the achievable accuracy of the estimates is dependent on how large the buffer RAM can be made and how much latency can be tolerated.

In addition to these aspects, the output signals of the estimators must be processed before they can be applied to the compensator. In many cases, this processing uses complex-to-implement transcendental functions, powers or roots. These functions are more easily implemented in software using an embedded processor. As the output rate of the estimators is just once every N samples, the processor can be used to

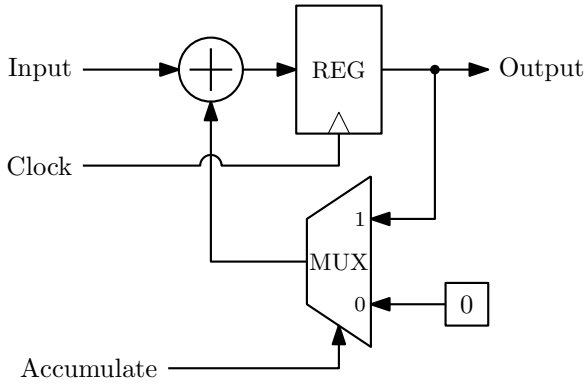

Figure 2.9: A block diagram of a resettable accumulator which consists of an adder, a register and a multiplexer. When the accumulate signal is "1", the register keeps accumulating the incoming data. When the accumulate signal is "0", the multiplexor outputs zero effectively bypassing the adder.

perform the further processing of these signals at the lower rate and load the resulting compensation parameters into the compensator, which is implemented in dedicated hardware.

In conclusion, feed-forward compensation algorithms based on variance and covariance estimators are often undesirable for on-chip implementation unless the system contains a processor for which RAM is already needed.

2.5 Feedback Adaptive Signal Processing: LMS Adaptive interference canceling

Adaptive compensation schemes based on the least mean squares (LMS) algorithm [34] have several advantages over feed-forward systems. Firstly, a set of parameters with explicit mathematical expressions is not needed; the system is self organizing. Secondly, the statistical information upon which the parameters are based does not need to be estimated directly but is used implicitly by the algorithm. Both features offer greatly reduced computational burden and die area reduction when implemented directly in hardware.

2.5.1 LMS-based compensation scheme

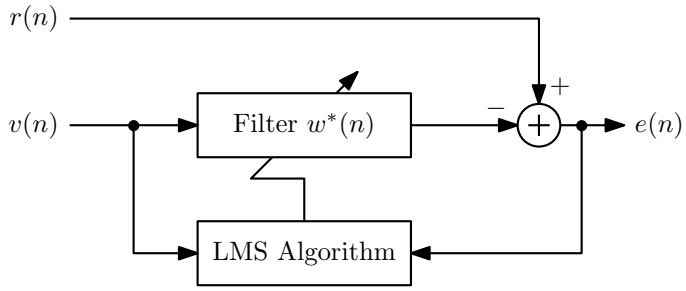

Figure 2.10: A block diagram of an adaptive filter, consisting of a single complex-valued time-varying filter coefficient $w^*(n)$, used as in interference canceller.

Figure 2.10 shows the block diagram of an adaptive filter used as an interference canceller. A received signal, containing a desired signal and an undesired interferer, is applied to the input $r(n)$. A (time-domain) estimate signal of the interferer is applied to the input $v(n)$. The adaptive filter aligns the estimate in phase and amplitude with the actual interferer contained in $r(n)$. A subtraction removes the interferer energy from the received signal and the cleaned signal appears at the (inappropriately named) error output, $e(n)$.

When the interferer estimate, $v(n)$, perfectly *represents* the interferer found in the received signal $r(n)$, the interference canceller is able to completely remove the interferer. To be more precise, the interference estimate $v(n)$ does not need to be equal to the interference, it may be scaled, rotated or skewed in the complex plane. Hence the term 'represents'.

The above statement is easily mathematically verified. To do so, suppose the received signal contains a desired baseband signal $z_1(n)$ and an undesired interferer $z_2(n)$:

$$r(n) = z_1(n) + \alpha \cdot z_2(n) \tag{2.25}$$

and we have, somehow, obtained an interference estimate that represents the interferer perfectly:

$$v(n) = \beta \cdot z_2(n), \tag{2.26}$$

where $\alpha \neq 0$ and $\beta \neq 0$ are a complex-valued coefficient that allows scaling, rotation and skewing.

By inspection of Fig. 2.10, the output of the canceller, $e(n)$, is:

$$e(n) = r(n) - w^*(n) \cdot v(n). \tag{2.27}$$

Given the inputs (2.25) and (2.26), the output can be written as:

$$e(n) = z_1(n) + \alpha \cdot z_2(n) - w^*(n) \cdot \beta \cdot z_2(n). \tag{2.28}$$

The undesired interference, $z_2(n)$, is completely removed when

$$w^*_{ideal}(n) = \frac{\alpha}{\beta}. \tag{2.29}$$

Often, either one or both of the coefficients α or β are unknown, making direct calculation of filter coefficient $w^*_{ideal}(n)$, using (2.29), impossible. However, it is possible to obtain an estimate of the filter coefficient by applying the statistical methods outlined in Sec. 2.4.3. Rather than focusing on this feed-forward method, a different method is explored here, namely that of adaptation using feedback.

2.5.2 Cost function optimization

The LMS adaptive filter, like many adaptive systems, optimizes its performance by minimizing a cost function with respect to the filter parameters. The cost function used is the mean squared value of the error output, hence the name of the adaptive algorithm. In mathematical terms, the cost function is equal to:

$$\begin{aligned} J(\mathbf{w}) &= \mathbf{E}\{|e(n)|^2\} \\ &= \mathbf{E}\{e(n)e^*(n)\} \end{aligned} \tag{2.30}$$

and the optimal coefficient vector $\mathbf{w}_{opt}$ is given by[2]:

$$\mathbf{w}_{opt} = \underset{\mathbf{w}}{\operatorname{argmin}}\, J(\mathbf{w}).$$

Thus, the optimum occurs when the mean of the squared output signal is minimized.

In case of the single-tap canceller in Fig. 2.10, the cost function becomes:

$$\begin{aligned} J(w(n)) &= \mathbf{E}\{|e(n)|^2\} \\ &= \mathbf{E}\{(r(n) - w^*(n) \cdot v(n)) \cdot (r^*(n) - w(n) \cdot v^*(n))\}, \end{aligned}$$

[2]argmin returns the value of the specified parameter for which the argument is minimum.

which can be expanded to:

$$\begin{aligned}\mathbf{E}\{|e(n)|^2\} = \mathbf{E}\{|r(n)|^2\} \\ - w^*(n) \cdot \mathbf{E}\{v(n) \cdot r^*(n)\} + w(n) \cdot \mathbf{E}\{v^*(n) \cdot r(n)\} \\ + |w(n)|^2 \cdot \mathbf{E}\{|v(n)|^2\}.\end{aligned} \tag{2.31}$$

Note that the cost function is a quadratic function of the filter coefficient and that the weight of $|w(n)|^2$ is always positive. Therefore, the cost function has exactly one minimum. If the expectations are known, the coefficient $w(n)$, for which the cost function is minimum can be found by directly solving the equations or by iterative methods which do not require division or the taking of square roots, such as the *steepest descent* algorithm.

Directly minimizing the cost function is achieved by setting the gradient to zero and solving for w. The gradient of the cost function (2.31) is (see Appendix A.2):

$$\frac{\partial J(w(n))}{\partial w(n)} = -2 \cdot \mathbf{E}\{v(n) \cdot r^*(n)\} + 2 \cdot w(n) \cdot \mathbf{E}\{|v(n)|^2\}. \tag{2.32}$$

Given the input signals (2.25) and (2.26), the minimization results in the following optimal filter coefficient:

$$\begin{aligned} w^*_{opt}(n) &= \frac{\mathbf{E}\{v^*(n) \cdot r(n)\}}{\mathbf{E}\{|v(n)|^2\}} \\ &= \frac{\beta^* \cdot \alpha}{|\beta|^2} \\ &= \frac{\alpha}{\beta}. \end{aligned} \tag{2.33}$$

Thus, the minimization of the cost function (2.30) results in the same filter coefficient as the previous method (2.29).

The above minimization technique requires a division operation, which can be avoided by using an iterative optimization method, such as the steepest descent algorithm. The steepest descent algorithm, in its stochastic form, is the basis of the LMS adaptive filter. The following section discusses the steepest descent algorithm in its regular form, before considering its stochastic form.

2.5.3 Minimization by steepest descent

The steepest descent algorithm minimizes a cost function $J(w)$ by choosing an initial solution w_0 and iteratively producing increasingly accurate solutions $w_{1\ldots n}$ by adjusting the previous solution in the direction of the negative gradient:

Algorithm Generic steepest descent algorithm for minimizing $J(w)$

$w_0 =$ initial guess to solution
for $i = 1$ to N **do**
  $w_i = w_{i-1} - \mu \cdot \frac{\partial J(w_{i-1})}{\partial w_{i-1}}$
end for

At each iteration, a new coefficient w_i is calculated, equal to the previous coefficient w_{i-1} and an adjustment based on the gradient, which is a function of w_{i-1}. The adjustment is governed by a step-size parameter μ. In effect, the steepest descent algorithm is a feedback system.

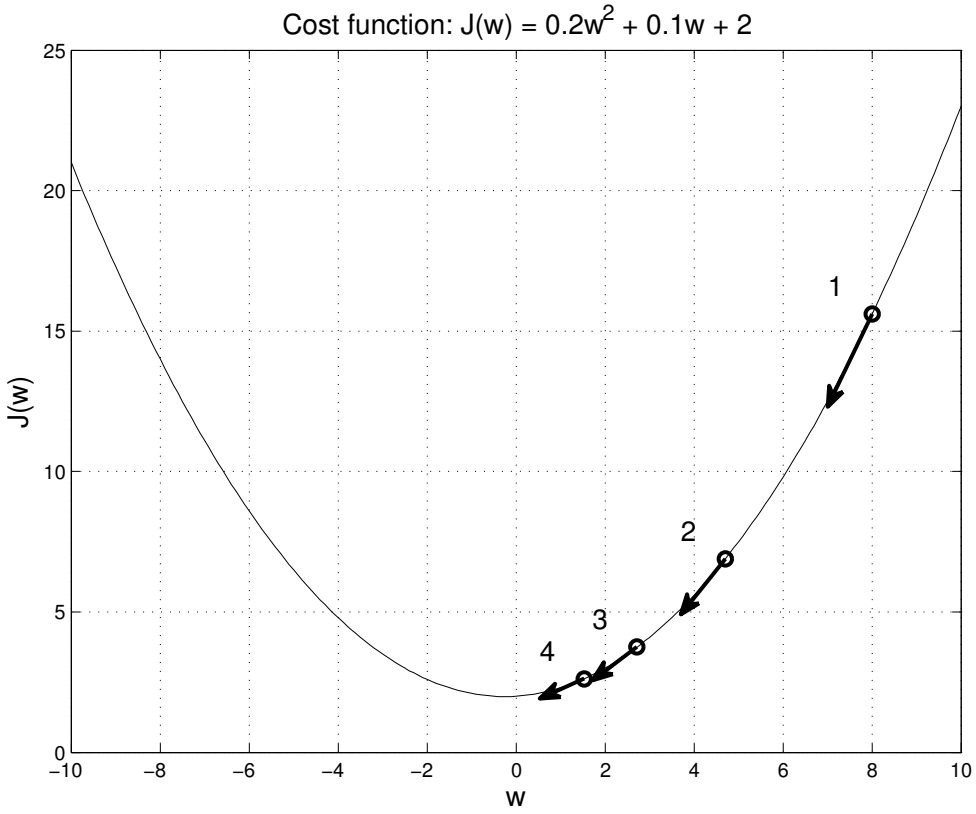

Figure 2.11: Steepest descent algorithm: circles indicate calculated points on the cost function, arrows indicate negative gradient. The gradient of the cost function is $0.4w + 0.1$. *The step-size* μ *and the initial solution were arbitrarily set to* 1 *and* 8, *respectively.*

As an example, figure 2.11 shows the first four iterations for a arbitrarily chosen real-valued cost function $J(w) = 0.2w^2 + 0.1w + 2$.

Application of the steepest-descent algorithm to the interference canceller in Fig. 2.10 for obtaining the filter coefficient $w^*(n)$ is done by substituting the specific gradient (2.32), which leads to:

Algorithm Steepest descent for obtaining $w^*(n)$ in Fig. 2.10

$w_0(n) =$ initial guess to solution
for $i = 1$ to M **do**
$w_i(n) = w_{i-1}(n) + 2\mu \cdot \left(\mathbf{E}\{v(n) \cdot r^*(n)\} - w_{i-1}(n) \cdot \mathbf{E}\{|v(n)|^2\}\right)$
end for
$w^*(n) = [w_M(n)]^*$

Note that the sample time index n and the expectations are constant during the iteration. Therefore, as long as the expectations are known, the algorithm is capable of calculating the optimal filter coefficient for each sample moment.

Lowpass filter interpretation

An important observation to make, is that the iterative weight update loop of the gradient descent algorithm constitutes, in fact, a first-order lowpass filter in the form of

$$w_i(n) = c_{fb} \cdot w_{i-1}(n) + x_i, \tag{2.34}$$

where the feedback coefficient

$$c_{fb} = 1 - 2\mu \cdot \mathbf{E}\{|v(n)|^2\}.$$

The input to the lowpass filter is a constant and is given by

$$x_i = 2\mu \cdot \mathbf{E}\{v(n) \cdot r^*(n)\}$$

and the filter has a z-domain transfer function

$$H(z) = \frac{1}{1 - c_{fb} \cdot z^{-1}},$$

which has a pole at $z = c_{fb}$ and a DC-gain of

$$H(0) = \frac{1}{2\mu \cdot \mathbf{E}\{|v(n)|^2\}}.$$

Because the input to the filter is a constant value, the step response determines the behavior in terms of convergence speed. Given the previous expressions, the step response converges to

$$x_i \cdot H(0) = \frac{\mathbf{E}\{v(n) \cdot r^*(n)\}}{\mathbf{E}\{|v(n)|^2\}}, \tag{2.35}$$

which is equal to the (unconjugated) optimal filter coefficient of the single-tap adaptive interference canceller.

The step response of the filter defines the convergence characteristic and speed; when the step-size μ is chosen closer to zero, the pole moves toward the center of the unit circle, the bandwidth of the filter decreases and the convergence becomes slower.

The stability of this particular steepest descent algorithm is guaranteed when $0 < \mu < \dfrac{1}{2 \cdot \mathbf{E}\{|v(n)|^2\}}$, see Appendix A.3.

2.5.4 Performance of the steepest-descent based interference canceller

To evaluate the performance of the steepest-descent based interference canceller, two scenarios will be considered. The first is where the interference estimate signal $v(n)$ consists of only interference, i.e. the interference estimate is perfect. The second is where the interference estimate contains energy from the desired signal. The latter scenario is the more common situation encountered in practical applications.

Scenario 1: a perfect interference estimate

Let the received signal $r(n)$ consist of a mixture of a desired baseband signal $z_1(n)$ and an undesired weighted interference signal $\alpha \cdot z_2(n)$, where the weighting coefficient α is unknown:

$$r(n) = z_1(n) + \alpha \cdot z_2(n).$$

And let the interference estimate be a perfect representation of the interference:

$$v(n) = \beta \cdot z_2(n).$$

For the expectations we have:

$$\mathbf{E}\{v(n) \cdot r^*(n)\} = \beta \cdot \alpha^* \cdot \sigma_{z_2}^2,$$
$$\mathbf{E}\{|v(n)|^2\} = |\beta|^2 \cdot \sigma_{z_2}^2.$$

which results in the following optimal (conjugated) filter coefficient:

$$w_{opt}^*(n) = \frac{\alpha}{\beta}.$$

The output of the canceller is then:

$$\begin{aligned} e(n) &= r(n) - w_{opt}^*(n) \cdot v(n) \\ &= z_1(n) + \alpha \cdot z_2(n) - \frac{\alpha}{\beta} \cdot (\beta \cdot z_2(n)) \\ &= z_1(n). \end{aligned} \tag{2.36}$$

Thus, if the interference estimate is perfect, the canceller is able to completely remove the interference. In practice, however, the interference estimate is almost never perfect and will contain a small amount of desired signal.

Scenario 2: a realistic interference estimate

A more realistic model of an interference estimate signal is one where a small amount of desired signal is present. In such a scenario the interference estimate signal becomes:

$$v(n) = \delta \cdot z_1(n) + \beta \cdot z_2(n),$$

where $|\delta|$ is much smaller than $|\beta|$. For the expectations we have:

$$\mathbf{E}\{v(n) \cdot r^*(n)\} = \delta \cdot \sigma_{z_1}^2 + \beta \cdot \alpha^* \cdot \sigma_{z_2}^2,$$

$$\mathbf{E}\{|v(n)|^2\} = |\delta|^2 \cdot \sigma_{z_1}^2 + |\beta|^2 \cdot \sigma_{z_2}^2,$$

so that the filter coefficient becomes:

$$w(n) = \frac{\delta \cdot \sigma_{z_1}^2 + \beta \cdot \alpha^* \cdot \sigma_{z_2}^2}{|\delta|^2 \cdot \sigma_{z_1}^2 + |\beta|^2 \cdot \sigma_{z_2}^2}, \tag{2.37}$$

When $|\delta| << |\beta|$ and the interference is large compared to the desired signal, $|\delta|^2 \cdot \sigma_{z_1}^2$ may be removed from the denominator without incurring a large error. This gives the following approximation $\widehat{w(n)}$ of the actual coefficient $w(n)$:

$$\widehat{w(n)} = \frac{\delta \cdot \sigma_{z_1}^2 + \beta \cdot \alpha^* \cdot \sigma_{z_2}^2}{|\beta|^2 \cdot \sigma_{z_2}^2}, \tag{2.38}$$

which may be conveniently split into a term which would result in perfect cancellation and a deviation term:

$$\widehat{w(n)} = \underbrace{\frac{\alpha^*}{\beta^*}}_{\text{perfect}} + \underbrace{\frac{\delta \cdot \sigma_{z_1}^2}{|\beta|^2 \cdot \sigma_{z_2}^2}}_{\text{deviation}} \tag{2.39}$$

From this expression, several conclusions can be drawn:

- The greater the desired signal leakage into the interference estimate, the larger the deviation.
- The greater the interference, the smaller the deviation.
- The deviation depends on the relative signal powers, i.e. the signal-to-interference ratio.

Using $\widehat{w(n)}$ as the filter coefficient, the output of the canceller is:

$$\begin{aligned} e(n) &= r(n) - \widehat{w^*(n)} \cdot v(n) \\ &= \left(1 - \frac{|\delta|^2 \cdot \sigma_{z_1}^2}{|\beta|^2 \cdot \sigma_{z_2}^2} - \frac{\alpha \cdot \delta}{\beta}\right) \cdot z_1(n) - \left(\frac{\delta^* \cdot \sigma_{z_1}^2}{\beta^* \cdot \sigma_{z_2}^2}\right) \cdot z_2(n) \end{aligned} \tag{2.40}$$

Assuming again that $|\delta| << |\beta|$ and $\sigma_{z_1}^2 < \sigma_{z_2}^2$, the above can be approximated by:

$$e(n) \approx \left(1 - \frac{\alpha \cdot \delta}{\beta}\right) \cdot z_1(n) - \left(\frac{\delta^* \cdot \sigma_{z_1}^2}{\beta^* \cdot \sigma_{z_2}^2}\right) \cdot z_2(n).$$

As shown by the presence of the interference $z_2(n)$ in the output of the canceller, the interference is not completely removed. The power of the interference at the output of the canceller is:

$$P_{interference} \approx \frac{|\delta|^2}{|\beta|^2} \cdot \frac{\sigma_{z_1}^4}{\sigma_{z_2}^2}, \tag{2.41}$$

which may be conveniently expressed in terms of the signal-to-interference ratio of the interference estimate, SIR_v:

$$P_{interference} \approx SIR_v \cdot \sigma_{z_1}^2 \qquad \text{with } SIR_v = \frac{|\delta|^2}{|\beta|^2} \cdot \frac{\sigma_{z_1}^2}{\sigma_{z_2}^2}, \tag{2.42}$$

The desired signal power at the output of the canceller is:

$$P_{desired} \approx \left(1 - 2 \cdot \Re\left\{\frac{\alpha \cdot \delta}{\beta}\right\} + \frac{|\alpha|^2 \cdot |\delta|^2}{|\beta|^2}\right) \cdot \sigma_{z_1}^2. \tag{2.43}$$

In a well-designed system, $|\delta| << 1$, so that

$$P_{desired} \approx \sigma_{z_1}^2. \tag{2.44}$$

Then, the signal-to-interference ratio at the output of the canceller is approximated by:

$$\begin{aligned} SIR_e &= \frac{P_{desired}}{P_{interference}} \\ &\approx \frac{\sigma_{z_1}^2}{SIR_v \cdot \sigma_{z_1}^2} \\ &\approx ISR_v \end{aligned} \tag{2.45}$$

Thus, the signal-to-interference ratio at the output of the canceller, is approximately equal to the interference-to-signal ratio of the interference estimate.

In fact, *the performance of the canceller depends only on* ***quality*** *of the interference estimate and* ***not*** *on the received signal*; an important relation indeed.

We will exploit this property in Chapters 3, 4 and 5 extensively.

Given (2.42) and (2.44), the total power at the output of the canceller, or the *minimum cost-function value* J_{min}, is then equal to

$$\begin{aligned} J_{min} &= P_{desired} + P_{interference} \\ &\approx (1 + SIR_v) \cdot \sigma_{z_1}^2 \end{aligned} \tag{2.46}$$

Experimental performance verification

Performance simulations were done using MATLAB to verify the performance relation found. The interference attenuation in the received signal was chosen to be 0 dB with a 45-degree phase shift, so that

$$\alpha = \frac{1}{2}\sqrt{2} + j \cdot \frac{1}{2}\sqrt{2}$$

and the interference contribution to the interference estimate was chosen to be 0 dB, so that

$$\beta = 1.$$

The interference and the desired signals are chosen to be white Gaussian noise signals of equal power, which means

$$\sigma_{z_1} = \sigma_{z_2} = 1.$$

The desired signal leakage parameter δ is swept from -50 to 0 dB and the SIR at the output of the canceller determined. For this system the SIR of the interference estimate is:

$$SIR_v = |\delta|^2.$$

Thus, the expected SIR at the output of the canceller is

$$SIR_e = \frac{1}{|\delta|^2}.$$

Figure 2.12 shown the results; the simulated performance of the signal-to-interference ratio at the output of the canceller is in accordance with the predicted value given by (2.45).

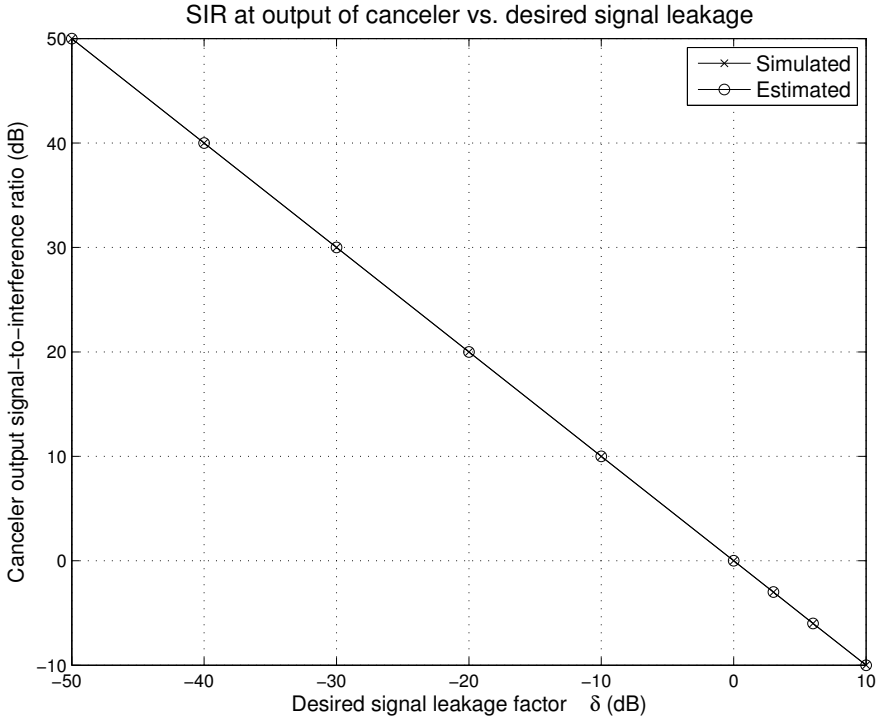

Figure 2.12: Signal-to-interference ratio at the output of the steepest-descent based canceller versus the desired signal leakage parameter δ. The remaining parameters are $\alpha = \frac{1}{2}\sqrt{(2)} + j \cdot \frac{1}{2}\sqrt{2}$, $\beta = 1$.

2.5.5 The LMS algorithm

In practice, the steepest descent algorithm cannot be applied directly as the expectations required are not known. The expectations could be estimated by using the sample variance and cross-correlation estimators outlined in Section 2.4. However, the steepest-descent algorithm can be modified into the *stochastic gradient descent* [25], which leads to a very simple and elegant adaptive system known as the LMS adaptive filter.

Stochastic gradient descent

The stochastic gradient algorithm uses the instantaneous values of the variables as a coarse approximation to their expectation:

$$\mathbf{E}\{|v(n)|^2\} \approx |v(n)|^2$$
$$\mathbf{E}\{v(n) \cdot r^*(n)\} \approx v(n) \cdot r^*(n)$$

These approximations are nothing more than the sample variance estimator of $v(n)$ and the cross-correlation estimator for $v(n)$ and $r^*(n)$, both based on a single sample. Because of the large error, these approximations cannot be applied to the steepest-descent algorithm directly as it would lead it to converge to an incorrect value. A solution is found by realizing that the approximations are unbiased and give the correct value *in the mean*. If the signals $v(n)$ and $r(n)$ are wide-sense stationary and ergodic, accurate results can be obtained by reducing the approximation variance through lowpass filtering in the time domain.

The stochastic gradient algorithm makes use of the fact that the weight update loop of the steepest-descent algorithm has a lowpass characteristic, which will filter out a large portion of the approximation noise. The stochastic gradient algorithm for the single-tap adaptive interference canceller is obtained by applying the approximations to the steepest-descent algorithm and iterating over time.

Algorithm LMS algorithm for the adaptive interference canceller in Fig. 2.10

$w(0) =$ initial guess to solution
loop
  $w(n+1) = w(n) + 2\mu \cdot \left(r^*(n) \cdot v(n) - w(n) \cdot |v(n)|^2\right)$
  $n = n + 1$
end loop

This algorithm implicitly includes the calculation of the interference canceller output $e(n)$. The canceller output may be made explicit by substituting

$$r^*(n) \cdot v(n) - w(n) \cdot |v(n)|^2 = e^*(n) \cdot v(n)$$

and including the interference canceller $e(n) = r(n) - w^*(n) \cdot v(n)$ within the loop:

Algorithm LMS algorithm for the adaptive interference canceller in Fig. 2.10

$w_0(n) =$ initial guess to solution
loop
$e(n) = r(n) - w^*(n) \cdot v(n)$
$w(n+1) = w(n) + 2\mu \cdot e^*(n) \cdot v(n)$
$n = n + 1$
end loop

Figure 2.13 shows a block diagram of the single-tap canceller with the LMS weight update algorithm.

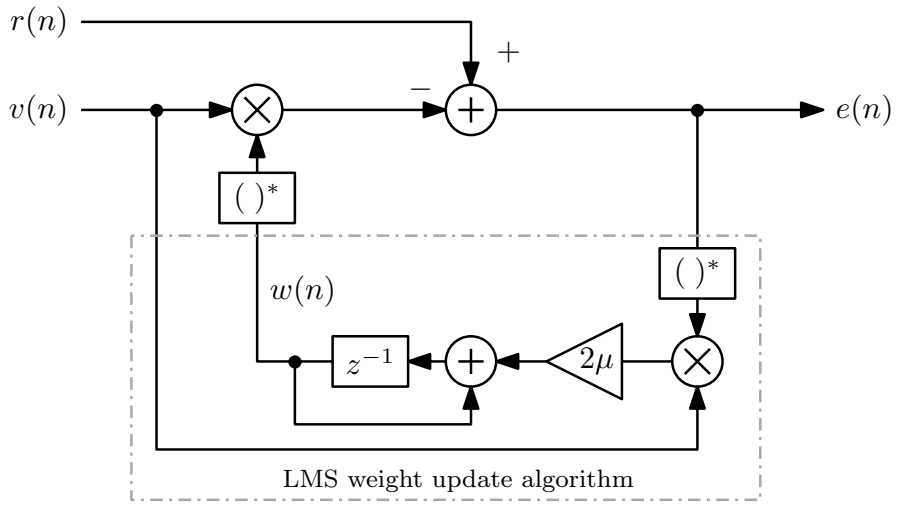

Figure 2.13: A block diagram of the single-tap adaptive interference canceller and its LMS weight update algorithm.

2.5.6 Performance of an LMS-based interference canceller

Due to the coarse nature of the approximations for the expectations, the LMS algorithm will never produce filter coefficients that are better than the steepest-descent algorithm. However, by making the step-size parameter μ very small with respect to the variance of $v(n)$, the cutoff frequency of the lowpass filter action will be very low, resulting in increased filter coefficient accuracy at the expense of the convergence rate. This trade-off is present in all LMS-based algorithms.

The performance of the LMS adaptive filter is notoriously difficult to analyze. Indeed, according to [25], page 259:

> ... although the LMS filter is very simple in physical terms, its mathematical analysis is profoundly complicated because of its highly nonlinear nature. Indeed, despite the extensive effort that has been expended in the literature to analyze the LMS filter, we still do not have a direct mathematical analysis of its stability and steady-state performance, and quite probably we never will.

Under several assumptions, some of them clearly false, the performance penalty of the LMS algorithm can be expressed in its *misadjustment* [25], denoted by $\mathcal{M}$. The misadjustment is the ratio defined by

$$\mathcal{M} = \frac{J_{ex}}{J_{min}},$$

where J_{ex} is the steady-state excess mean-square error. In other words, the misadjustment is a ratio (usually expressed as a percentage) that identifies how much the LMS algorithm deviates from the optimum mean-square error, J_{min}.

According to Section 5.4 in [25], the misadjustment may be expressed as:

$$\mathcal{M} \approx \mu \cdot \mathbf{E}\left[\|\mathbf{u}(n)\|^2\right],$$

where $\mathbf{u}(n)$ is the filter state vector. In other words, the misadjustment is equal to the step size times the average energy contained in the adaptive filter states.

The single-tap canceller has only a single state which is equal to the interference estimate signal. Thus, $\|\mathbf{u}(n)\|^2 = |v(n)|^2$. Therefore, the misadjustment for the single-tap filter is approximately equal to:

$$\begin{aligned}\mathcal{M} &\approx \mu \cdot \sigma_v^2 \\ &\approx \mu\left(|\delta|^2 \cdot \sigma_{z_1}^2 + |\beta|^2 \cdot \sigma_{z_2}^2\right). \end{aligned} \tag{2.47}$$

Summarizing the above, the misadjustment is proportional to the power of the interference estimate $v(n)$. Most importantly, the smaller the step-size parameter μ, the smaller the misadjustment. Typically, it is desirable to have a misadjustment that is lower than 10% of the interference estimate, i.e. $\mu < \frac{1}{10} \cdot \sigma_v^2$.

For a full derivation of the misadjustment and the underlying assumptions made, the reader is directed to [25], Section 5.4.

Assuming the interference estimate $v(n)$ mostly consists of interference, any misadjustment will increase the interference contribution to the output of the canceller, thereby increasing the average error power:

$$J_{lms} = (1 + \mathcal{M}) \cdot J_{min}$$

and

$$P_{interference,lms} \approx \underbrace{P_{interference,opt}}_{\text{due to leakage}} + \underbrace{\mathcal{M} \cdot (1 + SIR_v) \cdot \sigma_{z_1}^2}_{\text{due to misadjustment}}$$

Experimental misadjustment verification

Even though some of the assumptions made in the derivation of the misadjustment are questionable at best, (2.47) is still reasonably accurate. To demonstrate this, the system from Section 2.5.4 is used to simulate the misadjustment and interference power at the output of the canceller over 100 trials.

Like the previous simulations, the desired signal $z_1(n)$ and the interference signal $z_2(n)$ have unity variance. The desired signal leakage parameter δ was set to -30 dB and the step size was set to $\mu = 0.001$.

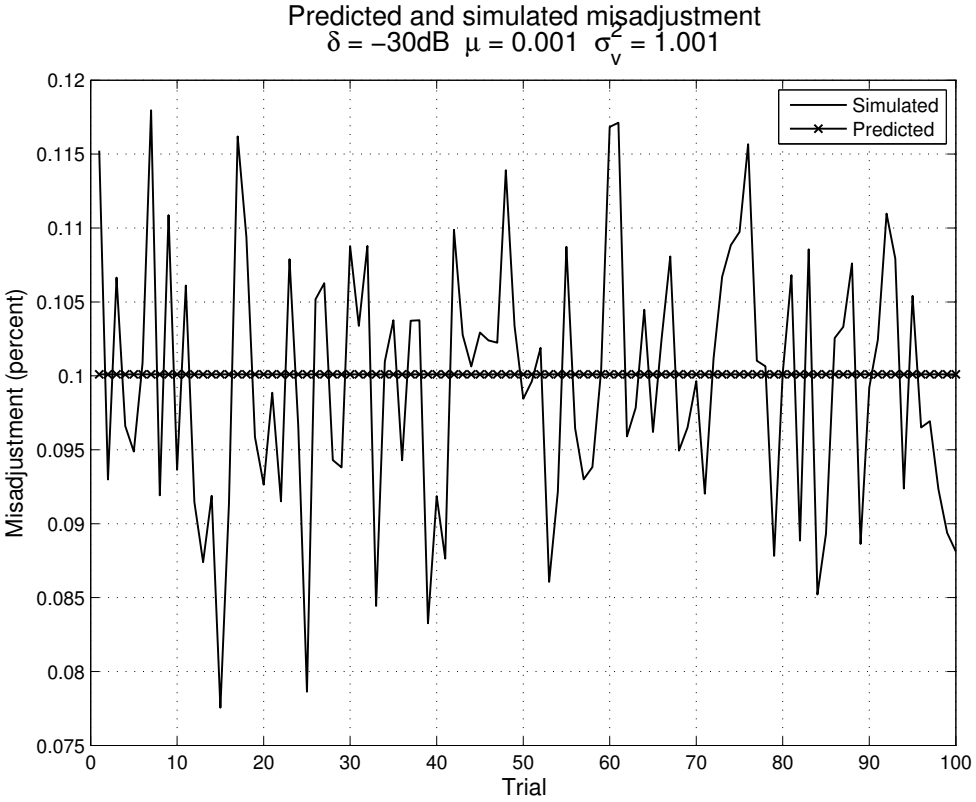

Figure 2.14: Misadjustment simulation based on 100 trials, each consisting of N=65536 samples.

The mean simulated misadjustment over 100 trials was 0.0982 percent, while the predicted misadjustment was 0.1 percent. The mean interference output power, simulated over 100 trials, was 0.001952 while the predicted interference output power was 0.001958. Thus, theory is in accordance with the simulation results and we can be confident our derivations are correct.

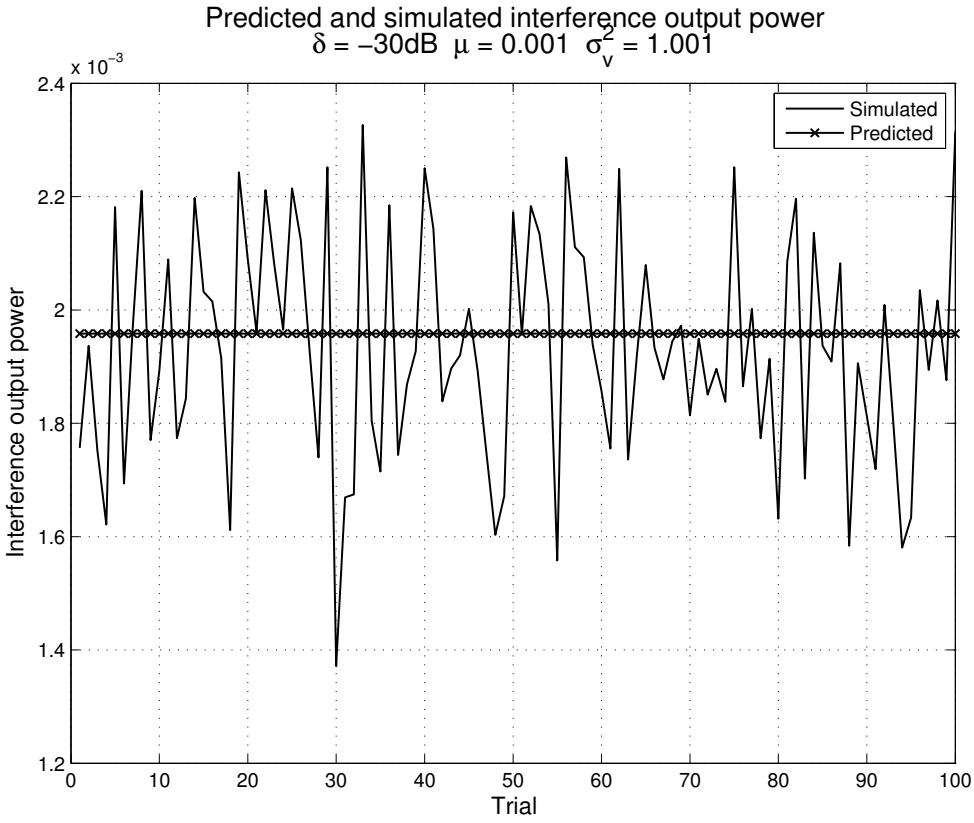

Figure 2.15: Interference power simulation based on 100 trials, each consisting of N=65536 samples.

2.6 Conclusions

This chapter briefly introduced some important concepts and properties of adaptive systems, some of which were proven by mathematics or made plausible by experimental verification through simulations. The systems discussed were specifically tailored toward the later chapters in which the algorithms are applied to harmonic image rejection and spectral sensing.

The astute reader will have noticed that during the treatment of the adaptive interference canceller nothing was mentioned on *how* to obtain a good interference estimate signal $v(n)$, or how to apply the interference canceller to the problem of harmonic image rejection. These are the subjects of the next three chapters.

Chapter 3

Harmonic Image Rejection using Adaptive Interference Cancellation

3.1 Prologue

This chapter appeared in Transactions on Circuits and Systems II: Express Briefs [35] and is a complete reproduction thereof.

The Fourier coefficients for the LO pulse wave mentioned in this chapter can be found in Appendix A.4.

3.2 Introduction

Wireless receivers must have good harmonic rejection (HR). When the HR is insufficient, signals present at multiples of the local oscillator (LO) frequency ω_{LO} will be down-mixed to baseband thus causing interference to the desired signal. In a direct-conversion receiver, the HR is determined by the amount of RF filtering and the LO waveform of the mixer.

In traditional single-band receiver frontends, a fixed high-order RF filter is sufficient to attain good HR. Multi-band receivers require, a tracking RF filter or multiple RF filters. Such active RF tracking filters typically consume a lot of power [36] and take up much die or board space, which makes both solutions unattractive for CMOS integration.

The requirements of the RF filters are exacerbated by the use of square waves as the LO waveform or the use of switching mixers in the front-end [37]. In a direct-

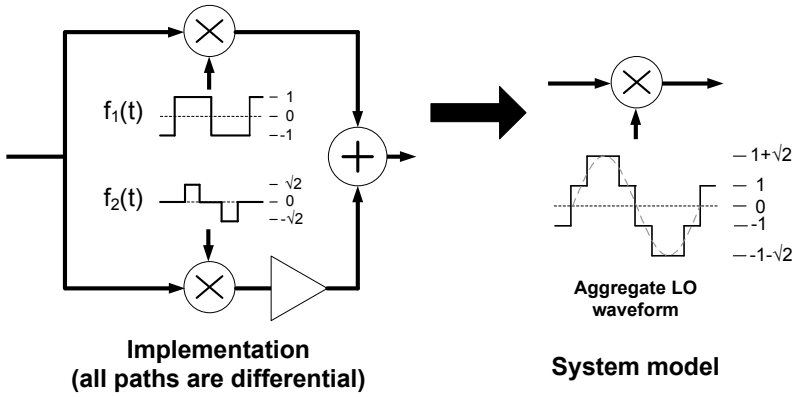

Figure 3.1: Modeling a set of parallel mixers as a single mixer. The single mixer is driven by the aggregate *effective LO waveform.*

conversion receiver, the (baseband) output of the mixer is the convolution of the effective LO waveform spectrum with the RF spectrum at the antenna. Thus, the harmonic content of the effective LO waveform determines which frequencies are mixed down to baseband. As the effective local oscillator contains many strong harmonics, the mixer offers less HR compared to a multiplier with a sinusoidal LO. Still, square waves are preferred over sinusoids, especially for flexible spectrum access [37], because the former are easier to produce over a wide frequency range in an IC using digital circuits.

Unwanted mixing products, such as the 3^{rd} and 5^{th} harmonic images, can be canceled by using multiple mixers. Each mixer is driven by a LO square wave of different duty cycle. Their outputs are combined in a weighted sum to form the final output. Provided the mixers operate linearly from RF to IF, this parallel mixer structure may be treated as a single mixer from a system point-of-view. The effective *aggregate* LO waveform, is simply the weighted sum of the individual LO waveforms, see Fig. 3.1.

The duty cycles and weights of each LO waveform are chosen so that the aggregate LO waveform contains a reduced set of harmonics. The more mixing paths are introduced, the less harmonics are present in the aggregate waveform. In practice, the LO signals are generated using a multi-phase clock generator. This technique has been successfully applied in CMOS transmitters [38] and in receivers [24, 12].

In [24], the average harmonic rejection across 10 chips is around 40 dB and in [12] the HR ratio is around 42 dB. This is often not enough. Suppose you want to receive a TV signal at $900/3 = 300$ MHz. A nearby GSM transmitter at about 900 MHz can produce up to 0 dBm at the antenna. It will completely corrupt the TV signal.

In this paper, we present a new HR topology. In addition to HR in the analog domain, we obtain additional HR in the *digital* domain. A digital solution was chosen because of the need for high-accuracy signal manipulation. It requires a second obser-

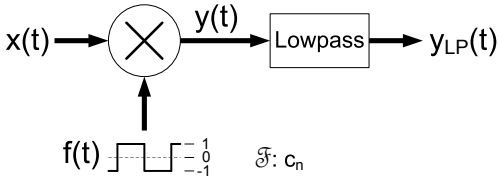

Figure 3.2: Block diagram of a mixer with a square wave LO.

vation of the complex baseband signal in order to reduce the interference caused by the residual harmonic images. This observation is produced by means of two analog subtractors and two additional ADCs.

In the next section, we will introduce a system model of a single mixer. In Section III, the extended multi-path mixer is explained. Section IV explains the digital algorithm. This is followed by Section V, which presents our simulation results. Finally, Section VI offers the conclusions.

3.3 Mixers - a system model

The (differential) mixer shown in Fig. 3.2 is driven by a square wave $f(t)$. The input $x(t)$ is multiplied by the LO $f(t)$ to form the output $y(t)$.

Consider an RF input signal $x(t)$ consisting of $n = 1 \dots N$ baseband-equivalent signals $z_n(t)$:

$$\begin{aligned} x(t) &= \sum_{n=1}^{N} \Re\left\{ z_n(t) \cdot e^{j\,\omega_{LO}\,n\,t} \right\} \\ &= \frac{1}{2} \sum_{n=1}^{N} z_n(t) \cdot e^{j\,\omega_{LO}\,n\,t} + z_n^*(t) \cdot e^{-j\,\omega_{LO}\,n\,t} \end{aligned} \tag{3.1}$$

where $\Re$ denotes the real part, ω_{LO} is the LO frequency in rad/s and * denotes the complex conjugate. The RF signal corresponding to $z_n(t)$ can be found at a multiple of the LO frequency, namely $n \cdot \omega_{LO}$.

Also consider the LO signal $f(t)$ as its Fourier series:

$$f(t) = c_0 + \sum_{n=1}^{\infty} c_n^* \cdot e^{-j\,\omega_{LO}\,n\,t} + c_n \cdot e^{j\,\omega_{LO}\,n\,t} \tag{3.2}$$

where c_n are the Fourier series coefficients of the LO waveform.

The output after the lowpass filter $y_{LP}(t)$ is calculated by multiplying (3.1) by (A.17) and removing the high-frequency components:

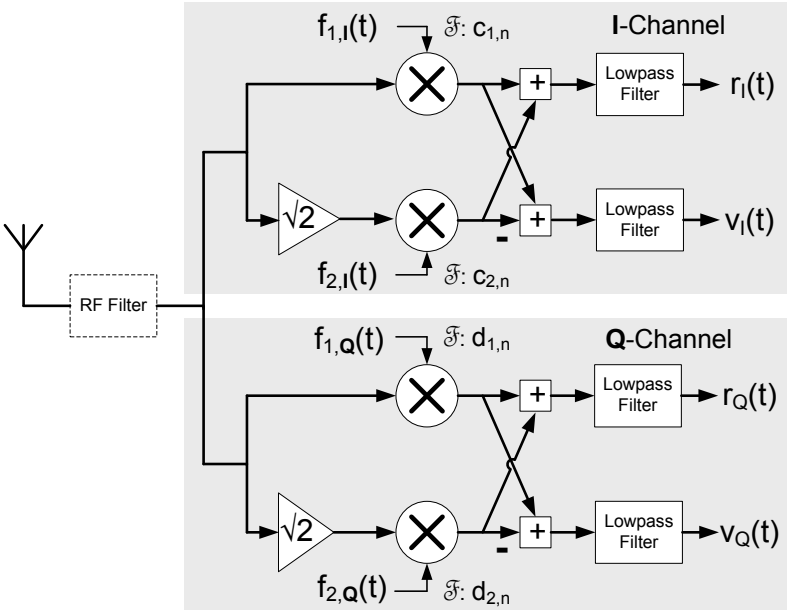

Figure 3.3: A quadrature harmonic rejection mixer topology. The LO waveforms are denoted by $f_{1,I}(t)$, $f_{2,I}(t)$, $f_{1,Q}(t)$ and $f_{2,Q}(t)$. Their Fourier series coefficients are $c_{1,n}$, $c_{2,n}$, $d_{1,n}$ and $d_{2,n}$ respectively.

$$y_{LP}(t) = \frac{1}{2}\sum_{n=1}^{\infty} c_n^* \cdot z_n(t) + c_n \cdot z_n^*(t) \tag{3.3}$$

Equation 3.3 shows that the strength of the harmonic images down mixed to baseband depend on the Fourier series of the LO waveform. For instance, when the 3$^{\text{rd}}$ harmonic is absent from the LO waveform ($c_3 = 0$), the third harmonic image $z_3(t)$, found at an RF frequency of $3\,\omega_{LO}$ rad/s, will not be present in the baseband signal $y_{LP}(t)$.

3.4 A quadrature harmonic-rejection mixer

Consider the harmonic-rejection mixer block diagram shown in Fig. 3.3. The RF signal present at the antenna passes through an RF filter after which it is distributed across four mixers. The top two mixers produce the in-phase channel $r_I(t)$ while the bottom two mixers produce the quadrature channel $r_Q(t)$. For now, we will ignore $v_I(t)$ and $v_Q(t)$.

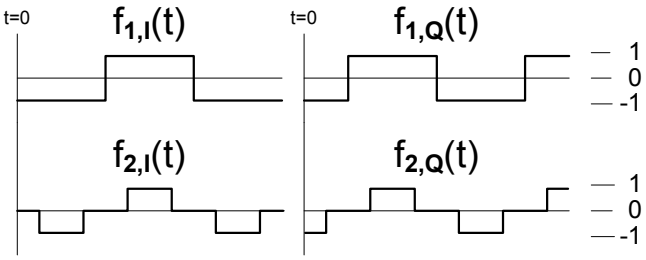

Figure 3.4: Effective LO waveforms of the I-channel ($f_{1,I}(t)$, $f_{2,I}(t)$) and the Q-channel ($f_{1,Q}(t)$, $f_{2,Q}(t)$).

The Fourier series coefficients of the aggregate LO waveform of the I-channel, α_n, and those of the Q-channel, β_n, can be expressed as functions of the Fourier series coefficients of the mixer LO waveforms $f_{1,I}(t)$, $f_{2,I}(t)$, $f_{1,Q}(t)$ and $f_{2,Q}(t)$, which are $c_{1,n}$, $c_{2,n}$, $d_{1,n}$, and $d_{2,n}$ respectively. By inspection of Fig. 3.3, $r_I(t)$ and $r_Q(t)$ are found to be:

$$r_I(t) = \frac{1}{2}\sum_{n=1}^{\infty} \alpha_n^* \cdot z_n(t) + \alpha_n \cdot z_n^*(t)$$
$$r_Q(t) = \frac{1}{2}\sum_{n=1}^{\infty} \beta_n^* \cdot z_n(t) + \beta_n \cdot z_n^*(t)$$

,where

$$\alpha_n = c_{1,n} + \sqrt{2}\, c_{2,n} \qquad \beta_n = d_{1,n} + \sqrt{2}\, d_{2,n} \tag{3.4}$$

Thus, the complex baseband output $r(t) = r_I(t) + j \cdot r_Q(t)$ is equal to:

$$r(t) = \frac{1}{2}\sum_{n=1}^{\infty} (\alpha_n - j\,\beta_n)^* \cdot z_n(t) + (\alpha_n + j\,\beta_n) \cdot z_n^*(t) \tag{3.5}$$

Given the LO waveforms shown in Fig. 3.4, it can be shown that $\alpha_n = 0$ and $\beta_n = 0$ when:

$$n \in \{3 + 8k, 5 + 8k \mid k \in \mathbb{N}\} \tag{3.6}$$

or when n is even. As a result, the even-order, 3^{rd} and 5^{th} harmonic images are rejected. The first uncanceled harmonic image is the 7^{th}. Thus, the complex baseband output $r(t)$ only contains the desired signal assuming that the RF filter at the antenna removes the 7^{th} and higher harmonic images. The RF filter requirements are greatly relaxed compared to a single-mixer case where the filter would have to remove the 3^{rd} and higher harmonic images, assuming a perfect differential system.

3.4.1 Achievable harmonic rejection ratio

Unfortunately, complete rejection of the harmonic images as specified by (3.6) through the principle outlined above, only applies when the LO waveforms $f_{1,I}(t)$, $f_{2,I}(t)$, $f_{1,Q}(t)$ and $f_{2,Q}(t)$ are exactly as specified in [38].

In practice, the LO waveforms are derived from an eight-phase clock. Such a multi-phase clock has dynamic and static timing errors. These errors reduce the amount of HR. In [39] it is shown that static timing errors are typically dominant over dynamic timing errors.

Assuming the multi-phase clock frequency is exact, seven out of the eight clock edges can have static timing errors, $\tau_{1..7}$, as there are seven degrees of freedom. A second source of error that limits the HR ratio is a deviation in the required $1 : \sqrt{2}$ ratio between the paths, see Fig. 3.3. A perfect $1 : \sqrt{2}$ ratio is hard to achieve in hardware owing to component mismatches and the fact that $1 : \sqrt{2}$ is an irrational ratio.

In addition to limiting the achievable HR, the aforementioned errors also cause I/Q imbalance. There exist many solutions to the I/Q imbalance problem and we will therefore not cover I/Q imbalance here. Instead, we refer to [32, 40] and the references therein.

3.4.2 Improving the harmonic rejection

The harmonic rejection ratio (HRR) can be improved by admittance scaling [41, 39] the clock generator and mixer circuits at the cost of increased power consumption. Scaling the admittance of a circuit by a factor λ decreases the amplitude mismatch by a factor $\sqrt{\lambda}$ and increases its power consumption by a factor λ. The same holds for timing mismatch errors. However, increasing the HR performance considerably, e.g. from 40 to greater than 70 dB, through admittance scaling (i.e. wider transistors) would increase the power consumption from milliwatts to Watts, which is clearly undesirable.

A second approach to improve the HRR is to calibrate the timing of the multi-phase clock using analog techniques. This solution requires many calibration points within the circuit as each clock edge must be controlled. A purely digital HRR-enhancement technique is preferable because it is more scalable and easier to migrate to a new IC process. It can also be designed independently from the analog front-end.

We present such a technique based on interference cancellation in the next section.

3.5 An interference cancellation technique for additional harmonic rejection

Interference cancellation techniques based on LMS adaptive filtering have been used in a wide variety of situations, such as active noise canceling [26], beam forming and radar [20]. The basic concept is to subtract an estimate of the interferer from the contaminated desired signal, see Fig. 3.5. Before the interference estimate can be subtracted from the contaminated signal, it must be scaled and rotated by a filter to remove any phase or amplitude difference between the interference in the two paths. This is achieved by an adaptive filter.

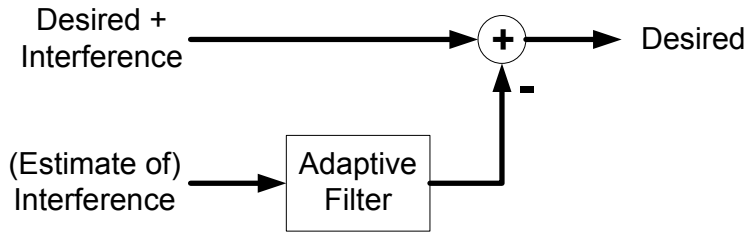

Figure 3.5: The concept of interference canceling.

In our application, the contaminated desired signal is $r(t)$ and the estimate of the interference is $v(t) = v_I(t) + j \cdot v_Q(t)$. The signal $v(t)$ is produced by subtracting instead of adding the paths as is shown in Fig. 3.3. The signal $v(t)$ can be expressed as:

$$v(t) = \frac{1}{2} \sum_{n=1}^{\infty} (\delta_n - j\,\gamma_n)^* \cdot z_n(t) + (\delta_n + j\,\gamma_n) \cdot z_n^*(t) \tag{3.7}$$

$$\text{where} \qquad \delta_n = c_{1,n} - \sqrt{2}\,c_{2,n} \qquad \gamma_n = d_{1,n} - \sqrt{2}\,d_{2,n}$$

The signals that are attenuated in $r(t)$ are not attenuated in $v(t)$ and vice-versa. So, $v(t)$ forms an estimate of the interference as the desired signal is attenuated, while the interference is not.

From (3.5), it is clear that the desired signal contains both the signals $z_n(t)$ and their complex conjugates $z_n^*(t)$. In order to reject the harmonic images, both $z_n(t)$ and $z_n^*(t)$ for $n > 1$ must be canceled by the interference canceler. Thus, we must apply two-input MISO interference canceling [42, 25], where $v(t)$ and $v^*(t)$ serve as the two inputs.

Before we can supply the digital interference canceler with the signals $v(t)$ and $r(t)$, we must convert to the digital domain using two analog-to-digital converters (ADCs) with complex-valued inputs.

3.5.1 From analog to digital

The two complex analog signals $r(t)$ and $v(t)$ are sampled by four ADCs. The ADCs share a common clock and are therefore synchronized. Assuming that the anti-aliasing filters in front of the ADCs are perfect, we have two complex discrete-time signals $\bar{r}(k)$ and $\bar{v}(k)$, which are defined as:

$$\bar{r}(k) = r(k\,\tau_{sample}) \qquad \bar{v}(k) = v(k\,\tau_{sample})$$

where τ_{sample} is the time (in seconds) between each sample of the ADCs and k is the sample index.

We will simply write $r(k)$ and $v(k)$ instead of $\bar{r}(k)$ and $\bar{v}(k)$ from this point onward as the remainder of the paper focuses on discrete-time digital signal processing only.

The quantization noise in $\bar{v}(k)$ needs to be lower than the desired additional HR achieved by the digital part. The additional ADCs, used to sample $v(k)$, require at least $\lceil \frac{S}{6} \rceil$ bits, where S is the minimum desired suppression in dB and $\lceil . \rceil$ denotes rounding up to the nearest integer.

3.5.2 The digital interference canceler

Figure 3.6 shows the proposed discrete-time HR structure. It comprises two one-tap complex FIR filters, a complex-conjugate operator block (to produce $v^*(k)$) and an adder with two negating inputs. The filter weights w_1 and w_2 rotate and scale $v(k)$ and $v^*(k)$ such that the phase and amplitude of the strongest harmonic image lines up with the same harmonic image in $r(k)$. In effect, the power of the strongest harmonic image is greatly reduced in the output signal $e(k)$. The output $e(k)$ can be written as:

$$e(k) = r(k) - w_1^* \cdot v(k) - w_2^* \cdot v^*(k) \tag{3.8}$$

As each harmonic image in $v(k)$ has a different phase and amplitude with respect to $r(k)$, each harmonic image requires a different value of w_1 and w_2 to cancel. In effect, the interference canceler can reject only one harmonic image. This may seem like a big disadvantage but the probability that more than one very strong harmonic image is present at RF is quite low. Also consider the fact that the analog part already provides 40 dB of rejection and that this does not include the additional rejection offered by an RF filter.

3.5.3 Obtaining the filter weights w_1 and w_2

The filter weights w_1 and w_2 are estimated using the LMS adaptive filter algorithm [25]. This algorithm was chosen for its simple implementation in hardware, its robustness and the fact that the convergence conditions are well-understood.

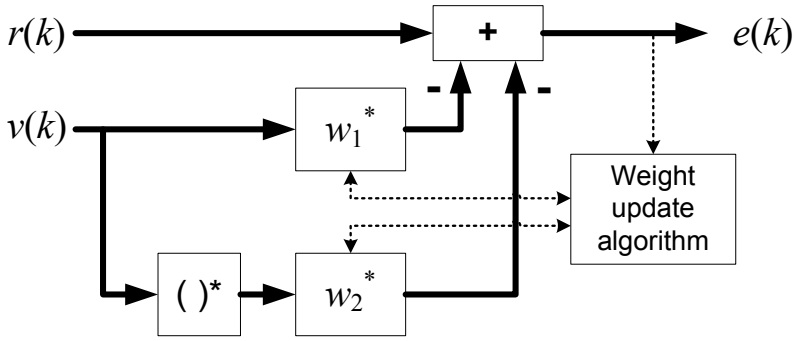

Figure 3.6: The digital harmonic rejection structure

The optimum (in the mean-square sense) filter weights $\mathbf{w}_{opt}$ are obtained by minimizing the following cost function [25] with respect to $\mathbf{w}$:

$$J(\mathbf{w}) = E\left\{|r(k)|^2 - \mathbf{w}^H\mathbf{p} - \mathbf{p}^H\mathbf{w} + \mathbf{w}^H\mathbf{R}\mathbf{w}\right\} \tag{3.9}$$

where

$$\mathbf{w} = \begin{bmatrix} w_1 \\ w_2 \end{bmatrix} \qquad \mathbf{p} = \begin{bmatrix} E\{v(k)r^*(k)\} \\ E\{v^*(k)r^*(k)\} \end{bmatrix} \tag{3.10}$$

$$\mathbf{R} = \begin{bmatrix} E\left\{|v(k)|^2\right\} & E\left\{v^2(k)\right\} \\ E\left\{(v^*(k))^2\right\} & E\left\{|v(k)|^2\right\} \end{bmatrix} \tag{3.11}$$

,H denotes the Hermitian operator and $E\{.\}$ denotes the expectation operator.

Note that $\mathbf{p}$ and $\mathbf{R}$ can be expressed as functions of the α_n, β_n, δ_n and γ_n coefficients. Due to limited article space, this is left as an exercise for the reader. As the coefficients depend on the LO static timing errors and mismatches in the $1 : \sqrt{2}$ ratio, the algorithm is able to compensate for both.

The LMS adaptive filter algorithm [25] minimizes (3.9) without requiring explicit knowledge of the statistics in (3.10) and (3.11) by using the following filter update rule:

$$\hat{\mathbf{w}}(k+1) = \hat{\mathbf{w}}(k) + \mu\mathbf{v}(k)e^*(k) \tag{3.12}$$

where the learning coefficient $\mu < (E\{|v(k)|^2\})^{-1}$ for stability, $\hat{\mathbf{w}}(k)$ is an estimate of $\mathbf{w}_{opt}$ at time k and

$$\mathbf{v}(k) = \begin{bmatrix} v(k) \\ v^*(k) \end{bmatrix} \tag{3.13}$$

To evaluate the HR performance of the algorithm, simulations were performed.

3.6 Simulations

The LMS adaptation coefficient μ is chosen to be $10^{-4} \cdot E\{|v(k)|^2\}^{-1}$. This proved to be a good tradeoff between convergence speed and accuracy.

In order to verify that our algorithm works, we performed a simulation of the HR mixer and compensator. The static timing errors $\tau_{1..7}$ of the multi-phase clock generator are drawn from a zero mean gaussian distributed process with a standard deviation equal to 0.5% of the aggregate LO period. The $1 : \sqrt{2}$ ratio was approximated by 1 : 1.4. This results in HR figures from 30 to 40 dB for the analog part. The simulations do not include an RF filter.

In the first simulation, five sinusoidal signals (the desired and four harmonic images) are present at the antenna. Their baseband frequencies are 0.05, 0.10, 0.15, 0.20 and 0.25 cycles/sample, respectively. Their signal strengths are 0 dB with respect to the unit-variance desired signal ($\sigma^2_{desired} = 1$), except for the 3rd harmonic image, which is 50 dB. This scenario represents a typical case where there is one very strong interferer and several weaker ones. Complex AWG noise $\sigma^2_{noise} = 10^{-5}$ is added to each baseband-equivalent signal to simulate RF noise. This figure was chosen low to be able to show clear signal spectra. The ADCs have an infinite number of bits.

Figure 3.7 shows the spectra of the mixer output $r(k)$, the interference output $v(k)$ and the compensated output $e(k)$. From the $r(k)$ spectrum, it is clear that the HR offered by the analog mixer is not sufficient. The 3rd harmonic image is 10.4 dB stronger that the desired signal. The v(k) signal indeed estimates the interference: the desired signal is suppressed while the 3rd and 5th harmonic images are boosted.

The dominating signal in the compensated signal $e(k)$ is the desired signal, as shown by its spectrum in Fig. 3.7. The 3rd harmonic image is found at -76.9 dB, which is a decrease of 87.3 dB. As the other harmonic images are not rejected, the final signal-to-interference ratio will be determined by these images.

To show the systems works with a modulated signal and realistic ADC quantization errors, the desired signal is changed to a random 16-QAM signal. Given 35 dB of analog HR and 50 dB stronger interference, we require 35 dB of digital HR for a 20 dB SNR so 6 bits are needed for the additional ADCs. The main ADCs use 10 bits. The constellation diagrams of $r(k)$ (left) and $e(k)$ (right) are shown in Fig. 3.8. The constellation plot of $e(k)$ clearly shows a 16-QAM constellation, while the $r(k)$ plot does not. As ADC power scales with 2^{bits}, the additional ADCs add an insignificant amount of power to the system while they improve the total HR performance greatly.

The signal-to-interference ratio (SIR) after compensation depends on the RF scenario, the $1 : \sqrt{2}$ ratio errors and the timing errors $\tau_{1..7}$. Therefore, a simple performance estimate of the SIR is not tractable. However, an indication of the compensator's performance can be given in the form of a SIR scatter plot and its distribution, as shown in Fig. 3.9. The plots were produced by taking 1000 different realizations of $\tau_{1..7}$ and determining the SIR of $r(k)$ and $e(k)$ for each realization. The RF scenario was kept the same as used in Fig. 3.7 and the ADCs use an infinite number of bits. From the histogram it is clear that the compensation structure provides an increase

of more than 36 dB in 90% of the cases. The mean SIR at the output $e(k)$ is 30.3 dB, an increase of 41.9 dB.

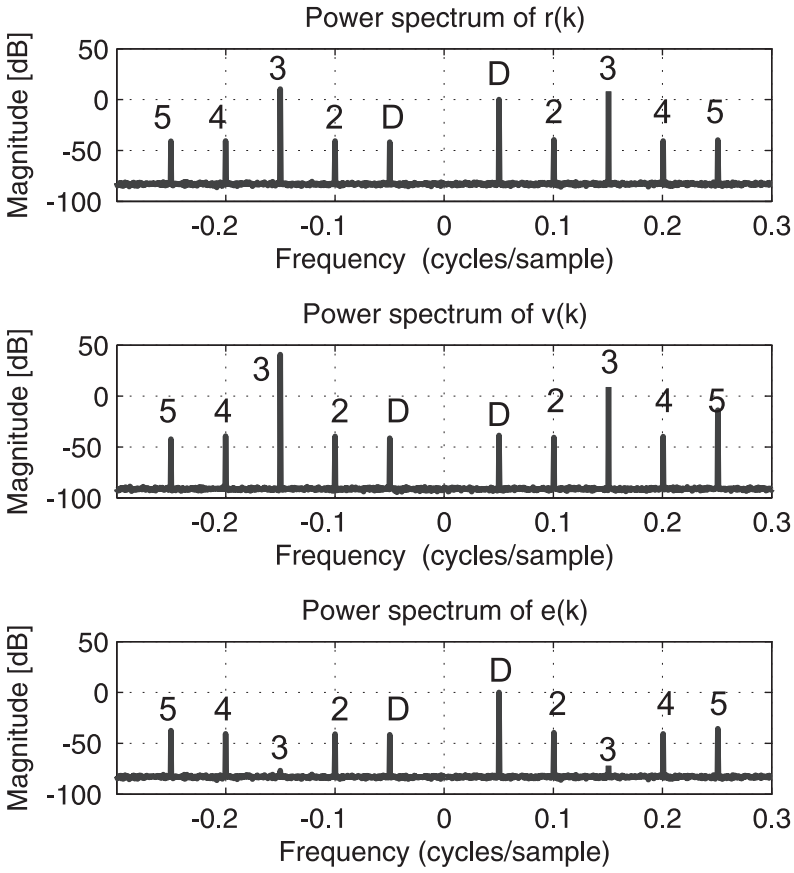

Figure 3.7: Baseband spectra of $r(k)$, $v(k)$ and $e(k)$. The baseband-equivalent desired signal has unit variance $\sigma_d = 1$ at the antenna. The remaining RF signal strengths are: 2nd = 0 dB, 3rd = 50 dB, 4th = 0 dB, 5th = 0 dB w.r.t the desired signal. The signals are indicated by 'D','2','3','4' and '5', respectively. All signals are sinusoidal. The baseband frequencies of the signals are 0.05, 0.10, 0.15, 0.20 and 0.25 cycles/sample. The ADCs have an infinite number of bits.

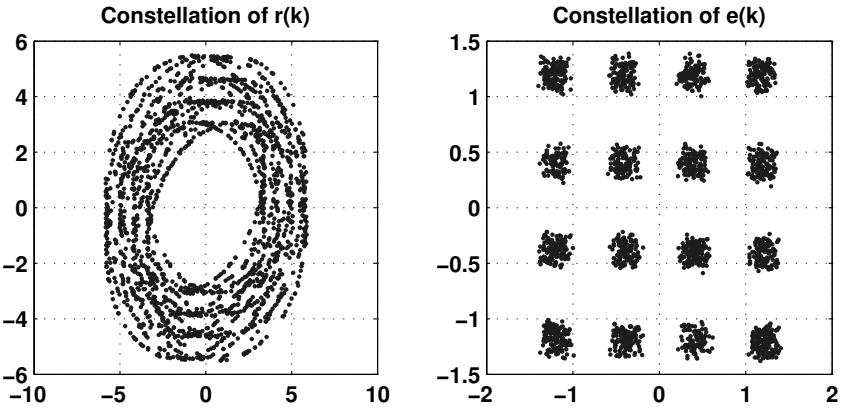

Figure 3.8: Constellation diagrams of $r(k)$ and $e(k)$. The baseband-equivalent desired signal has unit variance $\sigma_d = 1$ at the antenna. The remaining RF signal strengths are: 2nd = 0 dB, 3rd = 50 dB, 4th = 0 dB, 5th = 0 dB w.r.t the desired signal. The desired signal's modulation scheme is 16-QAM, the other signals are sinusoidal. The ADCs use 10 and 6 bits for $r(k)$ and $v(k)$ respectively.

3.7 Conclusions

We have presented a method to increase the harmonic rejection (HR) of an analog HR mixer by means of an adaptive compensation structure. The structure comprises two complex 1-tap FIR filters and a complex conjugation block. The filter weights are obtained by the LMS adaptive filter algorithm.

The proposed method is able to reject the strongest harmonic image. The final signal-to-interference ratio (SIR) at the output depends strongly on the static timing errors of the aggregate LO waveform and RF signals present at the antenna. Therefore, it is intractable to provide a performance figure valid for all cases. The effectiveness of our solution is shown by means of statistical simulation: a SIR increase of more than 36 dB is found in 90% of the cases. The mean SIR increase is 41.8 dB.

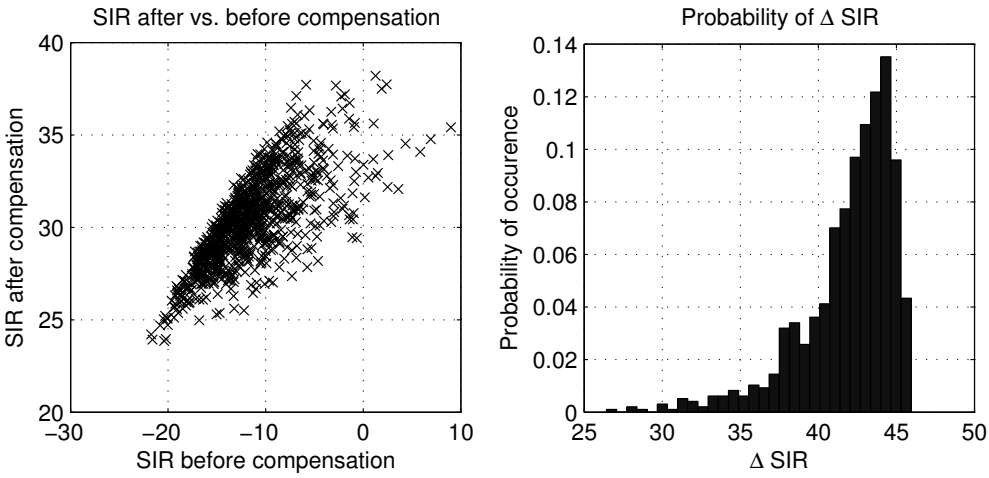

Figure 3.9: Left: a scatter plot of the SIR after vs. before compensation. Right: a histogram showing the probability of a certain SIR improvement caused by the compensator.

Chapter 4

Harmonic Image Cancelling: Experimental Verification

This chapter appeared in the proceedings of the EuWiT conference [43] and is a complete reproduction thereof.

4.1 Introduction

Harmonic downmixing is a problem in direct-conversion receivers employing switching mixers. Owing to the harmonic content of the effective local oscillator (LO) waveform, RF signals present at multiples of the LO frequency ω_{LO} appear at baseband together with the desired signal [38, 37]. These RF signals, or *harmonic images*, can be much stronger than the desired signal and can thus cause interference.

This is especially a challenging problem in multi-band receivers such as television tuners [36]. Traditionally, this is solved by removing the harmonic image signals before they reach the mixer stage through an RF tracking filtering. Such filters are power hungry and it is difficult to design them that they keep their desired shape over a wide range of frequencies.

A different approach to avoid harmonic downmixing is to minimize the harmonic content of the effective LO waveform. By putting multiple switching mixers in parallel and summing their weighted outputs, the effective *aggregate* LO waveform contains less harmonics than a pure square wave. This technique has been successfully used in transmitters [38] and receivers [24] to remove the 3^{rd} and 5^{th} harmonic images. The first uncanceled image is the 7^{th} harmonic image.

In theory, the multipath solution in [24] is able to reject the 3^{rd} and 5^{th} harmonic images completely, but around 30 to 40 dB attenuation has been reported in practice. This limitation is due to the amplitude and phase imbalance between the paths,

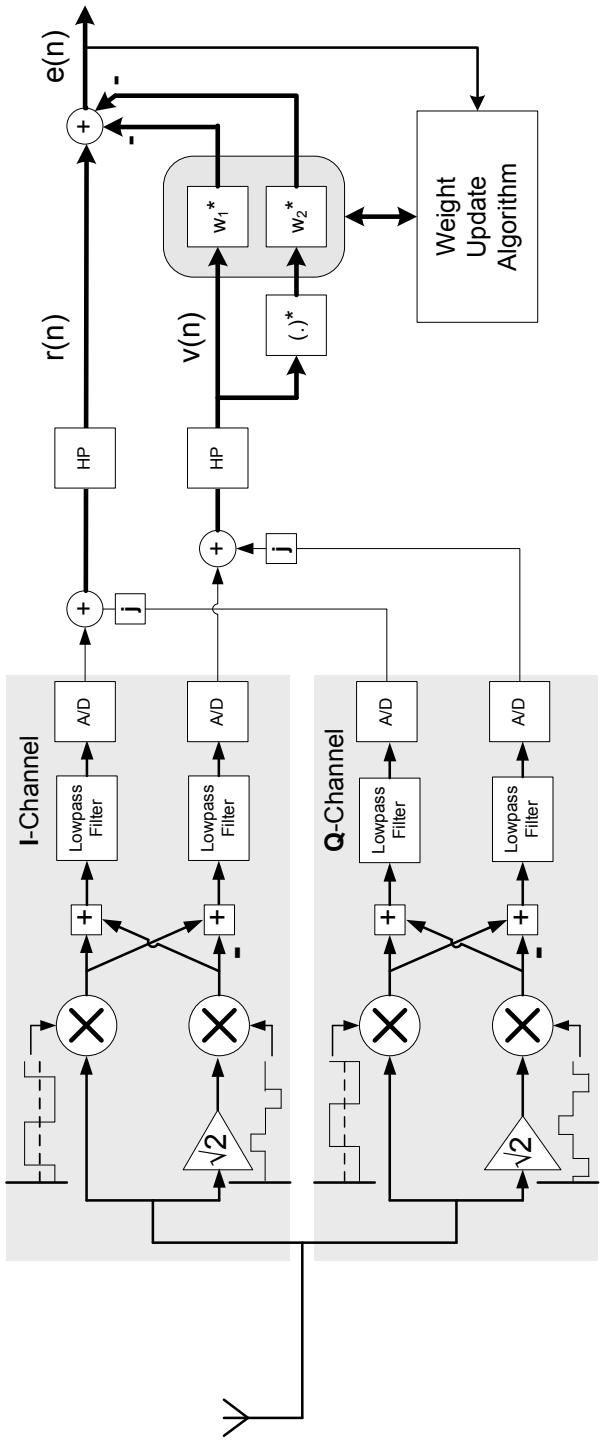

Figure 4.1: A two-stage harmonic rejection mixer.

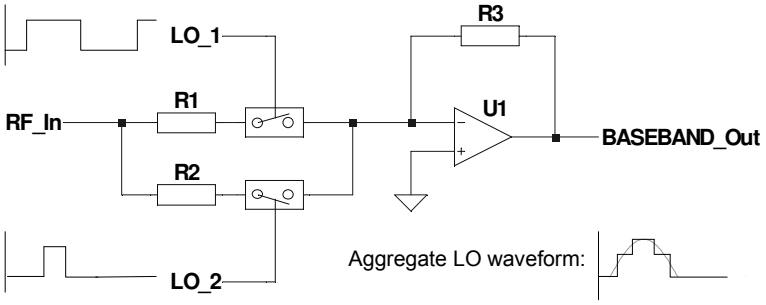

Figure 4.2: One half of a differential mixer circuit. The resistors R1 and R2 are used to provide the necessary $1 : \sqrt{2}$ *weighting ratio of the RF. Also shown is the resulting aggregate LO waveform.*

arising from mismatches in component values and timing errors in the multi-phase LO clock generator.

Some RF receivers, such as multi-band television tuners and upcoming cognitive radio receivers require more than 90 dB of harmonic rejection. Clearly, the 40 dB offered by the multi-path solution is not enough. In an attempt to solve this problem, we proposed a combined analog-digital technique based on interference canceling to further attenuate a strong harmonic image [35]. The previous work is based on simulations only. Here, we evaluate the properties by measurements on a breadboarded harmonic rejection downconverter circuit. The aim is to demonstrate functionality and to find practical performance limitations.

4.2 Overview of the Harmonic Rejection System

The harmonic rejection downconverter comprises an analog multi-path mixer built from off-the-shelf components, a four-channel A/D board and PC running the interference cancellation algorithm. The use of off-the-shelf components calls for a down-scaling of the frequencies. The aim is not to produce a circuit that is directly applicable, but to learn about the general circuit properties before designing a high-frequency chip. A system diagram of the downconverter is shown in Fig. 4.1.

The antenna signal is split into two paths, an I channel and a Q channel. Each channel consists of two 74HC4066-based switching mixers, each with a different LO waveform as indicated in Fig. 4.1. One half of the switching mixer is shown in Fig. 4.2. Note that the aggregate LO waveform, which is also shown in Fig. 4.2, approximates the first half-period of a sine wave. The $1 : \sqrt{2}$ weighting ratio is implemented by the resistors R1 and R2. The other half of the switching mixer (which is not shown) takes care of the second half-period of the sine wave.

The output of the mixers are added to form the signal r and subtracted to form the signal v. Both operations are done using CMOS opamps. The addition leads to the rejection of the 3$^{\text{rd}}$ and 5$^{\text{th}}$ harmonic images leaving the desired signal, while the subtraction leads to the rejection of the desired signal, leaving the aforementioned harmonic images. Amplitude and phase imbalances cause the rejection to be around 30 dB in case of the breadboarded system.

In other words, r contains the desired signal and some residual harmonic image signals, while v contains the harmonic image signals and some residual of the desired signal. In effect, v forms an estimate of the interference contained in r. This fact is exploited by the digital interference canceler.

The multi-phase LO clock generator consists of parallel-loadable 8-bit shift registers (74HC166). Each distinct LO waveform is made by one shift register of which the output is routed to its serial input. The parallel loading feature is used to load the desired switching pattern into the register at startup. The shift registers are clocked at 8 MHz making the base period of the eight-phase clock 1 MHz. Therefore, the downconverter is tuned to 1 MHz, the scaled LO frequency.

The signals are converted to the discrete-time domain by four 12-bit A/D converters (AD9342) running at 500 ksamples/s. Their data streams are read by a PC, which performs the digital signal processing. The 'added' I/Q and 'subtracted' I/Q signals are combined into two complex-valued signals, $r(n)$ and $v(n)$, from which two highpass filters (HP) remove any DC offsets and LF self-mixing noise.

4.2.1 The Interference Canceler

The interference cancellation (IC) algorithm, which is based on least mean squares (LMS) adaptive filter theory [25], consists of two complex weighting coefficients w_1 and w_2, as shown in Fig. 4.1. The coefficients scale and rotate $v(n)$ and its complex conjugate $v^*(n)$. The need for $v^*(n)$ in the canceler arises from I/Q imbalance in v and r. The reader is referred to [32] for a more thorough treatment on I/Q imbalance and its relation to this complex conjugate.

The IC is performed by the following equation:

$$e(n) = r(n) - w_1^*(n)\, v(n) - w_2^*(n)\, v^*(n) \tag{4.1}$$

,where $e(n)$ is the interference-reduced output.

The coefficients $w_1^*(n)$ and $w_2^*(n)$ approach the optimal (LMS) values as n goes to infinity, by applying the following multiple-input single-output (MISO) update algorithm [42]:

$$\begin{aligned} w_1(n+1) &= w_1(n) + \mu\, v(n)\, e^*(n) \\ w_2(n+1) &= w_2(n) + \mu\, v^*(n)\, e^*(n) \end{aligned} \tag{4.2}$$

,where $\mu = \frac{10^{-4}}{\sigma_v^2}$ is a learning coefficient and σ_v^2 denotes the power of the interference estimate $v(n)$. The value of μ is small enough that (4.2) is stable and large enough for rapid convergence. In [35], the algorithm is described in greater detail.

4.3 Measurements

To show that the HR concept works in practice, the spectrum of $r(n)$ and $e(n)$ were determined. A 1.01 MHz sinusoidal signal of 10 mV peak-peak was used as the desired signal and a 412 mV peak-peak 3.02 MHz sinusoid was used as a third harmonic image; a 32.3 dB power difference. The 412 mV swing was chosen so the nonlinearities of the CMOS switches were below -85 dBFS, where 0 dBFS corresponds to the full-scale of the ADC.

The spectrum of $r(n)$ and $e(n)$ are shown in Fig. 4.3. The plots were produced by performing a 256-point FFT on $r(n)$ and $e(n)$ after decimation-by-four to reduce the sampling rate to 125kHz. Decimation was needed to meet the real-time constraints of the PC.

The desired signal and 3^{rd} harmonic image appear at -34.8 dBFS (-10 kHz baseband) and -34.0 dbFS (20 kHz baseband) (respectively, in $r(n)$. The analog HR stage is able to reduce the 32.3 dB difference to 0.8 dB, indicating a harmonic rejection figure of 31.5 dB. At the output of the canceler, $e(n)$, the third harmonic image signal appears at -72.2 dBFS. Therefore, the canceler is able to increase the harmonic rejection by 37.4 dB to a total of 68.9 dB.

The spectrum of $e(n)$ shows that the third harmonic image, at $\pm$ 20 kHz, is not completely removed. The interference estimate $v(n)$ not only contains the interference, but also energy from the desired signal due to a finite amount of analog rejection, 28.50 dB in our case. Because of this, the attainable HR by the IC is also limited [34]; less desired signal energy (with respect to the interference energy) in $v(n)$ leads to greater HR of the harmonic image in $e(n)$. Therefore, the analog signal paths used to generate $v(n)$ should be designed to maximize the rejection of the desired signal.

To examine the dependence of the digital rejection on the signal-to-interference (SIR) ratio in $v(n)$, the third harmonic image signal was varied between 800 mVpp and 10 mVpp. The desired signal was kept at 10 mVpp. The same test was repeated for a 5^{th} harmonic image signal at 5.02 MHz. As the SIR of $v(n)$ is related to the SIR of $r(n)$, we need only focus on $r(n)$.

The SIR of $e(n)$ against the SIR of $r(n)$ is shown in Fig. 4.4. As the SIR of $r(n)$ decreases, owing to a power increase in the third harmonic image, more harmonic image signal energy is present in $v(n)$ while the desired signal's energy remains the same. As the SIR of $r(n)$ decreases, an increase in rejection is expected in $e(n)$ [35]. This remarkable trend is clearly visible in Fig. 4.4 for both the 3^{rd} and 5^{th} harmonic images. However, when the SIR of $r(n)$ is more than about 23 dB, the canceler makes the SIR of $e(n)$ worse. This feature can be avoided by bypassing the canceler when there is no improvement. Detecting this situation requires additional knowledge, such as the bit-error rate. This is a topic for further research.

When the SIR of $r(n)$ is smaller than 0 dB, a droop in the SIR of $e(n)$ is visible. This coincides with an interferer voltage of 412 mVpp or higher, a region where the CMOS switches in the mixer circuit become nonlinear. As a result, the I/Q imbalance

in $v(n)$ increases and more desired signal energy is found in $v(n)$. As discussed above, this has a detrimental effect on the harmonic rejection, hence the lower SIR of $e(n)$.

The total harmonic rejection was determined to show the system's performance, see Figure 4.5. As expected, the harmonic rejection increases with increased harmonic image power, a favorable trend indeed! The harmonic rejection reaches its maximum when the downconverter is in its nonlinear region, indicating resilience to intermodulation products. The maximum harmonic rejection attained by the downconverter is 75.4 dB, its minimum is 13.8 dB. The analog stage offers around 32 dB of rejection, irrespective of the harmonic image power. Switching off the canceler, as suggested above, makes the attainable harmonic rejection range from 32 to 75 dB. Note that the aforementioned range is without an RF filter.

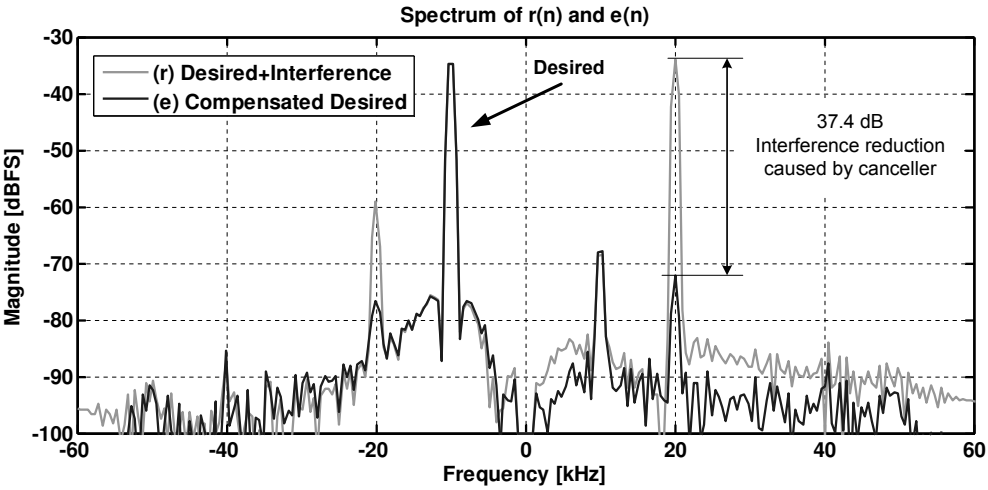

Figure 4.3: Magnitude spectrum of $r(n)$ and $e(n)$. The desired signal (1.01 MHz RF, -10 kHz baseband) is 10 mVpp at the antenna, the third harmonic image signal (3.01 MHz RF, 20 kHz baseband) is 412mVpp at the antenna. Both signals are sinusoidal. Decimate-by-four and a 256-point FFT were used to obtain the spectrum.

4.4 Effect of Circuit Imperfections

Other factors besides the desired signal energy in $v(n)$ determine the signal components at the output of the digital canceler. To effects will be considered next; nonlinearities in the mixer frontend, jitter of the LO or A/D sample clock and DC offset & LO leakage.

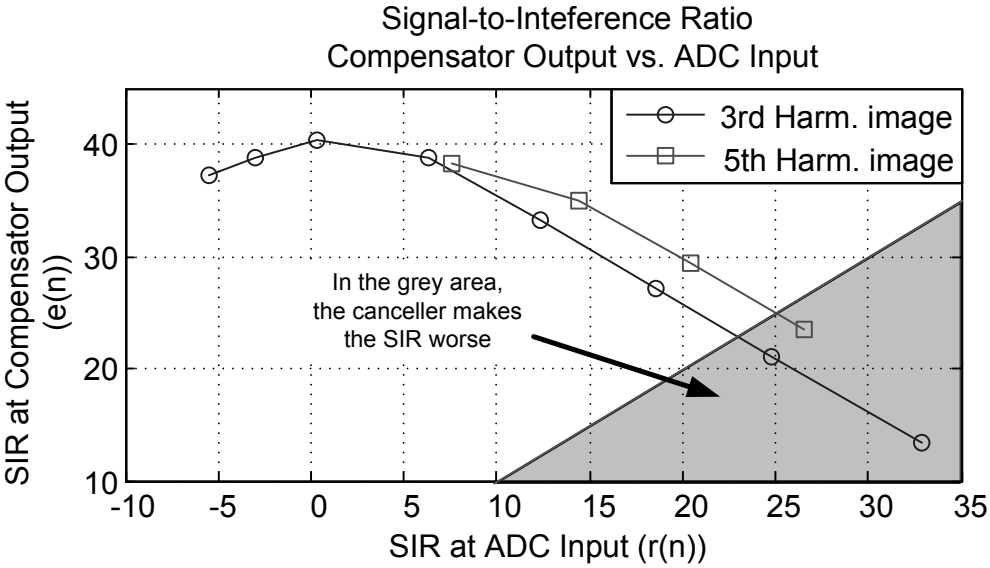

Figure 4.4: Signal-to-interference ratio (SIR) of $e(n)$ versus the SIR at the mixer output $r(n)$. The desired signal is 10 mVpp at the antenna, the harmonic image signals are between 10 and 800 mVpp at the antenna. Both signals are sinusoidal.

4.4.1 Nonlinearities

When the the frontend is in a blocking condition, i.e. the signals are being clipped or heavily distorted, there is no way to recover the desired signal. However, given mildly nonlinear conditions, intermodulation products that are generated before the mixer, for instance, in an low-noise amplifier, will be rejected when they exist in the same band as the interferer being canceled; thus either in the 3^{rd} or the 5^{th} harmonic image band.

Intermodulation products generated after the mixers are generally not canceled as they are not common among the paths. Luckily, this seperation also ensures that correlation between $r(n)$ and $v(n)$ cannot be attributed to these products. As the values of w_1 and w_2 depend on the correlation between $r(n)$ and $v(n)$, low-level intermodulation products do not affect the performance of the canceler. Note that these products are not canceled and can cause interference to the desired signal.

4.4.2 Jitter of the master clock and A/D sample clock

Jitter of the clock driving the multi-phase LO generator, the master clock, is common to all the shift registers. When we ignore the timing jitter caused by the shift registers

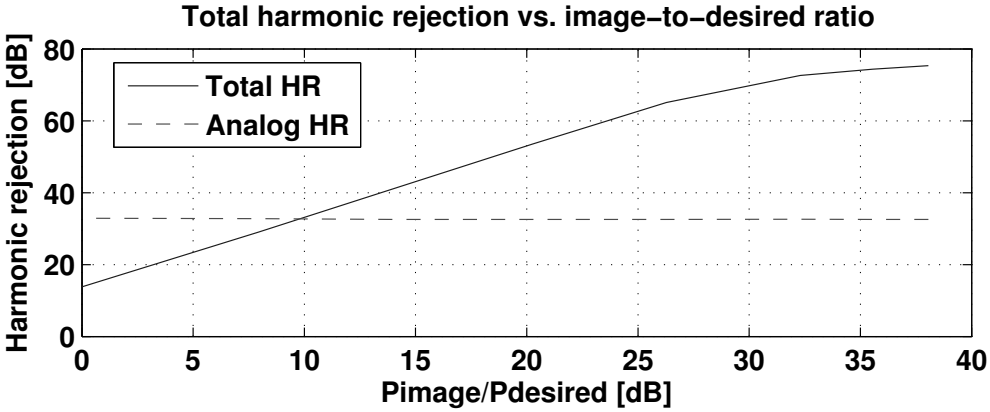

Figure 4.5: Total harmonic rejection ratio (analog+digital) against the image-to-desired signal ratio.

themselves, the transitions at the output of the registers share the same timing error. As the mixer clocking patterns are not all equal, this means that high-frequency jitter, i.e. edge-to-edge jitter, is not the same for each mixer, which leads to a decorrelation between $r(n)$ and $v(n)$ caused by phase modulation. The canceler is only able to remove the part common to $r(n)$ and $v(n)$, i.e. the correlating part, leaving the decorrelated residue and thereby reducing the harmonic rejection.

When the first measurements were taken, a function generator was used as the master clock. Its phase noise caused considerable skirting around the desired and harmonic carriers. When the function generator was replaced by a fixed-frequency crystal oscillator, the skirts disappeared but the HR performance remained the same. This points to a certain resilience with respect to phase noise.

Timing jitter of the A/D clock is not a problem for the canceler as the A/D converters share the clock and thus have the same timing error. As a result, there will be no decorrelating effect. However, as is to be expected, A/D clock jitter can cause problems in the carrier or symbol synchronization and decoding parts of the receiver.

4.4.3 DC offset and LO leakage

Both DC offset and LO leakage are well-known problems of direct-conversion receivers [44].

A DC offset at the input of the IC algorithm will cause a run-away effect of the filter coefficients, in this case w_1 and w_2. The reason for this is the accumulation that takes place in the coefficient update algorithm (4.2), in the presence of a DC term.

A source of slowly time-varying DC offset in direct-conversion receivers is the LO leakage phenomenon. Energy radiates from the local oscillator and finds its way into the antenna or mixer, thereby mixing with itself to DC.

An easy solution to the DC offset problem is to include digital high-pass filters directly after the A/D converters. However, not all modulation schemes are compatible with a notch at DC. For example, GMSK used in GSM cellphones, has most of its signal energy near DC when the receiver is operated in zero-IF mode.

4.5 Conclusions

We presented measurements done on a two-stage harmonic rejection downconverter built from off-the-shelf components. The downconverter comprises a multi-path analog mixer, with approximately 32 dB of harmonic rejection, as a first stage and a digital harmonic rejection system based on adaptive blind interference canceling as a second stage.

The inclusion of the digital harmonic rejection stage does not pose any special requirements on the analog circuit other than two additional A/D converters and subtracters. The performance of the harmonic rejection algorithm depends mainly on the quality of the interference estimate $v(n)$. Therefore, careful design of the signal paths used to obtain $v(n)$ with respect to rejection of the desired signal, is advantageous. Frontend nonlinearities do not severely affect the performance of the digital canceler, but intermodulation products are generally not canceled unless they are generated before the downconverter. The canceler shows some resilitience to LO phase noise but is not capable of handling DC offsets at its inputs. Digital highpass filters are needed to remove these offsets. The harmonic rejection of the downconverter ranges from 32 to 75 dB, depending on the power of the harmonic image. A stronger harmonic image leads to more harmonic rejection; a very favorable trend indeed.

Chapter 5

An SDR front-end featuring Dual-Domain Harmonic Rejection.

5.1 Prologue

This chapter appeared in the IEEE Journal of Solid State Circuits [45] and is a complete reproduction thereof with the exception of corrections made to the angle data in Table 5.1. The corrections do not affect the text of article.

As a result of the reproduction, this chapter contains work done by Dr. Z. Ru, who designed and implemented the analog CMOS circuitry. Therefore, the analog circuitry, especially the polyphase two-stage harmonic rejection technique, should not be considered a part of this thesis.

The Fourier coefficients for the LO pulse wave mentioned in this chapter can be found in Appendix A.4.

5.2 Introduction

Software-Defined Radio (SDR) concepts have recently drawn considerable academic interest and increasingly also industrial interest. Limiting our discussion to RF transceivers, most work focuses on integrating the functionality of multiple dedicated narrowband radios into one radio, which is reconfigurable by software [46, 47]. This is hoped to bring cost and size reductions while supporting an ever increasing set of communication standards in a single device. The SDR concepts might also allow field upgradable radios to accommodate evolving standards and become an enabler for

cognitive radio applications, to improve the efficiency of utilizing the scarce spectrum resources.

To support the reception of different radio standards, a wideband radio receiver seems an obvious solution. Some wideband receivers have been reported, e.g., for wideband TV receivers [13, 48], ultra-wideband receivers [49, 50], and SDR applications [46, 47]. However, *wideband receivers are not only wideband to desired signals but also wideband to undesired interference.*

Traditional wireless standards use dedicated radio bands, so that in-band interference (IBI) can be distinguished from out-of-band interference (OBI). For a SDR aiming at covering arbitrary frequencies, the definition of IBI and OBI may become fuzzy. Still, we will use the terms IBI and OBI in this paper as: 1) current SDR receivers often aim at covering multiple traditional radio standards which have clear band definitions; 2) even if this is not the case, e.g. for cognitive radio, a SDR still aims at implementing selectivity, i.e. receive a signal for which baseband bandwidth is much smaller than f_{RF}. In the latter case OBI can be interpreted as "out-of-baseband interference".

For popular mobile communication applications, the IBI can be as strong as -30 to -20 dBm while the OBI can be as strong as -10 to 0 dBm [51]. An RF band-selection filter is often employed to suppress OBI to below the IBI level, requiring high quality factor and sharp roll-off. These filters are difficult to integrate on-chip and are often dedicated to one specific band. In a SDR receiver, the dedicated RF filter is undesired owing to its poor flexibility. State-of-the-art multi-band receivers [52, 53] use multiple dedicated RF filters in parallel, which increases size and cost for every band that is added. This paper aims at improving the robustness of a radio receiver to OBI in order to relax the requirement on RF filters, exploiting fully-integrated analog and digitally-enhanced mixed-signal techniques.

At least two mechanisms generate in-band distortion due to OBI: 1) nonlinearity related mixing of strong OBI via, e.g., intermodulation or cross-modulation; 2) harmonic mixing of interferers with LO harmonics due to hard-switching mixers and/or the use of digital LO waveforms. We will explain these two mechanisms briefly below as well as review the state-of-the-art solutions for these problems.

Out-of-band nonlinearity

Nonlinearity may generate intermodulation and harmonic distortion falling on top of the desired signal, or may desensitize a receiver due to blockers and produce cross modulation [10]. Without sufficient RF band-selection filtering, the out-of-band linearity can become the bottleneck since OBI is much stronger than IBI. A wideband LNA as used in [46] and [47] amplifies the desired signal and undesired wideband interference with equal gain. A low voltage gain of 6 dB can already clip a 0 dBm blocker to a 1.2V supply. The amplified interference also challenges the nonlinear output impedance of an LNA and the linearity of a next-stage mixer.

LNA linearization techniques have been proposed [54, 55] to achieve an IIP3 in excess of +15 dBm but have drawbacks [56]: 1) they often rely on two nonlinearity mechanisms that compensate each other but don't automatically match, so that some kind of fine tuning is needed, compromising robustness to process spread; 2) they mostly rely on modeling of the weakly nonlinear region so that high IIP3 is only achieved for low input two-tone power while limited or no benefit for strong interference.

Recently, a blocker filtering technique has been presented [57], achieved by means of an auxiliary feedforward path, which conducts the undesired interferers and suppresses them by subtracting them from the main signal path at the output of LNA. However it comes with some drawbacks: 1) significant cost arises in terms of noise and power consumption in that auxiliary path; 2) the blocker filtering effect relies on the matching between the main path and the auxiliary path. We will see later in Section 5.3 that equivalent functionality can be achieved with much simpler hardware, i.e. without requiring additional signal path.

Harmonic mixing

Linear time-variant behavior in a hard-switching mixer, or equivalently multiplication with a square wave, not only downconverts the desired signal but also interference around LO harmonics. This harmonic mixing is of much less concern in narrowband receivers, relying on RF band-selection filters. The 8-phase harmonic-rejection (HR) mixers as described in [11] can suppress RF signals around second to sixth LO harmonics but amplitude and phase mismatches limit the achievable HR ratio typically to 30-40 dB [47, 13, 48, 58]. However, a quick calculation shows that much more rejection is needed: if we want to bring harmonic responses down to the noise floor, e.g. -100 dBm in 10 MHz for NF=4dB, and cope with interferers of -40 to 0 dBm, a HR ratio of 60 to 100 dB is needed. State-of-the-art wideband TV tuners rely on RF tracking filters together with HR mixers [13, 48] to guarantee more than 65 dB HR ratio. We aim at removing such tracking filters or at least relaxing their requirements by making HR mixers more robust to mismatch.

Contribution of this paper

Both out-of-band nonlinearity and harmonic mixing can severely degrade signal-to-distortion ratio[1] . Therefore, in our view *a practical SDR should not just be a wideband receiver, but also have enhanced out-of-band linearity and enhanced harmonic rejection.* This paper will propose an architecture to improve the wideband receiver's linearity, especially its IIP3 for OBI and its tolerance to blockers. Moreover, to dramatically improve HR performance, two alternative HR techniques are proposed: 1) a two-stage polyphase HR technique implemented purely in the analog domain [14, 15];

[1]Signal-to-Distortion Ratio is so important to software-defined radio that it can be viewed as another interpretation of "SDR".

2) a mixed-signal technique exploiting digital adaptive interference cancelling (AIC) [59]. Both improve HR by rejecting harmonics in two successive steps ("iterative"), and both share the same 8-phase RF-to-baseband downconverter as a first HR stage. Compared to [14, 15, 59], we greatly extend the analysis and show additional experimental results. Compared to [60], this work derives the interference estimate in another way, presents measurements and achieves better performance due to the better interference estimate.

The rest of the paper is organized as follows. Section 5.3 introduces a technique using low-pass filtering to mitigate blockers and improve out-of-band IIP3. Section 5.4 proposes a two-stage polyphase HR concept to improve amplitude accuracy obtaining high HR robust to mismatch. To improve both amplitude and phase accuracy, a digitally-enhanced HR technique using AIC is presented in Section 5.5. The implementations of the analog front-end and the digital back-end are discussed in Section 5.6 and 5.7 respectively. The experimental results are presented in Section 5.8 with a comparison of analog and digital HR techniques as well as benchmarking to other work. The conclusions are drawn in Section 5.9.

5.3 Low-Pass Blocker Filtering

Traditionally, narrowband receiver front-ends use LNA-mixer combinations which can deliver good enough linearity, typically an IIP3<0 dBm, for in-band (IB) interference while an RF band-selection filter takes care of out-of-band (OB) interference. However, in a wideband receiver, since OBI is much stronger than IBI, the required OB IIP3 is much higher than the required IB IIP3 and even desensitization can occur due to strong OB blockers. Therefore, frequency selective amplification or attenuation is desired. Tunable band-pass filtering (BPF) is in principle a solution, but it is difficult to provide sufficient selectivity and tunability simultaneously with good noise and linearity, using CMOS on-chip filters. Here we approach the problem from another angle.

Concept

To guarantee low NF, we need amplification early in the receiver chain. Voltage amplification in an LNA is usually realized via V-I conversion using, e.g. the transconductance of a transistor, followed by I-V conversion via some impedance or transimpedance. We can separate the two functional blocks, V-I and I-V, and insert a passive zero-IF mixer and a low-pass filter (LPF) in between, as shown in Fig. 5.1. The LPF drawn is conceptually current-in current-out and internally with no voltage swing. However in practice, the functions of the LPF and the I-V conversion can be merged by using a frequency-dependent impedance, such as a parallel R and C.

It is crucial to present a low impedance over a wide band to the output of V-I block, i.e. node B, so that little voltage gain occurs before filtering, leading to less distortion

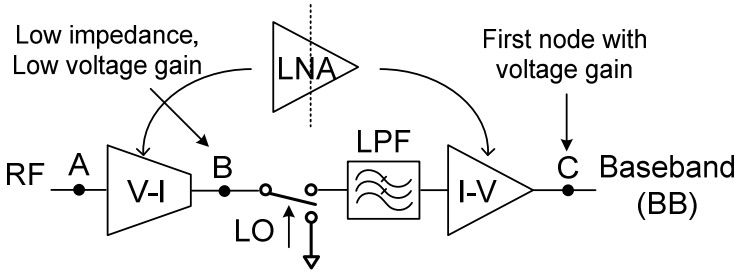

Figure 5.1: Conceptual diagram of the low-pass blocker filtering.

in the mixer and the nonlinear output impedance of the V-I block[2]. Therefore the first voltage gain occurs only at baseband after low pass filtering, which provides selectivity to mitigate OBI.

To quantify the blocker filtering effect, we may compare the 1 dB compression point (P_{1dB}) for desired signals to the 1 dB desensitization point (B_{1dB}) for blockers[3] , both input referred. Assume a third-order Taylor series for nonlinearity with α_1 and α_3 for the first and third order coefficients respectively. Without any blocker filtering, it can be derived from [61] that $P_{1dB} = 10 \cdot \log\left(0.145 \cdot \left|\frac{\alpha_1}{\alpha_3}\right|\right)$ and $B_{1dB} = 10 \cdot \log\left(0.0725 \cdot \left|\frac{\alpha_1}{\alpha_3}\right|\right)$, if both in amplitude. Therefore, B_{1dB} can be calculated based on P_{1dB}, and if without blocker filtering, B_{1dB}=(P_{1dB}-3dB).

The LPF in Fig. 5.1 can mitigate blockers, and its bandwidth (BW) and order (n) determines the blocker filtering effect. If desensitization happens after I-to-V conversion, which is often the case due to a high voltage gain and limited voltage headroom, the suppression of blockers in dB by the LPF corresponds to the improvement of B_{1dB}.

However, for a wideband receiver the situation is more complicated, as one RF-blocker can be downconverted by different LO harmonics. For instance, a square-wave LO of 400 MHz converts a 1250 MHz RF signal to 850 MHz and 50 MHz via the first and third harmonic of the LO, respectively. The strongest downconverted signal depends on the blocker frequency (f_B) and the LO frequency (f_{LO}), i.e. which LO harmonic the blocker is closer to. Also it depends on the relative gain of the m^th harmonic compared to the fundamental (first) harmonic, i.e. the m^th harmonic rejection ratio (HR_m).

[2]Another motivation for low impedance at RF nodes is to widen the receiver's RF bandwidth as exploited in [49]

[3]P_{1dB} thus defines the desired input signal power at which the receiver gain drops by 1 dB without applying blockers, while B_{1dB} defines the undesired input interference (single-tone blocker) power where the receiver gain drops by 1 dB.

Assume for simplicity that one blocker component dominates after downconversion and determines B_{1dB}. If $|f_B - mf_{LO}| \leq BW$, i.e. the blocker is within the LPF BW after downconversion by the m$^t h$ harmonic, we find:

$$B_{1dB} \approx (P_{1dB} - 3\ dB) + \min[HR_m], \tag{5.1}$$

if $|f_B - mf_{LO}| > BW$, i.e. the blocker is outside the LPF BW after downconversion by the m$^t h$ harmonic, assuming an asymptotic filter characteristic, we find:

$$B_{1dB} \approx (P_{1dB} - 3\ dB) + \ldots \\ \min\left[n \cdot 20 \cdot \log_{10}\left(\frac{|f_B - m \cdot f_{LO}|}{BW}\right) + HR_m\right]. \tag{5.2}$$

From (5.2) we can expect smaller bandwidth (BW) and higher order (n) of the LPF gives higher B_{1dB}, if f_B, f_{LO} and HR_m are fixed. Besides, we can also improve B_{1dB} via improving P_{1dB}, e.g. if compression happens at the receiver output, a lower receiver voltage gain or a larger output voltage headroom can improve the input referred P_{1dB}, and hence a higher B_{1dB}.

The LPF can help to relax the OB linearity of the I-V conversion, however *not* for the V-I conversion. Therefore, the maximum achievable B_{1dB} is ultimately limited by the P_{1dB} of the V-I conversion minus 3 dB. Thus linearity of the V-I conversion is very important and we will return to that point in Section 5.6. Via a similar mechanism, the OB IIP3 can also be enhanced compared to the IB IIP3.

Realization

A specific realization of the general concept (Fig. 5.1) is presented in Fig. 5.2. Zero-IF receivers commonly use an LNA followed by a mixer with current output loaded by a LPF to suppress interference. We carry this approach *one step further* by entirely removing the voltage-gain LNA before the mixer and instead use a Low Noise Transconductance Amplifier (LNTA) as the first RF stage for the V-I conversion with input impedance matching. As mentioned before, maintaining a low impedance at node B over a wide band is important. This can be realized by using low-ohmic switches in the passive mixers followed by transimpedance amplifiers (TIA) built via negative feedback around operational transconductance amplifier (OTA). The feedback network consists of R & C in parallel to form a LPF. At high frequency, the feedback-loop gain drops so the virtual-ground impedance rises. By putting a capacitor C_{VG} to ground or across the differential virtual-ground nodes, the impedance at high frequency is reduced. Both C_{VG} and C_{FB} contribute to the total LPF function.

Fig. 5.2 also shows, qualitatively, the impedance relationship between node B (Z_B) and node D (Z_D), i.e. Z_B is roughly equal to scaled Z_D plus the mixer switch-on resistance (R_{mixer}) and shifted in frequency. Applying an RF current input, it can be

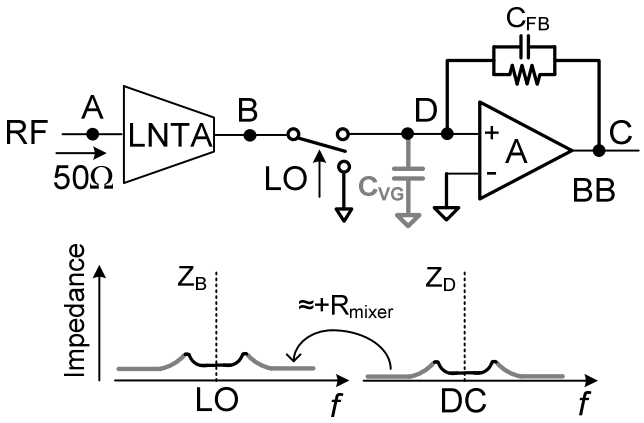

Figure 5.2: Realization of the low-pass blocker filtering and illustration of impedance transfer effect.

derived [21] that, for an N-phase mixer driven by 1/N-duty-cycle (non-overlapping) LO, the impedance Z_B at an RF around m$^t h$-LO-harmonic frequency (m=1, 2, 3...), i.e. with an offset frequency Δf from $m \cdot f_{LO}(|\Delta f| \leq f_{LO}/2)$, can be written as:

$$Z_B(m \cdot f_{LO} + \Delta f) \approx R_{mixer} + \frac{N}{m^2 + \pi^2} \sin^2\left(\frac{m \cdot \pi}{N}\right) \cdot Z_D(\Delta f). \tag{5.3}$$

Please note that (5.3) holds given that Z_D presents strong filtering effect, e.g. a pole at a much lower frequency than f_{LO}, which is normally the case for a down-mixer. Consider m=1: for N=2 or 4 the coefficient of Z_D is about 0.2, and for N=8, it is about 0.12, showing R_{mixer} actually plays a much larger role in determining Z_B. For $m > 1$, the coefficient of Z_D is even smaller.

Besides delivering low impedance, this topology (Fig. 5.2) can also bring two other advantages exploited in some *narrowband* receivers [62, 63, 64]: 1) good *in-band* linearity in the I-V conversion due to the negative feedback; 2) low 1/f noise from the mixer switches working in the linear region which carry little DC current. To the authors' knowledge, this work [14] is the first to exploit this topology in a *wideband* receiver to enhance *out-of-band* linearity. If the LPF suppresses the OBI well, the main contributor to the OB nonlinearity will come from the V-I conversion of the LNTA, which can be quite linear as we will see later.

Although voltage amplification is avoided at RF, if the transconductance of LNTA is big, the receiver-input referred noise of the following stages, i.e. mixer and TIA, can be relatively small, so that the overall receiver NF can still be good and dominated by LNTA itself. As an example, the whole receiver in [64] achieves a NF of 2.2 dB based on a similar topology but in a narrowband configuration.

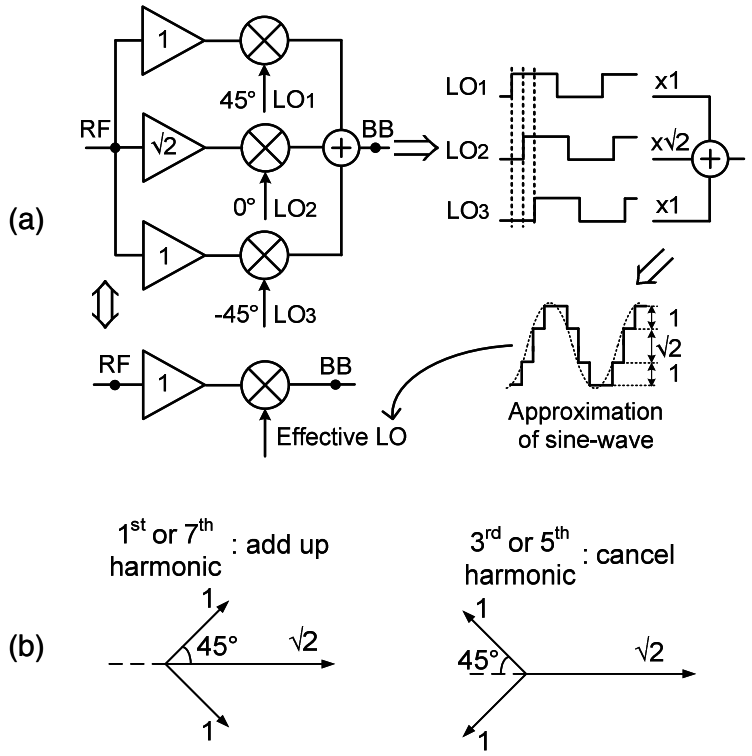

Figure 5.3: (a) Block diagram of a traditional HR mixer, and (b) its vector diagram.

5.4 Two-Stage Polyphase Harmonic Rejection

The low-pass blocker filtering technique presented in the previous section acts after mixing, so it cannot prevent the harmonic mixing already occurring in the mixer stage. It is known that using balanced LO can suppress all even-order harmonics. To also suppress odd-order harmonics, harmonic-rejection (HR) mixers using multi-phase square-wave LOs driving parallel operating mixers have been proposed before [11, 58]. Fig. 5.3 (a) shows an example, where the weighted current outputs add up to approximate mixing with a sine-wave LO. The combination of an amplitude ratio of $1 : \sqrt{2} : 1$ and an eight-phase LO (equidistant 45°) can reject the third and fifth harmonics, as shown in the vector diagram of Fig. 5.3 (b). The seventh harmonic is not rejected and still needs to be removed by filtering, but the filter requirement is strongly relaxed compared to the case of a normal double-balanced I/Q mixer whose first unrejected harmonic is the third order. However, the achievable HR ratio is

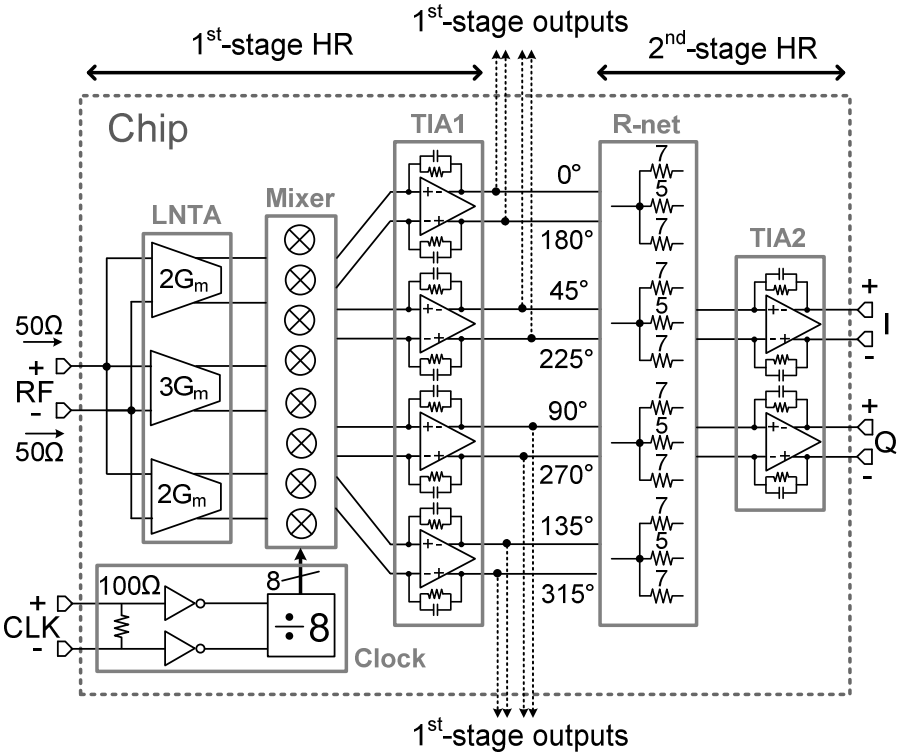

Figure 5.4: Chip block diagram implementing the two-stage polyphase HR and the low-pass blocker filtering

limited by the accuracy of the amplitude ratios and the LO phases.

To achieve high HR ratio we need to accurately implement the desired weighting ratios, in this case the irrational ratio $1 : \sqrt{2}$ accurately on chip. There are at least two challenges here: 1) realizing the right nominal (average) ratio; 2) keeping random variations due to mismatch small enough. To address these issues we propose a two-stage polyphase HR concept (see Fig. 5.4) in which two-stage *iterative* weighting and summing results in much higher HR than traditional HR mixers with only 1-stage. We will show that this iterative weighting results in a small product of relative errors for random variations, whereas the use of suitably chosen integer ratios results in sufficient accuracy to achieve a HR well above 60 dB.

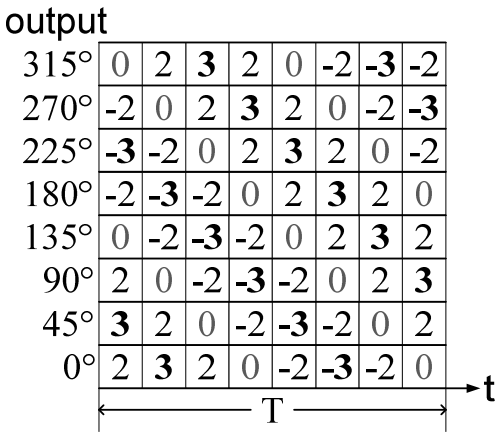

Figure 5.5: Weighting factors for the first-stage HR outputs versus time.

Block diagram

Figure 5.4 shows the block diagram of the two-stage polyphase HR system, implemented on chip. The irrational ratio $1 : \sqrt{2} : 1$ is realized in two iterative steps with integer ratios: a first step with $2 : 3 : 2$ and a second step with $5 : 7 : 5$. The first-stage weighting is realized via 7 unit-LNTAs interconnected in 3 parallel groups to form the $2 : 3 : 2$ ratio. The second-stage weighting is realized via a baseband resistor network "R-net" between the TIA1 and TIA2 stages. The $5 : 7 : 5$ amplitude ratio corresponds to the $7 : 5 : 7$ resistance ratio. The passive mixer array is driven by eight-phase 1/8-duty-cycle (non-overlapping) LO. Via the combination of the LNTA, mixer and TIA with LPF, the first voltage gain occurs at baseband after LPF for good OB linearity. Since harmonics can be as strong as blockers, it is important to have significant HR before the first voltage gain, especially because the anti-blocker filtering doesn't reduce harmonic images close to harmonics of the LO, as shown in (5.1). The additional more accurate HR follows in the second stage, aiming to bring residual harmonic images below the noise floor.

Working principle

We will now show how we accurately approximate $1 : \sqrt{2} : 1$ via $2 : 3 : 2$ and $5 : 7 : 5$. A key point is that the output of the TIA1 stage has eight IF-outputs with equidistant phases, i.e. 0 to 315 with 45-degree increments, instead of the conventional four phases, i.e. quadrature. This enables iterative HR by adding a second stage. Fig. 5.5 shows the weighting factor for the 8 outputs of the first-stage HR versus time (t) for one complete period of the LO (T). If we weight and sum three adjacent-phase

$$
\begin{array}{rcccccccc}
[\,2 & \mathbf{3} & 2 & 0 & -2 & \mathbf{-3} & -2 & 0\,]\cdot 5 \\
+[\,0 & 2 & \mathbf{3} & 2 & 0 & -2 & \mathbf{-3} & -2\,]\cdot 7 \\
+[\,\text{-}2 & 0 & 2 & \mathbf{3} & 2 & 0 & -2 & \mathbf{-3}\,]\cdot 5 \\
\hline
[\,0 & 29 & 41 & 29 & 0 & -29 & -41 & -29\,]
\end{array}
$$

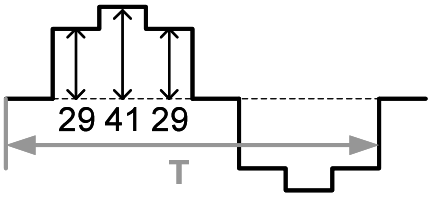

Figure 5.6: Approximation of $1 : \sqrt{2} : 1$ *as* $29 : 41 : 29$ *via integer ratios.*

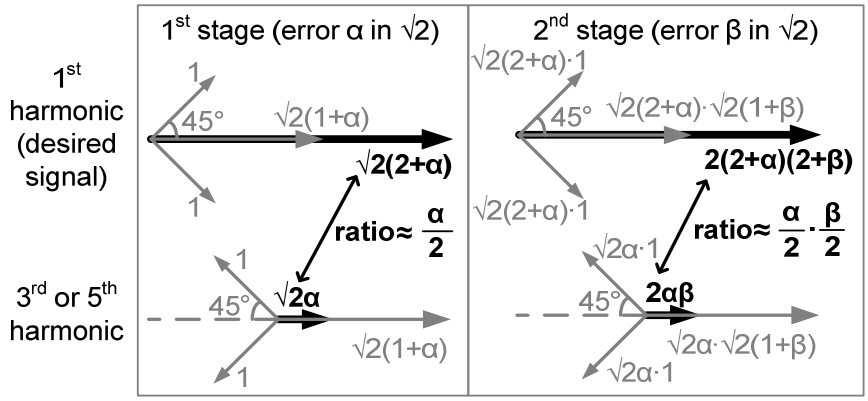

Figure 5.7: Error reduction principle in the two-stage polyphase HR (error $\alpha/2$ *becomes a much smaller product of errors:* $\alpha\beta/4$.

outputs of the first-stage HR via the second-stage weighting factors 5:7:5, as shown in Fig. 5.6, we find $29 : 41 : 29$. The ratio $41 : 29$ is equal to 1.4138, which represents only a 0.028% error from $\sqrt{(}2)$. This amplitude error corresponds to a HR ratio of more than 77 dB, if no phase error.

The two-stage polyphase HR not only can approximate $1 : \sqrt{2} : 1$ very closely, but it is also robust to amplitude mismatch, as illustrated in Fig. 5.7 via vector diagrams of the two stages. It shows how, for the desired signal, polyphase contributions from

three paths add up, while for the third and fifth harmonics, they cancel nominally. Assume now that the error in realizing $\sqrt{2}$ dominates and model it as a relative error α for the first stage and β for the second stage. Also for simplicity, assume that the desired signal and the third and fifth harmonics are equally strong at the receiver input and neglect the relative strength of different LO harmonics due to a certain LO duty cycle. After the first stage, the desired signal is multiplied by $\sqrt{2} \cdot (2 + \alpha)$ and the third and fifth harmonics by $\sqrt{2} \cdot \alpha$, leading to a relative error (interference-to-signal ratio) of $\alpha/2$ if $\alpha \ll 2$. For the second stage the same derivation holds. As the two stages are cascaded, the product of the gains determines the result, i.e. the total gain for the desired signal becomes $[\sqrt{2} \cdot (2 + \alpha)] \cdot [\sqrt{2} \cdot (2 + \beta)]$ and for the third and fifth harmonics it is $[\sqrt{2} \cdot \alpha] \cdot [\sqrt{2} \cdot \beta]$. This renders a total relative error (interference-to-signal ratio) of:

$$\frac{2 \cdot \alpha \cdot \beta}{2 \cdot (2 + \alpha) \cdot (2 + \beta)} \approx \frac{\alpha}{2} \cdot \frac{\beta}{2}, \tag{5.4}$$

if $\alpha \ll 2$ and $\beta \ll 2$. Therefore, the total relative error is the *product* of the relative errors for the two stages, $\alpha/2$ and $\beta/2$. If the second stage has an error β=1%, ideally this improves HR by $(\beta/2)^{-1}$, i.e. 46 dB, which has also been confirmed by simulation.

Please note that the product of errors, as shown in (5.4), holds for both third and fifth harmonics. Moreover, it not just works for mismatch induced errors but for any amplitude errors, e.g. errors introduced by parasitic capacitance or finite LNTA output impedance.

Theoretically, more than two stages can achieve even better amplitude accuracy, but practically phase accuracy will often dominate. To also address the phase error, next we will propose an alternative HR concept that exploits digital techniques.

5.5 Digitally-Enhanced Harmonic Rejection

Even for the concept proposed in the previous section, the HR performance can still be limited by the amplitude and especially phase mismatches between the paths. In this section, we propose a digitally-enhanced HR architecture exploiting digital adaptive interference cancelling (AIC). Simply put, this concept adapts an estimate of the third or fifth-order harmonic image in such a way that after subtraction from the received signal the HR ratio is increased.

The AIC concept is shown in Fig. 5.8: the interference estimate, $v(n)$, is aligned (in phase and amplitude) with the interference in the received signal, $r(n)$, by an adaptive digital equalizer. Thus, the equalizer removes the *amplitude and phase differences* of the interference between $v(n)$ and $r(n)$. The equalized interference estimate is subtracted from the received signal, which cancels the interference and produces the output signal, $e(n)$.

Fig. 5.9 shows a system-level block diagram of the proposed system. The analog front-end used is identical to the first stage of the two-stage analog HR architecture

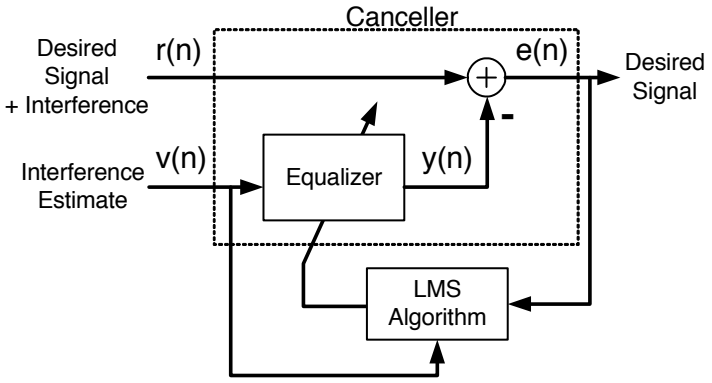

Figure 5.8: A block diagram shwoing the concept of adaptive interference cancelling.

proposed earlier. It produces four fully-differential signals, which are converted into the digital domain using four A/D converters, to form signals x_0, x_{45}, x_{90} and x_{135}. The HR of the analog down-mixer, typically in the range of 30 to 40 dB, reduces the required dynamic range of the aforementioned A/D converters.

Two complex-valued IQ pairs are formed using the four real-valued baseband signals:

$$IQ_1(n) = x_0(n) - j \cdot x_{90}(n)$$
$$IQ_2(n) = x_{45}(n) - j \cdot x_{135}(n),$$

where IQ_1 can be considered as the received signal and IQ_2 is an additional I/Q pair, needed to generate the interference estimate.

The baseband signals, x_0, x_{45}, x_{90} and x_{135}, produced by the analog front-end are subject to component mismatches and LO timing errors, which cause amplitude and phase uncertainty. As a result, the amplitude and phase difference between the received signal, r(n), and the interference estimate, v(n), are subject to this uncertainty.

Perfect cancelling of the interference requires two conditions to be met: first, the interference estimate must be a perfect representation of the interference and second, the amplitude and phase difference between the interference estimate and the interference in the received signal must be completely removed by the equalizer.

Given the above, the equalizer must be adaptive to be able to cope with the uncertainty in the phase and amplitude in order to obtain the maximum amount of interference canceling.

The equalizer consists of two single-tap FIR filters, which are formed by the complex coefficients, w_1, w_2 and the two associated multipliers shown in the grey portion of Fig. 5.9. The coefficients are adapted by applying the power-normalized LMS algorithm [25].

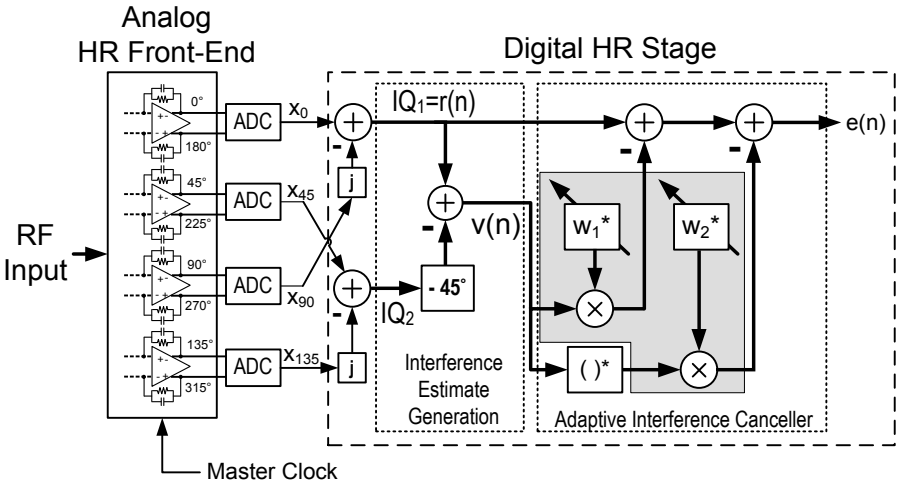

Figure 5.9: A system-level block diagram of the analog front-end, the interference estimate generation and the AIC. The equalizer of the AIC is shown in grey.

For the single interferer case (only a third or fifth-order harmonic image is present), the signal-to-interference ratio (SIR) at the output, e(n), of the digital AIC stage is determined by the inverse SIR of the interference estimate, v(n) [34]:

$$SIR_{e(n)} \approx \frac{1}{SIR_{v(n)}}. \tag{5.5}$$

To maximize the SIR at the output of the canceller, the SIR of the interference estimate must be minimized. Therefore, the aim is to generate an interference estimate that contains the least amount of desired signal energy and the maximum amount of harmonic image energy.

Generating the interference estimate

The analog baseband outputs of the front-end, x_0, x_{45}, x_{90} and x_{135}, are formed by 8-phase 1/8-period-shifted LO waveforms that approximate a sinusoid, as explained in Section 5.4. An N/8-period time shift results in a -45° phase shift for the desired signal and three & five times as much for the third and fifth harmonic images[4] . This property is exploited in the generation of the interference estimate.

[4]A time-shift is a linear phase operation. Thus, the resulting phase shift scales linearly with frequency.

Signal	IQ_1		IQ_2		Interference estimate, $v(n)$	
	Gain	Phase	Gain	Phase	Gain	Phase
Desired	1.000	0°	1.000	45°	0.000	N/A
3^{rd}	0.024	0°	0.024	135°	0.048	−45°
5^{th}	0.014	0°	0.014	225°	0.028	0°

Table 5.1: The normalized (to the desired signal) RF-to-baseband transfer characteristics of IQ_1, IQ_2 and the interference estimate $v(n)$. ***Note: this table has been corrected since the original JSSC publication.***

Considering only the relatively large (6%) approximation error of 1:$\sqrt{2}$:1 by 2:3:2 (weighting ratio of the three LNTAs), the theoretical RF-to-baseband gain and rotation of the desired and third & fifth-order signals are given in Table 5.1. For instance, it shows that the third harmonic image is attenuated by $-20 \cdot \log_{10}(0.024) = 32.4$ dB, with respect to the desired signal.

The data for IQ_1 and IQ_2 in Table 5.1 can be derived using the mixer modeling technique used in [20], which uses the Fourier series of the effective LO waveforms and the LNTA weighting ratio. Note that the phase and amplitude relations between IQ_1 and IQ_2 are *independent of the actual RF signals*, i.e. modulation schemes.

By examining Table 5.1, it follows that the interference estimate, v(n), can be generated by a -45° rotation of IQ_2, which aligns the desired signal with respect to IQ_1. Subtracting the rotated IQ_2, i.e. IQ_2', from IQ_1 results in the cancelling of the desired signal but leaves the interference:

$$v(n) = IQ_1(n) - \underbrace{IQ_2(n) \cdot \exp\left(-j \cdot \pi \cdot \frac{45}{180}\right)}_{IQ_2'(n)}. \tag{5.6}$$

The resulting signal components in the interference estimate, also shown in Table 5.1, can be derived using (5.6). For instance, it shows that the third harmonic image is attenuated by $-20 \cdot \log_{10}(0.048) = 26.4$ dB. This attenuation is solely due to the analog HR front-end and the application of (5.6). The third harmonic image, in the interference estimate, is 6 dB stronger compared to IQ_1 or IQ_2 owing to a doubling of its amplitude by (5.6). This also holds for the fifth harmonic image. In addition, the desired signal is completely cancelled, despite the 6% error in 1:$\sqrt{2}$:1. Thus, in theory, $v(n)$ can be a good interference estimate.

The adaptive interference canceller

In practical systems, however, the rejection of the desired signal in v(n) is limited by matching, just like the HR in the analog down-mixer. Fortunately, the AIC technique

does not require perfect rejection of the desired signal to give good results. Consider a third harmonic interferer and a desired signal that are equally strong after passing through the analog HR down-mixing stage. Given a realistic (matching limited) desired signal rejection of 40 dB during the interference estimate generation by way of (5.6), the SIR of the estimate, $SIR_{v(n)}$, is -40 dB. Using (5), the theoretical SIR after the AIC, $SIR_{e(n)}$, is 40dB. Then the total harmonic rejection is 40 dB plus the rejection obtained by the analog first stage (typically in the range of 30 to 40 dB).

Given the above, it should be clear that the additional harmonic rejection provided by the AIC is dependent on the SIR of the baseband signals IQ_1 & IQ_2, which is equal to the signal-to-harmonic ratios of the RF antenna signal minus the HR of the analog front-end.

Interestingly, the performance of the AIC shows a favorable trend with respect to the interference power: if the interference power increases, the quality (1/SIR) of the interference estimate *increases*, which leads to an increased SIR at the output of the canceller. In practice, the benefit of this trend is limited by the nonlinearity of the front-end, including the A/D converters.

Consider again the block diagram of the digital HR stage in Fig. 5.9. The interference estimate, $v(n)$, and its complex conjugate[5] , $v^*(n)$, are equalized via multiplying by w_1^* and w_2^*, respectively. The equalized signals are subtracted from the received signal, $r(n)$, which removes the interference and produces the output signal, $e(n)$. The filter weights, w_1^* and w_2^*, are adapted with every new output value of $e(n)$ by means of the LMS update rule [25]:

$$\begin{aligned} w_1(n+1) &= w_1(n) + \mu \cdot v(n) \cdot e^*(n) \\ w_2(n+1) &= w_2(n) + \mu \cdot v^*(n) \cdot e^*(n), \end{aligned} \tag{5.7}$$

where μ is the power-normalized step-size, normalized to the power of the interference estimate $v(n)$, i.e. P_v:

$$\mu = \frac{1 \cdot 10^{-4}}{P_v} \tag{5.8}$$

and the canceller output, $e(n)$, is calculated from the received signal, $r(n)$, by:

$$e(n) = r(n) - w_1^*(n) \cdot v(n) - w_2^*(n) \cdot v^*(n) \tag{5.9}$$

as shown in Fig. 5.9.

The LMS update rule as in (5.7) is an iterative process that aims to minimize the cross-correlation between the output of the canceller, $e(n)$, and the interference estimate, $v(n)$. Cross-correlation is a measure of similarity, thus, minimizing it results

[5]The complex conjugate is needed to remove the I/Q imbalance image [16] of the harmonic image in addition to the harmonic image itself.

in the output of the canceller being as *dissimilar* to the interference estimate as possible: the interference at the output, $e(n)$, is reduced.

The step-size parameter μ in (5.8) is chosen somewhat arbitrarily. Generally speaking, choosing μ too small results in slow convergence and choosing it too big increases the (time-varying) error of the filter weights [25], which reduces the harmonic rejection.

The optimum equalizer coefficients, w_1 and w_2, for cancelling the third harmonic image may differ from the optimum coefficients for cancelling the fifth harmonic image, owing to different phase and amplitude mismatches for each image. The dominating interference largely determines the cross-correlation. Therefore, the dominating harmonic image will be cancelled by the AIC stage. Note that the preceding analog HR down-mixer stage rejects both images.

The optimum coefficients are independent of the RF signal modulation scheme, owing to the fact that the amplitude and phase *differences* between $r(n)$ and $v(n)$ are independent of the actual RF signals. Thus, once the filter coefficients to cancel a specific harmonic image have been found (by application of the iterative LMS algorithm), they remain valid until the mismatch introduced by the front-end changes, for instance, when making large changes in the LO frequency.

5.6 Implementation of The Analog Front-End

A SDR receiver chip has been implemented in 65nm CMOS to verify the three concepts proposed in previous sections. The digital AIC algorithm is realized in software and will be discussed later. The block diagram of the chip has been shown in Fig. 5.4. The signal path consists of LNTAs, passive mixers, and two-stage TIAs with second-stage HR-weighting via a resistor network (R-net). The first voltage gain should be at baseband after LPF for good OB linearity, as discussed in Section 5.3, and the realization of two-stage polyphase HR has been described in Section 5.4. The eight-phase LO is derived via a divide-by-eight from an off-chip signal CLK, i.e. the master clock. The receiver can be reconfigured to deliver either eight-phase outputs from TIA1 or I/Q outputs from TIA2. The eight-phase outputs interface to off-chip ADCs for digitally-enhanced HR measurements while the TIA2 stage is switched off. To better understand the implementation, a more detailed description for some key blocks follows.

Linear LNTA

Fig. 5.10 shows the schematic of a pseudo-differential unit-LNTA, of which there are seven units in parallel to form three LNTAs with 2:3:2 ratio, sharing the same external (large-value) inductor to GND for DC bias. The common-gate (CG) transistor M1 provides input matching while the input is also connected to the AC-coupled inverter consisting of common-source (CS) transistors M2 and M3. For each single-ended

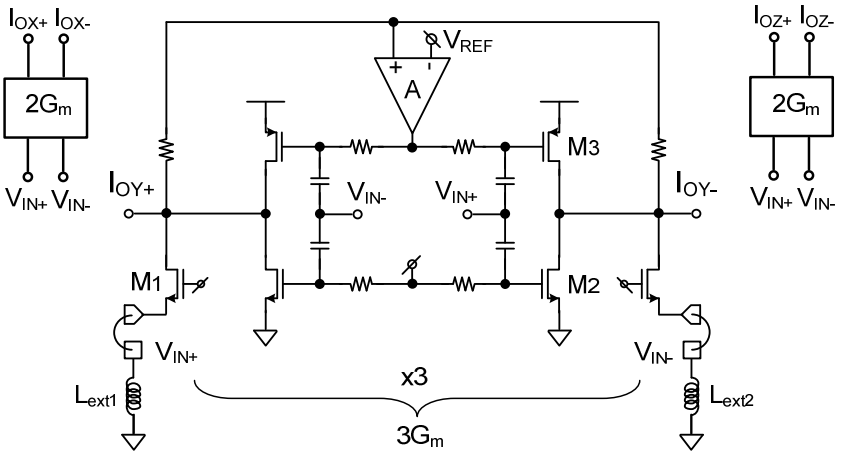

Figure 5.10: Low-noise transconductance amplifiers (LNTA) implementing $3G_m$ (shown on transistor level) and two blocks of $2G_m$ (identical schematic)

half, all seven unit-LNTAs together deliver an impedance matching with the source impedance $R_S = 50\ \Omega$ and a total transconductance $g_{m,tot} = 100$ mS ($g_{m,CG} = 20$ mS, $g_{m,CS} = 80$ mS). A common-mode feedback (CMFB) loop using high-ohmic resistors and an amplifier "A" controls the PMOS transistors and ensures all three LNTA outputs are biased around $V_{REF} = 600$ mV. In total the three differential LNTAs draw 14 mA from a 1.2V supply.

The noise behavior of the LNTA can be understood by studying a single-ended half, which consists of a CG transistor M1 and two CS transistors M2/M3, sharing the same input V_{in+}. Considering the LNTA output noise in the current domain, the noise factor can be written as:

$$F = 1 + \frac{kT\gamma g_{m,CG} \cdot \left(1 - R_s \cdot g_{m,CS})^2\right)}{kTR_s \cdot g_{m,tot}^2} + \frac{4kT\gamma g_{m,CS}}{kTR_s \cdot g_{m,tot}^2}. \tag{5.10}$$

The second term considers the partial noise cancelling of the CG transistor noise [28] and the third term considers the noise from the CS transistors. If take $R_S = 50\ \Omega$, $g_{m,CG} = 20$ mS, $g_{mCS} = 80$ mS, and $g_{m,tot} = 100$ mS into (10), we get $F = 1 + 9\gamma/25 + 16\gamma/25 = 1 + \gamma$. If γ is in the range of 2/3 to 1, the noise figure (NF) would be 2.2 to 3 dB.

For wideband operation, minimum-length transistors are used to achieve $S_{11} < -10$ dB to more than 6 GHz RF (simulation). Since the input impedance of a CG transistor depends on its drain impedance [65], a wideband low impedance at its output, i.e. node B in Fig. 5.2, is desired for wideband input matching. This fits well to what is desired for linearity as discussed in Section 5.3.

Since the LPF improves the OB linearity of I-V conversion (Fig. 1), the V-I linearity sets the ultimate limit of OB linearity. To obtain a good V-I linearity, high (V_{GS}-V_{TH}) and high V_{DS} is desired. In our VDD=1.2V design, (V_{GS}-V_{TH}) is larger than 250mV and V_{DS} is 600mV. Fig. 5.11 shows IIP3 simulation results (considering process spread), where *each* of the three LNTAs is loaded by a pair of resistors R_L to model the input impedance of the next stage mixers. To average out the effect of different LNTA transconductance (2:3:2), the simulation is carried out with all three LNTAs combined together as well as their individual R_L. The two input tones are at 801 MHz and 802 MHz. Simulations predict an IIP3 of more than +15 dBm if $R_L < 100\ \Omega$ and only ±1 dB variation over different process corners, indicating that high LNTA linearity robust to process spread is possible if we keep voltage gain low (small R_L).

Actually, it turns out that the addition of the CG-stage in parallel to the inverters has a nonlinearity cancellation effect that improves IIP3 for R_L between about 20Ω and 200Ω, which determines the V_{DS}-related distortion terms (for the case without a CG-stage, see the grey curve in Fig.5.11). Simulation and analysis indicate that it is mainly the pre-distortion at the inverter inputs introduced by the CG-stage via its source current, to cancel the distortion generated by inverter itself. Nevertheless, since we are interested in using a low R_L value, produced by mixer switches, to deliver signal current into the TIA stage, here we don't discuss this effect further.

A differential LNTA requires an off-chip balun if a single-ended antenna or RF filter is used. Compared to an LNTA with single-ended input, although the differential one may double the power consumption [66], it can render better IIP2. Besides, the input voltage swing on each of the differential inputs is lowered by 3 dB, which improves LNTA IIP3 and P_{1dB} by 3 dB.

Using the same setup as for Fig.5.11, simulations with an ideal balun and $R_L = 50\Omega$ (the designed input impedance of the mixer) show input referred $P_{1dB} = +4$ dBm, NF < 3 dB (only including noise from LNTA), and gain = -1 dB for each single-ended output (low gain as desired for good linearity) with -3 dB bandwidth > 7 GHz. This wide RF bandwidth benefits from the low impedance (real part) at the output of LNTA, which means the dominant pole is located at a very high frequency given a certain capacitance.

Passive mixer

Each of the three LNTAs with 2:3:2 ratio connects to eight passive current-commutating mixers driven by an eight-phase LO, as shown in Fig. 5.4. The mixers are DC-coupled to the LNTAs for wider bandwidth compared to AC-coupled, which introduces parasitic capacitance. Each mixer receives 3 differential inputs from LNTAs and together they deliver four differential outputs to TIA1, i.e. eight-phase signals with 45° increments.

The passive mixer simply consists of NMOS switches, with bulk tied to source. The gate of the mixer switch is AC-coupled to a clock driver and biased so that the maximum V_{GS}=VDD. The mixer switch-on resistance R_{mixer} is in the order of 50Ω

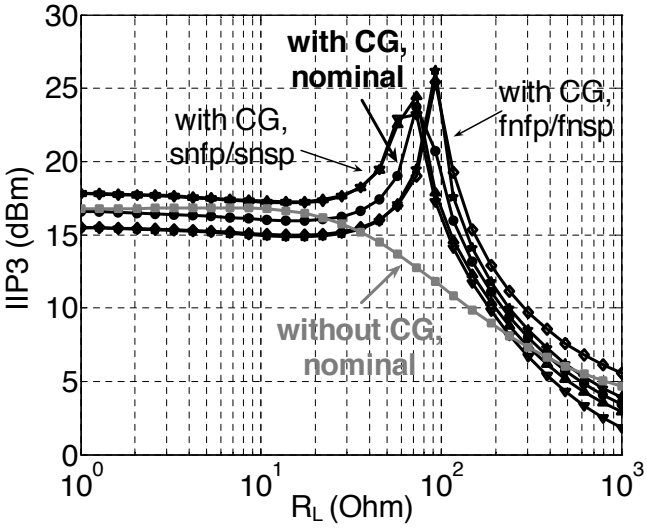

Figure 5.11: Simulated LNTA IIP3 versus load impedance (R_L for each of the three LNTAs) at different process corners (sn: slow-NMOS, sp: slow-PMOS, fn: fast-NMOS, fp: fast-PMOS).

and all mixer switches have the same dimension for good phase accuracy. Besides, the same R_{mixer} and different LNTA output impedance (3:2:3) also introduce a current division effect which brings the actual first-stage weighting ratio different from 2:3:2 but closer to the ideal 1:$\sqrt{2}$:1 ratio, good for the overall amplitude accuracy.

For good NF, we need to minimize clock overlap to avoid a low-ohmic path between TIA inputs that will amplify TIA noise [62]. For the case with 8 TIA inputs this leads to a maximum LO duty cycle of 1/8. Both sides of the mixer, i.e. the output of LNTA and the input of TIA, are biased at the same DC level (around half VDD) ensuring that little DC current flows for a low 1/f noise from the mixer switches.

Accurate multiphase clock

Since the amplitude accuracy can be ensured by the two-stage polyphase HR, the phase inaccuracy is likely to dominate. Based on the appendix in [45], if the LO duty cycle is "d", the resulting third HR (1σ) is

$$HR3 = 10\log_{10}\left(\frac{\sin^2(\pi\cdot d)}{\sin^2(3\pi\cdot d)}\cdot\left[\left(\frac{\sigma_A}{12}\right)^2+\left(\frac{\sigma_\varphi}{4}\right)^2\right]^{-1}\right) \tag{5.11}$$

,where σ_A and σ_φ are the standard deviation in the amplitude and phase respectively. For d=1/8 and negligible amplitude error ($\sigma_A \to 0$) due to the two-stage technique

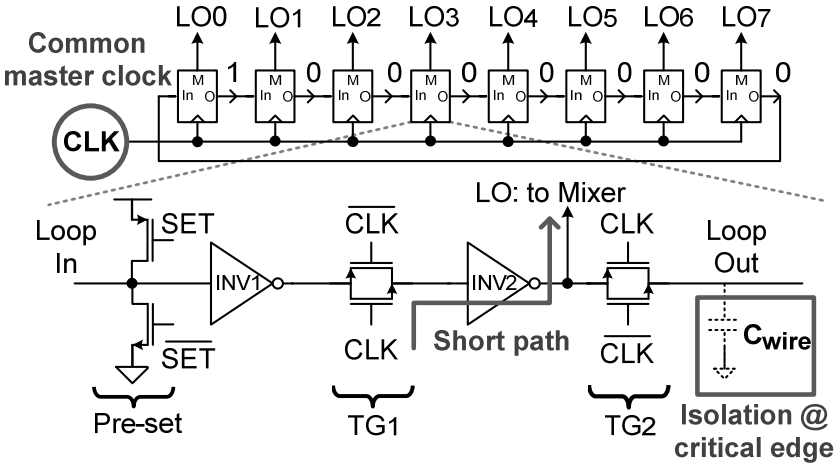

Figure 5.12: An eight-phase clock generator with low phase mismatch (with one cell shown on transistor level).

as in (5.4), to reach 60 dB HR (3σ), the required phase error is $\sigma_\phi = 0.03$.

To build a multiphase clock generator with low phase mismatch, two design principles are applied: 1) to use a common master clock to derive all phases; 2) to minimize the path from the common master clock to the mixer switches therefore to minimize mismatch accumulation.

Fig. 5.12 shows a divide-by-eight ring counter using eight dynamic transmission-gate (TG) flip-flops (FF). The same master clock (CLK), with eight times the LO frequency, drives all FFs. Only one inverter (INV2) is used as a buffer to minimize the path from CLK to mixer.

A preset data pattern is required to deliver the wanted 1/8 duty cycle. Each LO phase controls 6 mixer switches connecting to differential outputs of three LNTAs. The gates of all the 6 switches are connected together and driven by the same buffer, i.e. INV2, to minimize buffer mismatch.

In a ring counter, all flip-flops "see" the same environment. However, a loop is not convenient in layout and it may need different wiring lengths between each two flip-flops, degrading phase accuracy. A careful layout strategy is adopted to minimize the wiring differences. Moreover, when the critical LO edges occur, the largest part of the wiring is isolated from the output of INV2 via TG2, decreasing rise and fall times and reducing the effect of wiring mismatch.

The phase error reported in [14] is found to be too pessimistic due to an incorrect simulation test-bench. Fig. 5.13 presents the simulated phase deviation from 45° between two adjacent 0.8GHz LO phases due to mismatch, including the contribution from mixer switches. The histogram shows a maximum phase error of only 0.07 and it

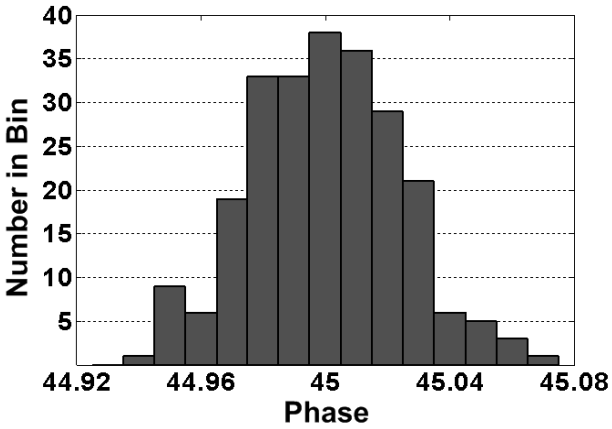

Figure 5.13: Histogram of the simulated phase difference between two adjacent LO outputs (240 Monte Carlo results).

yields $\sigma = 0.024$, i.e. 0.08 ps for 0.8 GHz. This clock performance is hence compatible with HR>60 dB (3σ).

The master clock CLK comes from an off-chip generator followed by a pair of inverters as on-chip buffer. Simulation shows, at 0.8 GHz LO, the power consumption of the divider is 5.4mA at 1.2V supply and the input buffers consume 8.9mA driven by 6.4 GHz differential input clock.

In simulation, the divide-by-eight can work up to 1.25 GHz LO (10 GHz CLK) in nominal case although it can vary with process corners. The up-side LO frequency is mainly limited by the large division ratio, i.e. eight. If a higher LO frequency is wanted, a divide-by-two may be used to generate four-phase (quadrature) LO instead of the divide-by-eight, and then the receiver in Fig. 5.4 can be reconfigured to a quadrature wideband receiver without HR [67], when harmonic mixing is less to be a problem at higher bands.

High-swing TIA and baseband R-net

Since the voltage gain occurs at the outputs of the TIA1 stage where interference is only partly suppressed, we choose an OTA topology being able to handle large voltage swing, which helps tolerate large blockers. It is a two-stage class-AB-output OTA based on [68]. The input pair uses NMOS transistors in weak inversion for high g_m/I_{DC} and a big size leading to low 1/f noise. For the OTA second stage, a class-AB push-pull output stage is used, which can handle more than 2V peak-to-peak differential output voltage swing. Each OTA draws 3mA from 1.2V supply.

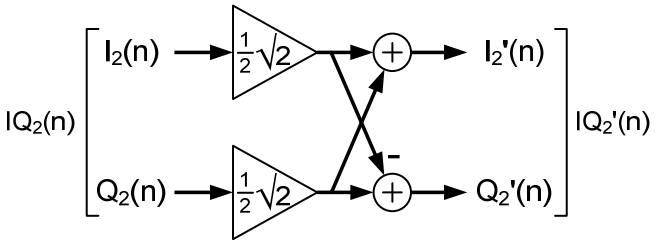

Figure 5.14: Reduced complexity -45° phase shifter.

A parallel RC feedback network implements a simple first-order LPF to perform blocker filtering (Fig. 5.4). Each TIA stage has a LPF -3 dB bandwidth of 20 MHz and together they determine the receiver IF bandwidth of 12 MHz, which may accommodate most mobile communication standards. The virtual-ground impedance of the TIAs is about 4Ω around DC and peaks to 60Ω around 700 MHz. The simulated gain after the TIA1 stage is 27 dB and after the TIA2 stage 34 dB.

The resistor network (R-net) provides the second-stage weighting for HR. It also converts eight-phase outputs of the TIA1 stage into quadrature inputs of the TIA2 stage. To form a 5:7:5 amplitude ratio, 19 unit-resistors form a resistance ratio of 7:5:7 in 3 paths. Harmonic rejection at baseband (via R-net) can also reduce errors due to parasitic capacitance compared to at high frequency.

5.7 Implementation of The Digital Back-End

The analog front-end used in the digitally-enhanced HR architecture consists of the first stage HR mixer driven by the multi-phase clock generator of the two-stage analog HR architecture. The reader is referred to the previous section for the implementation details of the analog circuits.

The four fully-differential baseband outputs provided by the TIA1 stage (Fig. 5.4) are converted into the digital domain using a commercial A/D board comprising four 14-bit ADCs (Fig. 5.9). Unfortunately, the input range of the used A/D board was more than 15 times greater than the output swing provided by the front-end, resulting in less than 10 effective bits.

The baseband processing, including the interference estimate generation and the adaptive interference canceller were implemented in software on a PC and use floating-point arithmetic. To allow real-time processing, a sampling rate of 4MS/s was chosen. This gives 2 MHz bandwidth for each analog baseband signal and 4 MHz bandwidth in the digital domain using quadrature signals. Fig. 5.9 gives a system-level overview of the setup.

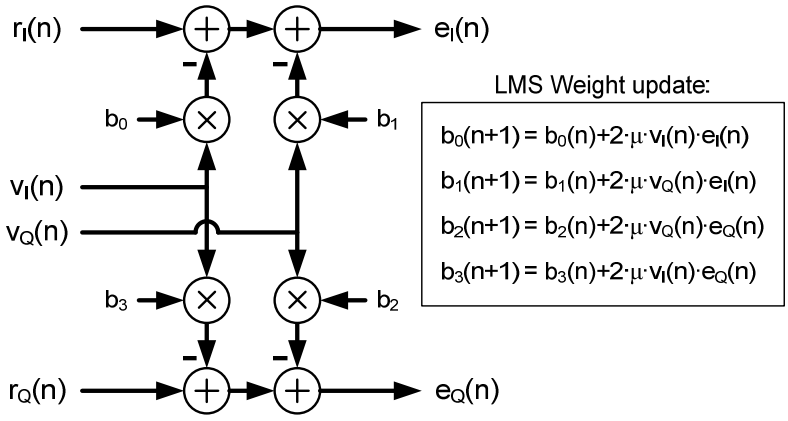

Figure 5.15: Reduced complexity interference canceller.

The interference estimate generation is implemented using two real adders and the phase shifter, shown in Fig. 5.14. This reduced-complexity shifter exploits the fact that the cosine and sine of a 45° angle are of equal magnitude. Thus, it needs two real multipliers (instead of four) and two real adders. Thus, the total complexity of the interference estimate generation is two real multipliers and four real adders.

The complexity of the canceller indicated by (5.9) can be reduced from eight multipliers and eight adders to four multipliers and four adders, by applying the following substitutions:

$$b_0 = w_{1,I} + w_{2,I} \qquad b_1 = w_{1,Q} - w_{2,Q}$$
$$b_2 = w_{1,I} - w_{2,I} \qquad b_2 = -w_{1,Q} - w_{2,Q},$$

where the filter coefficients, w_1 and w_2, are split in their real and imaginary parts, $w_{1,I}$, $w_{1,Q}$, etc. The resulting canceller and the new LMS update rules are shown in Fig. 5.15. If the step-size μ is rounded to the nearest power of two, four multipliers in the "LMS Weight update" become a shift operation. As a result, the update mechanism only needs four multipliers and four adders. Then, the total arithmetic complexity of the digital HR stage is ten multiplications and twelve additions per sample.

While the digital algorithm was implemented only in software, a fixed-point VHDL version was synthesized using a 65nm CMOS standard cell library. The tools reported a dynamic power of less than 10mW at 100 MS/s and 1.2V supply voltage.

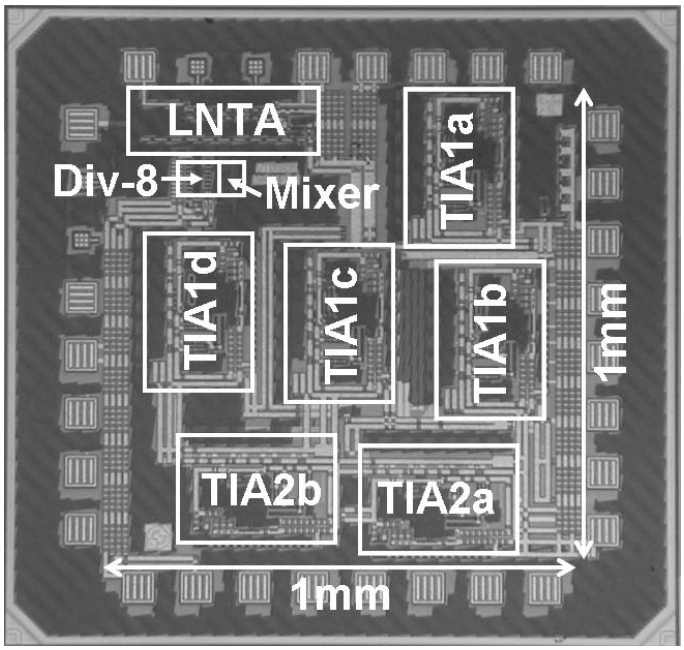

Figure 5.16: 65nm CMOS chip micrograph indicating some functional blocks.

5.8 Experimental Results

The circuit shown in Fig. 5.4 is fabricated in 65nm CMOS and the micrograph is shown in Fig. 5.16. The total area, excluding bond-pads, is about 1mm^2. Capacitors (C_{FB} and C_{VG} in Fig. 5.2) take a large portion of area in the TIA, and also the OTA input pair is big to achieve a low 1/f noise corner. With 1.2V supply, the analog power consumption is 33mA (LNTA: 14mA, TIA 1-stage: 12.8mA, TIA two-stage: 6.4mA) while the clock power consumption is 8mA at 0.4 GHz LO and 17mA at 0.9 GHz LO, including the clock input buffers.

The chip is packaged in a 32-pin Heat-sink Very-thin Quad Flat-pack No-leads (HVQFN) package. To prove the receiver is robust to OBI, all measurements are performed on PCB without any external filter. Two SMD inductors are mounted on the PCB to bias the LNTA (Fig. 5.10). Both the receiver inputs and clock inputs are differential and wideband hybrids (balun) were used to interface to single-ended 50Ω measurement equipments. The IF-output voltages are sensed by a differential active probe that performs differential to single-ended conversion and impedance conversion to 50Ω. The characteristics of all components and cables for testing are de-embedded from the results.

The divide-by-eight works up to 0.9 GHz LO, and the measured S_{11} is lower than

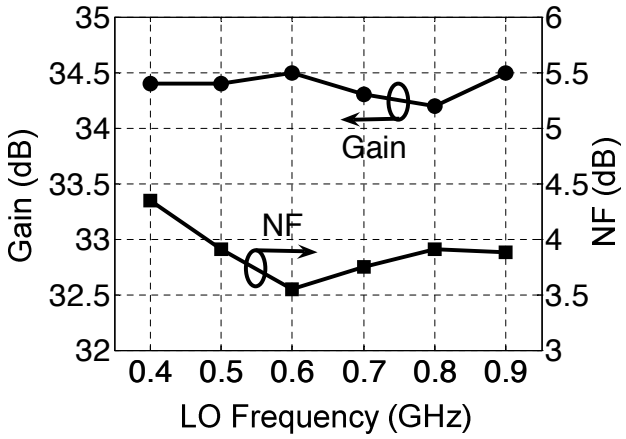

Figure 5.17: Measured voltage gain and DSB NF of the two-stage receiver as a function of the LO frequency.

-10 dB up to 5.5 GHz. This means the HR measurement is valid for 0.9 GHz LO up to its sixth harmonic. The measured IF bandwidth is 12 MHz and the baseband 1/f noise corner is 30 kHz thanks to the passive mixer with little DC current and the OTA with a large-sized input pair.

Gain, NF, RF bandwidth, and in-band IIP2/IIP3

Fig. 5.17 shows the measured voltage gain and DSB NF over an LO frequency of 0.4 to 0.9 GHz. The voltage conversion gain, measured for an IF of 1 MHz from the input of the balun to the differential outputs of receiver, is above 34 dB over the whole band and is quite flat (±0.2dB variation), indicating a much wider RF bandwidth. The NF is measured for an IF of 10 MHz since the available NF analyzer (Agilent N8973A) starts from that frequency. The DSB NF is below 4 dB except for 0.4 GHz where 1/f noise from the LNTA starts to dominate.

The divide-by-eight limits the LO frequency range up to 0.9 GHz (master clock @ 7.2 GHz), but the signal-path -3 dB RF bandwidth is much wider, up to 6 GHz. To verify it, we conducted a gain measurement for the seventh harmonic, i.e. the first non-canceled high-order harmonic. Ideally, using 1/8 duty-cycle LO, the strength of the seventh harmonic should be 1/7 of the fundamental harmonic, so we expect the seventh harmonic should ideally have a gain that is 16.9 dB (1/7) lower from 34 dB, i.e. 17.1 dB. Indeed, the gain drops from 17 dB at 0.7 GHz RF to 14.3 dB at 6 GHz RF (LO: 0.1 to 0.85 GHz), which means the OBI will only be attenuated a little by the frequency roll-off at RF. It also indicates that the receiver can be readily expanded

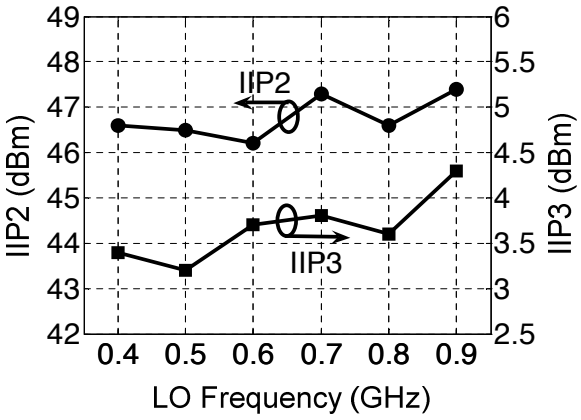

Figure 5.18: Measured in-band IIP2 and IIP3 versus LO frequency.

to cover higher bands by extending the LO range as discussed in Section 5.6.

Fig. 5.18 shows the measured in-band (IB) IIP2 and IIP3 over LO frequency, with two tones close to the LO frequency so that they are not affected by IF filtering (IIP2: f_{LO}+3 MHz and f_{LO}+6.01 MHz; IIP3: f_{LO}+3MHz and f_{LO}+3.01MHz). After downconversion, the IM2 component at 3.01 MHz and the IM3 component at 2.99 MHz are measured. The IB IIP3 is around +3.5 dBm, which is good given the high gain of 34 dB, thanks to only voltage gain at baseband with negative feedback. The IB IIP2 is above +46 dBm.

Out-of-band IIP2/IIP3

We also measured the out-of-band (OB) IIP2 and IIP3. Due to the LPF behavior, the measured OB linearity depends on the distance from f_{LO} to the two RF tones used. For sufficient distance, the LPF will suppress the downconverted two-tone interference so the OB nonlinearity is mainly contributed by the V-I of the LNTA.

The OB IIP3 is tested via two tones at 1.61 GHz and 2.40 GHz with an LO at 819 MHz, so that the IM3 is at 820 MHz RF and 1 MHz IF. The results of both IB (0.8GHz LO) and OB IIP3 are shown in Fig. 5.19. Without fine tuning, the measured OB IIP3 is +16 dBm, which agrees with the simulated results in Fig. 5.11. Compared to the IB IIP3 of +3.5 dBm, the OB IIP3 is dramatically improved because the TIA was dominating the IB IIP3, due to the high voltage gain at the output. As shown in the figure, the range for which IM3 follows the extrapolation line is also improved by almost 20 dB (upper limit of -30 dBm for IB versus -10 dBm for OB). This is crucial to tolerate large OB interference.

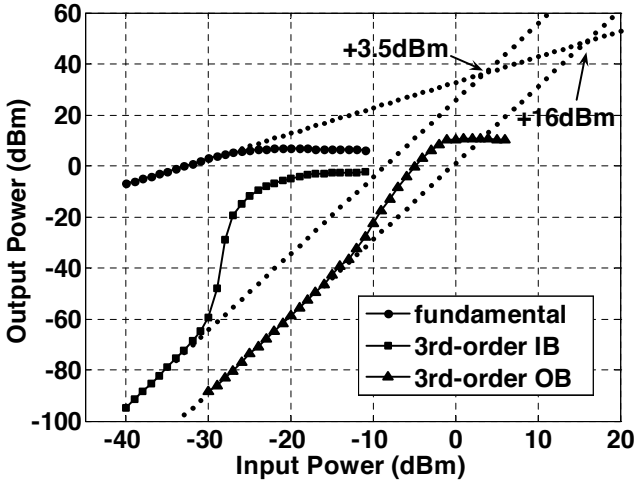

Figure 5.19: Measured in-band (IB) and out-of-band (OB) IIP3 for 800 MHz LO demonstrating OB linearity improvement.

The OB IIP2 is +56 dBm, tested via two tones at 1.80 GHz and 2.40 GHz while LO at 601 MHz, so that the IM2 is at 600 MHz RF and 1 MHz IF.

1dB compression point and blocker filtering

To quantify the effect of the blocker filtering, we measured the 1 dB compression point (P_{1dB}) and the 1 dB desensitization point (B_{1dB}), both input referred.

First we measured the P_{1dB} without applying any blockers, which is -22 dBm. The result is reasonable since -22 dBm input power plus 34 dB gain is equal to 12 dBm output power (referring to 50Ω), differentially. The single-ended voltage swing is about 1.27V peak to peak, just exceeding the 1.2V supply. This means the limitation is at the receiver output and the P_{1dB} can be improved by automatic gain control (AGC).

A more serious problem is to receive a weak signal at the same time with a strong interferer: a so-called blocker test. In this situation AGC doesn't help since the maximum gain is required to maintain sensitivity. The measurement was carried out with the LO at 400 MHz and the desired RF signal at 401 MHz with -50 dBm input power. The blocker frequency is varied from 402 MHz to 4.002 GHz. Fig. 5.20 shows B_{1dB} versus the blocker frequency. As predicted by (5.1) and (5.2), we see two effects in the figure: 1) the tolerable blocker power depends on the frequency distance between the LO and the blocker, due to the LPF behavior[6] ; 2) HR also plays a role

[6]The actual behavior of the LPF is more complicated than (5.2), since our baseband filter

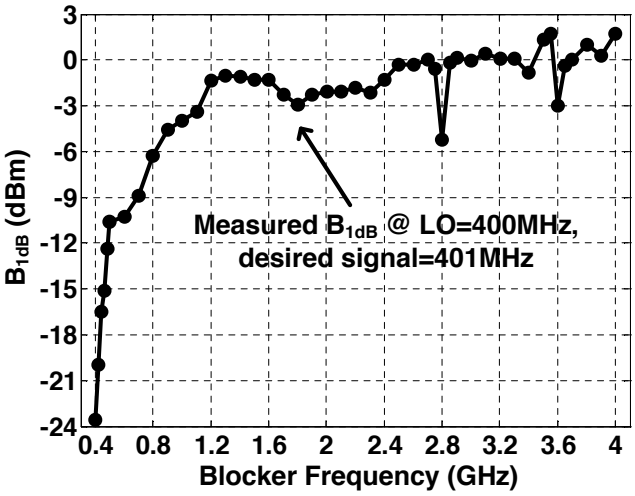

Figure 5.20: Measured input-referred 1 dB desensitization point (B_{1dB}) versus blocker frequency.

in blocker filtering, as two dips occur around seventh and ninth harmonic of the LO frequency, both of which are not rejected well by the eight-phase HR. From the figure, we can observe that B_{1dB} is better than P_{1dB}(-22 dBm) except very close-by blockers (402 MHz) and the maximum B_{1dB} is more than 0 dBm, showing the blocker filtering is indeed effective.

Two-Stage Polyphase Harmonic Rejection

We will verify the analog two-stage polyphase HR here and the digitally-enhanced HR in Section 5.8, page 97. These two alternative approaches will be compared in Section 5.8, page 100.

First we look at the two-stage polyphase HR. The HR ratio can be measured by comparing the gain difference between the desired signal and the harmonic image. At the receiver input, the desired signal power was -50 dBm while the harmonic image power was -30 dBm.

Fig. 5.21 shows, for one chip, the HR of 1-stage, at the outputs of the TIA1, and the total two-stage HR, at the outputs of the TIA2, versus LO frequency. The HR of 1-stage is between 30 and 40 dB and the HR of two-stage is around 70 dB, representing a 30 dB improvement for both third and fifth HR thanks to the two-stage polyphase HR technique. Generally, the HR improvement from the first stage to the second stage is

is cascaded in two stages, which does not follow a simple first-order or second-order filtering behavior.

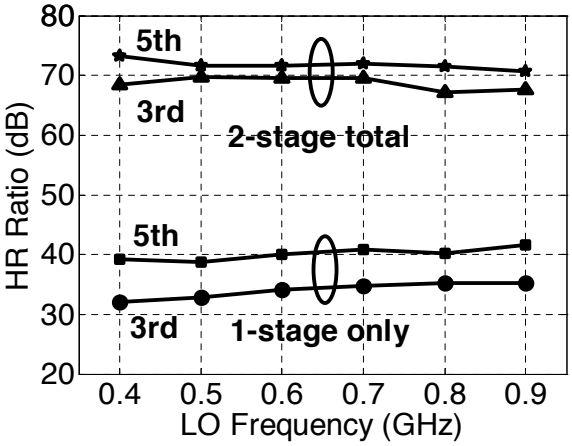

Figure 5.21: Measured HR ratio versus LO frequency: Comparison between HR width only one-stage and total two-stage (two-stage polyphase HR).

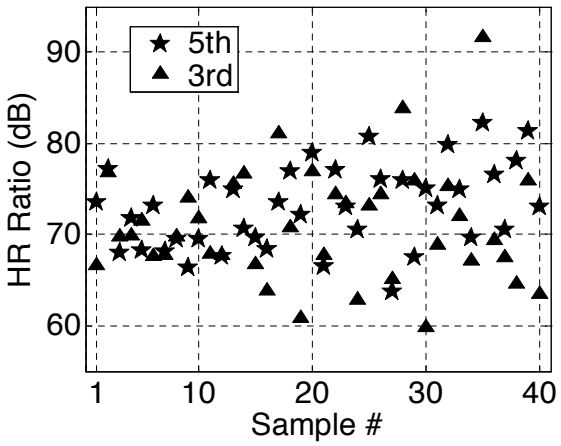

Figure 5.22: Measured HR ratio of 40 randomly selected chips at 800 MHz LO (two-stage polyphase HR).

in the range of 20 to 40 dB as observed from multiple chips. The large improvement also shows that it is the amplitude error dominating the first-stage HR.

To identify the effect of mismatch, we measured the HR of the two-stage configuration for 40 chips at 0.8 GHz LO, as shown in Fig. 5.22. The minimum third order HR is 60 dB and the minimum fifth order HR is 64 dB. The second, forth, and sixth HR is also measured, over 20 chips. The minimum second-order HR is 62 dB, while

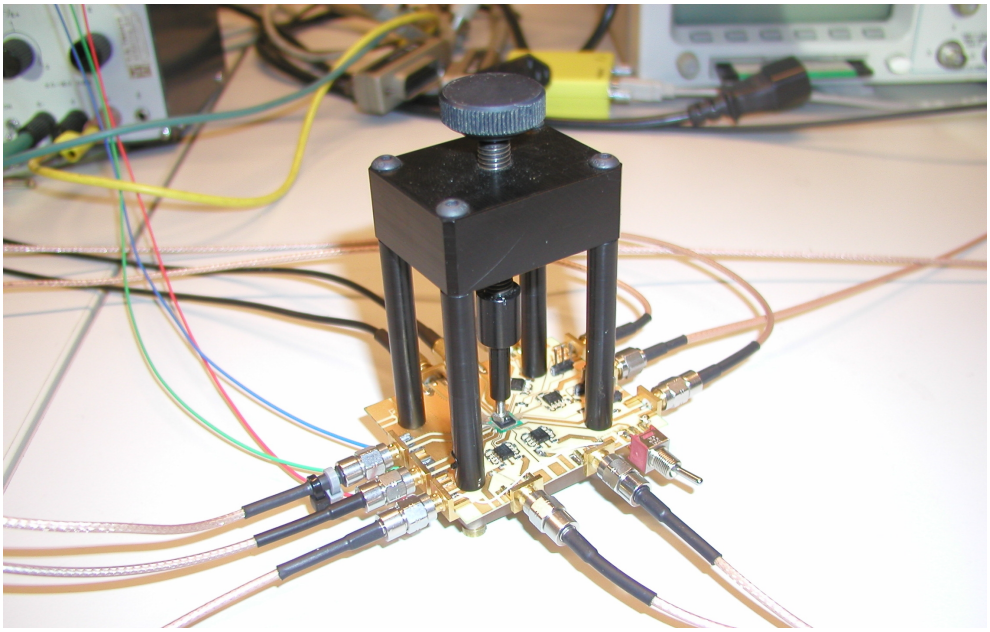

Figure 5.23: A picture of the measurement setup for evaluating the dual-domain harmonic rejection performance.

the minimum forth and sixth order HR are both 67 dB. These results are achieved without calibration, trimming, or RF filtering.

Since the signal-path -3 dB RF bandwidth has been characterized to be up to 6 GHz, the contribution of the frequency roll-off to the HR result should be small. According to (5.11), the simulated phase error $\sigma = 0.024$ means a minimum HR (3σ) of 62 dB if the amplitude error is eliminated, fitting well with the measured HR as well as the Monte Carlo simulation results. This also suggests that phase error can indeed be the limitation now.

Digitally-enhanced HR

Consider now the digitally-enhanced HR architecture. The harmonic rejection for the third harmonic image versus LO tuning range (0.4 to 0.9 GHz) was measured using the setup show in Fig. 5.23. The results are shown in Fig. 5.24. At the receiver input, the desired signal RF power was -66.1 dBm and the harmonic image RF power was -20.1 dBm. The analog HR mixer provides more than 36 dB HR for the third harmonic image, which is higher than the 32.4 dB predicted by Table 5.1. We attribute this difference to the finite output impedance of the three LNTAs. Thus, the effective weighting of the 2:3:2 ratio is closer to the ideal 1:$\sqrt{2}$:1, resulting in a higher measured HR.

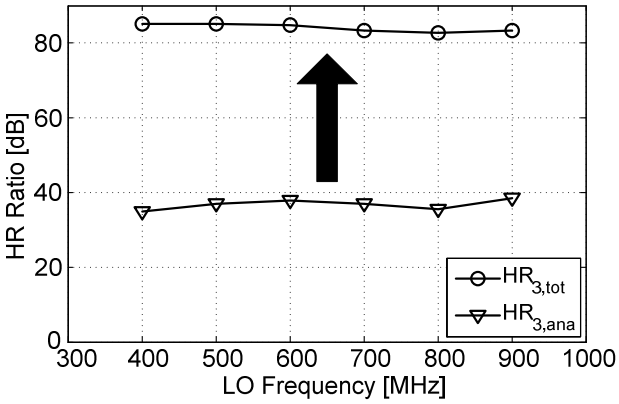

Figure 5.24: The measured third-order HR of the analog stage and the combined stages versus the LO frequency. Desired: -66.1 dBm RF power, third harmonic image:-20.1 dBm RF power (digitally enhanced HR).

Given a SIR of -46 dB at RF, the digital AIC increases the harmonic rejection provided by the analog HR mixer from 36 dB to over 80 dB across the entire LO tuning range. The HR measurements are calculated based on the difference in power between the desired signal and the harmonic image. At the output of the digital canceller, the harmonic image is below the noise floor. Instead of the harmonic image power, the noise floor was taken. Thus, the actual HR is greater than what is shown in Fig. 5.24.

A second indicator that the HR is higher comes from the SIR of the interference estimate, v(n), which was measured to be over 52 dB (limited by noise floor of equipment) across the entire LO tuning range. Given (5.5), the (theoretical) SIR at the output of the canceller is also 52 dB. The power ratio between the desired signal and the harmonic image (at RF) is -46 dB, which makes the theoretical HR greater than 98 dB! Unfortunately, the height of the noise floor at the output of the canceller, which is largely determined by the quantization noise of the A/D board, prevents this to be verified.

The third and fifth-order harmonic rejection for multiple (randomly selected) chips is shown in Fig. 5.25. The desired signal RF power was -66.1 dBm at 800 MHz LO. The RF power of the third and fifth-order harmonic images was -20.1 dBm. The results show more than 36dB of analog harmonic rejection and more than 80 dB of combined harmonic rejection, for all chips. Thus, the digitally-enhanced AIC technique performs well under varying mismatch conditions.

To show the effectiveness of the AIC technique against a modulated interferer, an FM modulated third harmonic image interferer was applied to the system. Fig. 5.26

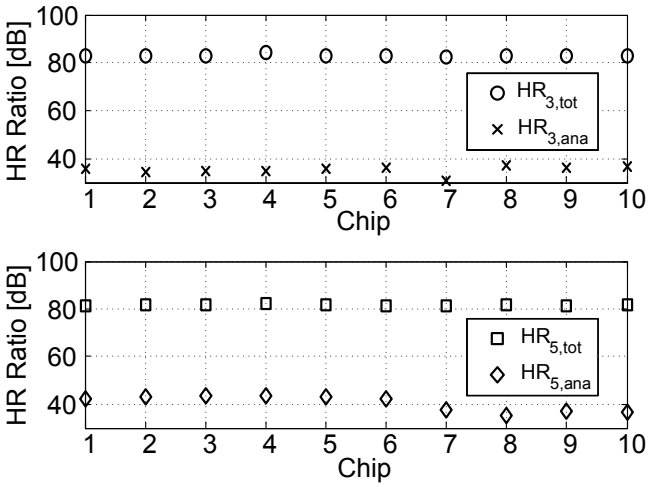

Figure 5.25: The measured thrid and fifth-order HR of the analog stage and combined stages, for 10 randomly selected chips, at 800 MHz LO (digitally enhanced HR).

shows the baseband spectrum of the received signal (top), r(n), and the AIC output (bottom), e(n).

In the received signal (Fig. 5.26, top), the third harmonic image signal at -1.25 MHz (baseband) causes interference to a (sinusoidal) desired signal at -1.45 MHz (baseband). The I/Q imbalance image of the third harmonic interferer is also visible at +1.25 MHz (baseband).

At the output of the canceller (Fig. 5.26, bottom), the third harmonic interferer is below the noise floor, which is a suppression of more than 40 dB. Assuming at least 36 dB of analog harmonic rejection, the combined harmonic rejection is thus more than 76 dB. This is less than 80 dB because the FM modulated interferer was weaker than the sinusoidal interferer used during the previous measurements.

Fig. 5.26 also shows signals which are caused by ground loop problems and spurs emanating from the switching power supply of the PC, which housed the A/D converter board.

Note that the I/Q imbalance image of the third harmonic interferer, see Fig. 5.26 (top), is suppressed to below the noise floor, revealing the I/Q imbalance image of the desired signal, see Fig. 5.26 (bottom), at +1.45MHz (baseband).

After convergence of the LMS algorithm, which takes around 50000 samples (12.5 ms), the equalizer coefficients were:

$$w_1 = 0.4852 - j0.0086$$

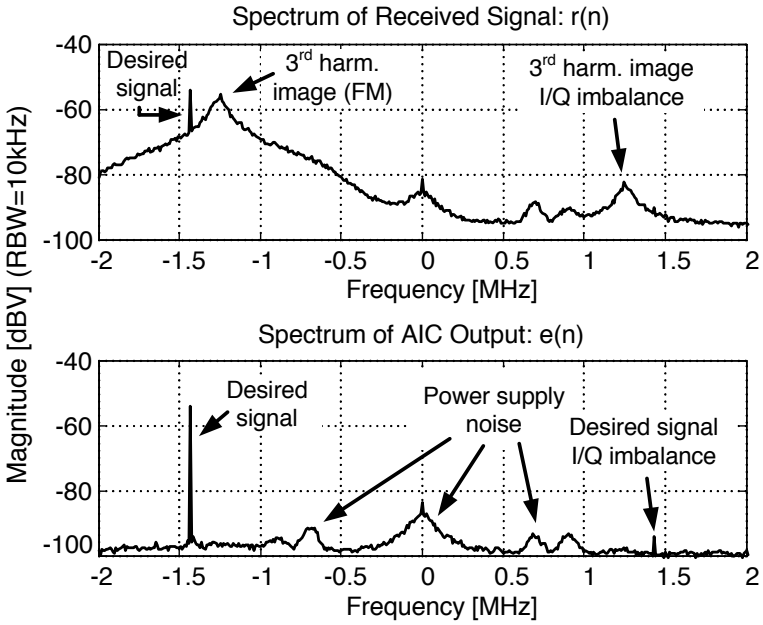

Figure 5.26: (top) The measured baseband spectrum of the (discrete-time) received signal, $r(n)$, and (bottom) the output of the canceller, $e(n)$.

and

$$w_2 = 0.0221 + j0.0122.$$

The measurements show that the digitally-enhanced HR approach is indeed a powerful one; it produces unprecedented HR figures, irrespective of (small) analog mismatches that exist in the analog front-end.

Comparing the alternatives

The two-stage polyphase HR implemented in analog approach helps both third *and* fifth HR via improved amplitude accuracy and achieves a minimum rejection of 60 dB and 64 dB respectively. The digitally-enhanced HR based on AIC algorithm consistently shows more than 80 dB of HR for a single harmonic image (either the third *or* the fifth) by correcting both amplitude and phase of that harmonic image. The other harmonic image is rejected by at least 36 dB, not improved from the analog first stage. They share a similar limitation on even-order HR.

On the implementation level, compared to the two-stage polyphase HR, the digitally-enhanced HR architecture requires two additional A/D converters, which may increase

	Analog two-stage	Digital AIC
Rej. strongest	>60 dB	>80 dB (*)
Rej. other odd.	>64 dB	>36 dB
Rej. even	>62 dB	>64 dB
Power DSP	N/A	<8.5mA @ 1.2 V (simulated)
#ADCs	2	4

Table 5.2: Comparison of two alternative HR techniques robust to mismatch. (*) = if one harmonic image band is dominating.

LO Frequency	0.4 to 0.9 GHz
Gain	34.4 dB ± 0.2 dB
DSB NF	4 dB ± 0.5 dB
S_{11} < -10 dB	80 MHz to 5.5 GHz
-3 dB RF Bandwidth	Up to 6 GHz
In/Out-of-band IIP3	+3.5 dBm / +16 dBm
In/Out-of-band IIP2	+46 dBm / +56 dBm
-3 dB IF Bandwidth	12 MHz
1/f noise corner	30kHz
Analog polyphase HR	2..6th: >60 dB
Digital AIC HR	>80 dB (strongest image)
Technology	65nm CMOS
Supply Voltage	1.2V
DC Current	50mA max.

Table 5.3: Summary of measured key performance.

the power considerably. Fortunately, the converters for x_{45} and x_{135} (Fig. 5.9) may be switched off when the analog HR stages can provide enough harmonic rejection.

Table 5.2 summarizes the results and properties of the two alternative approaches.

Performance summary and benchmark

Table 5.3 summarizes the measured performance. As a benchmark, Table **??** shows a comparison to other recently published wideband receivers with HR. Since it's difficult to characterize the exact overhead of the part implemented in software (digital AIC), here we only compare the part implemented on chip (Fig. 5.4) to other work.

There are two outstanding parameters of this work, i.e. linearity and harmonic rejection. Comparing all work including an LNA, [47], [48], and [70] shows an IIP3

Benchmark	CMOS tech.	Freq (MHz)	Gain (dB)	NF (dB)	IIP3 (dBm)	HR3 (dB)	HR5 (dB)	Chip #	Cal.	Power (mW)
This work	65nm	400-900 (a)	34	4	+3.5	60	64	40 min.	No	60
LNA + Mixer + Divider										
Bagheri [47]	90nm	800-5000	36	5	-15 (b)	38	40	1	No	51
LNA + Mixer + Divider, performance at 900 MHz										
Lerstaveesin [48]	180nm	48-860	83	4 to 7	-14	42 (c)	?	1	No	468 (c)
LNA + Mixer + BB Filter + VGA + ADC + PLL										
Ru [58]	65nm	200-900	2	19	+11	41	44	10 av.	No	19
No LNA, only Mixer & multiphase clock										
Maxim [69]	130nm	40-1000	?	16	+20	63	64	1	No	450
No LNA, only Mixer & multiphase clock										
Cha [70]	180nm	48-862	35	8	-15	72	45	10 min.	Yes	189
LNA + Mixer + Divider										

Table 5.4: Benchmark with other recent work.
(a) - Only LO frequency range, while measured RF bandwidth is up to 6 GHz.
(b) - IIP3 is derived for the full-gain setting which is required to match the 5 dB NF.
(c) - Both the HR3 and the power data exclude the contribution of the RF tracking filter.

around -15 dBm while this work shows an IIP3 of +3.5 dBm and a competitive NF. The OB IIP3 of our work is even higher (+16 dBm), but we did not find a good way to benchmark it. For HR, only [69] and [70] reported numbers comparable to this work. However, [69] only reported results from one chip while consuming large power due to a different structure of the HR mixer. [70] reported results for 10 chips, but relying on hand calibration, and the calibration is only effective for either third or fifth HR but not for both at the same time. Thus we conclude that our design has both good linearity and good HR at moderate power consumption, thanks to the proposed techniques.

5.9 Conclusions

This paper identified out-of-band (OB) nonlinearity and harmonic mixing as two main problems for *out-of-band interference* (OBI), and proposed solutions to reduce their effects. First, OB nonlinearity can be improved by implementing low-pass filtering, simultaneously with voltage gain only after downconversion, to improve the OB IIP3 and the desensitization point due to blockers. Second, two "iterative" harmonic-rejection (HR) techniques are presented to reduce harmonic mixing in a way which is robust to mismatch. An analog two-stage polyphase HR concept is proposed to greatly enhance the amplitude accuracy for both third and fifth harmonics so that the total amplitude error becomes product of errors. Alternatively, digitally-enhanced HR based on adaptive interference cancelling (AIC) can be applied to improve HR of the analog first-stage further by correcting both amplitude and phase errors for one dominant harmonic, either third or fifth. To guarantee a mismatch-robust HR for both analog and digital approaches, a simple but accurate ring counter is presented to generate the multiphase clocks driving the HR mixer.

We have verified the proposed techniques via a SDR receiver in 65nm CMOS, with RF bandwidth up to 6 GHz and 8-phase LO frequency up to 0.9 GHz (master clock up to 7.2 GHz). The 1 dB compression point is -22 dBm while the maximum 1 dB desensitization point is more than 0 dBm, showing the low-pass blocker filtering is effective. In terms of IIP3, +16 dBm for OBI is measured without fine tuning for sufficient frequency spacing, e.g. LO at 819 MHz while two-tone at 1.61 and 2.40 GHz, versus an in-band IIP3 of +3.5 dBm. Without any trimming or calibration, the two-stage polyphase HR technique achieves 60 dB minimum HR ratio at 0.8 GHz LO for both third and fifth harmonics over 40 randomly-selected chips, and all even-order HR ratios are measured above 60 dB as well. The digital AIC HR achieves a steady 80 dB HR for either third or fifth harmonic for 10 chips, indicating the power of adaptive digital techniques to solve analog problems.

Chapter 6

A Spectral Sensing Technique for Cognitive Radios in the Presence of Harmonic Images

This chapter appeared in the proceedings of the DySPAN conference [71] and is a complete reproduction thereof.

6.1 Introduction

Cognitive radios ideally support a large frequency range, one that spans multiple octaves. Generating the local oscillator (LO) signals for such a wide range of frequencies is predominantly achieved using digital circuits[37]. For instance, digital frequency dividers are used to divide the output of a high-frequency oscillator. In this way, a frequency synthesizer that spans a multiple-octave frequency range can be realized. However, such a frequency synthesizer generates a digital square-wave LO signal, which contains many harmonics in addition to the fundamental frequency.

The direct-conversion receiver has a low external component count compared to other receiver architectures, such as the superheterodyne. It is therefore the architecture of choice when high-integration and low-cost are desired. Such features are important in consumer applications, such as PDAs, mobile phones and laptops. However, when the mixers are driven by digital circuits, they suffer from *harmonic downmixing*[1].

[1] All radio architectures can suffer from harmonic downmixing. Here we limit ourselves to direct-conversion receivers as the harmonic downmixing problem is most severe in such receivers.

Harmonic downmixing is an undesirable effect whereby RF signals found at multiples of the local oscillator frequency, termed *harmonic images*, are downmixed to baseband, in addition to the desired signal. The effect is caused by harmonics in the local oscillator signal, which have significant strengths for a square-wave LO. The harmonic images cause interference to the desired signals and will degrade the bit-error rate (BER) at the decoder, or even make the desired signals undecodable. Harmonic downmixing also causes problems in spectrum sensing applications, such as in cognitive radio networks. The spectrum sensing algorithm, which is often based on energy detection or power spectral density measurements, will mistake an harmonic image signal, which is outside the band of interest, for a signal that is within the band of interest. As a result, certain parts of the spectrum are erroneously flagged as occupied while they are empty in reality.

Harmonic downmixing is an effect that must be taken into account when driving mixers using LO signals containing more than a single frequency, such as digital signals. However, this effect is neglected in most papers as they assume perfect sinusoidal LO signals and perfect multiplying mixers, or sufficient RF filtering. In practice, perfect sinusoidal signals and perfect multiplying mixers are not realizable. Sufficient RF filtering is expensive, bulky and can be difficult to implement.

In this paper, we present an algorithm based on cross-correlation of two baseband signals, r_1 and r_2. Both contain signals from the desired spectrum and from the harmonic images. A frequency offset Δf is used in the analog frontend to frequency shift the harmonic images and the desired signal by different amounts. After a frequency shift, $-\Delta f$, in the digital domain, the desired signal in r_1 and r_2 cross correlate. This principle allows correct spectrum sensing under conditions where harmonic images are present.

This paper is organized as follows. In the following section, a mixer model is developed that shows how multiple RF signals are downmixed to baseband and how they relate to the fourier series of the LO waveform. Then, the model is extended to quadrature receivers. In Section 6.3, the principle of using a frequency offset to decorrelate the desired signals from the harmonic images is presented. In addition, the sensing algorithm based on cross-correlation is explained and is formulated in terms of the quadrature mixer model from Section 6.2. In Section 6.4, the performance of the algorithm is analyzed and evaluated using simulations, while the final section offers the conclusions.

6.2 A mixer model incorporating harmonic downmixing

When a multiplying mixer's LO port is driven by a pulse-like signal, such as a digitally generated square wave, multiple frequencies present at the RF port are downconverted to baseband. In addition to the desired mixing product, additional mixing products appear at the mixer's baseband output. While the desired mixing product is governed

by the fundamental frequency of the LO signal, the other products are governed by the higher harmonics present in the LO signal. If a switching mixer is used instead of a multiplying mixer, the same argument holds as the *effective* LO waveform is pulse-like regardless of the actual LO waveform.

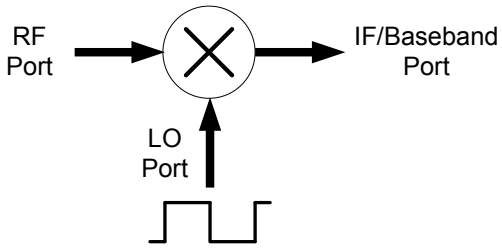

Figure 6.1: A mixer driven by a square wave at the LO port.

The mixing products found at the IF, or baseband, output of the mixer, depend on the fourier series of the effective LO waveform. Given an RF signal $x_{RF}(t)$ and an effective LO waveform $s_{LO}(t)$, the signal at the output, $y(t)$ of a mixer is given by the following equation:

$$y(t) = x_{RF}(t) \cdot s_{LO}(t) \tag{6.1}$$

The RF signal can be written as a sum of baseband-equivalent signals, where each baseband-equivalent signal represents a piece of RF spectrum centered around the harmonics of the LO waveform. In this way, each mixing product can be described separately. Given a set of band-limited baseband-equivalent signals $z_p(t)$, where $p \in [1, 2, 3, \ldots, \infty\rangle$, the RF signal is expressed as the following sum:

$$x_{RF}(t) = \Re\left\{\sum_{p=1}^{\infty} z_p(t) \cdot e^{j\cdot 2\pi\cdot p\cdot f_{LO}\cdot t}\right\} \tag{6.2}$$

,where $\Re$ denotes taking the real part of its complex argument and f_{LO} is the LO frequency in Hertz. The signal $z_p(t)$ represents a part of the RF spectrum, namely RF signals found around a frequency of $p \cdot f_{LO}$ Hz.

The $\Re$ operator may be removed by realizing that $\Re\{x\} = \frac{1}{2}(x + x^*)$, where $()^*$ denotes the complex conjugate. Therefore, (6.2) can be simplified as

$$x_{RF}(t) = \frac{1}{2}\sum_{p=1}^{\infty}\left(z_p(t) \cdot e^{j\cdot 2\pi\cdot p\cdot f_{LO}\cdot t} + z_p^*(t) \cdot e^{-j\cdot 2\pi\cdot p\cdot f_{LO}\cdot t}\right) \tag{6.3}$$

Given that the LO waveform is periodic, it is fully described by its complex-valued Fourier series coeffcients $\{c_0, c_1, \ldots, c_\infty\}$:

$$s_{LO}(t) = c_0 + \sum_{p=1}^{\infty}\left(c_p \cdot e^{j\cdot 2\pi f_{LO}\cdot p\cdot t} + c_p^* \cdot e^{-j\cdot 2\pi f_{LO}\cdot p\cdot t}\right) \tag{6.4}$$

By combining (6.3) and (6.4), an expression is obtained that shows the relation of the downmixed products to the baseband-equivalent signals $z_p(t)$ and the fourier coefficients of the mixer's LO waveform:

$$y(t) = \frac{1}{2} \sum_{p=1} \left(c_p^* \cdot z_p(t) + c_p \cdot z_p^*(t) \right) + \text{high frequency mixing products.} \tag{6.5}$$

In a direct-conversion receiver, the high frequency mixing products in (6.5) are removed by a post-mixer filter and/or the anti-aliasing lowpass filters before the A/D converters. In receiver applications, (6.5) may thus be simplified to:

$$y(t) = \frac{1}{2} \sum_{p=1} \left(c_p^* \cdot z_p(t) + c_p \cdot z_p^*(t) \right) \tag{6.6}$$

The purpose of a receiver is to recover $z_1(t)$, which is the desired signal spectrum. Note that, in the general case, $z_1(t)$ is a complex-valued signal, while $y(t)$ is real-valued. It is therefore not possible to fully recover $z_1(t)$ from $y(t)$ alone. Recovery of $z_1(t)$ is only possible by employing quadrature techniques.

6.2.1 Quadrature downconversion

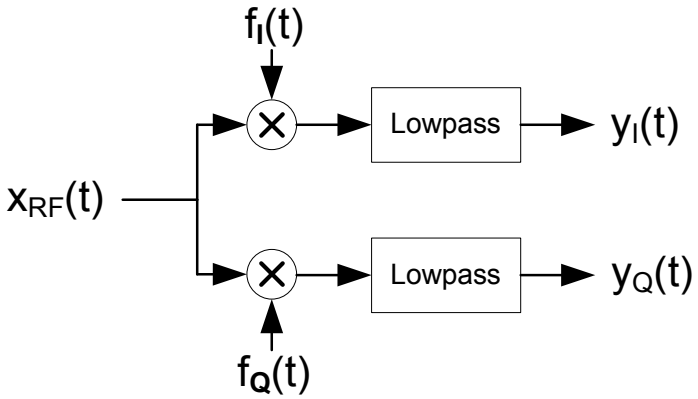

Figure 6.2: A quadrature downmixer employing two mixers. The LO signals $f_I(t)$ and $f_Q(t)$ are 90-degree out of phase with respect to each other.

A quadrature receiver uses two mixers to recover $z_1(t)$, where each mixer is driven by a different LO waveform. The two LO waveforms have the same shape but they are phase-shifted by 90 degrees with respect to each other. The phase-shift allows $z_1^*(t)$ to be removed while retaining the desired signal spectrum $z_1(t)$.

We will now apply the mixer model to a quadrature receiver architecture and show the dependence of the received signal $r(t)$, given the baseband-equivalent signals $z_p(t)$, and the fourier series coefficients of the two LO waveforms. For generality, we use different variables for the fourier coefficients of the two LO waveforms, which allows the LO waveforms to differ in shape and not only in phase.

Figure 6.2 shows the quadrature downconverter principle. Given the mixer model (6.6), the in-phase output $y_I(t)$ and the quadrature phase output $y_Q(t)$ can be written as:

$$\begin{aligned} y_I(t) &= \frac{1}{2}\sum_{p=1}\left(c_p^* \cdot z_p(t) + c_p \cdot z_p^*(t)\right) \\ y_Q(t) &= \frac{1}{2}\sum_{p=1}\left(d_p^* \cdot z_p(t) + d_p \cdot z_p^*(t)\right) \end{aligned} \tag{6.7}$$

,where c_p and d_p are the Fourier series coefficients of the LO signals $f_I(t)$ and $f_Q(t)$, respectively. The two real-valued outputs $y_I(t)$ and $y_Q(t)$ form a complex-valued baseband signal $r(t)$, where $r(t)$ may be expressed as:

$$\begin{aligned} r(t) &= y_I(t) + j \cdot y_Q(t) \\ &= \frac{1}{2}\sum_{p=1}\left((c_p - j \cdot d_p)^* \cdot z_p(t) + (c_p + j \cdot d_p) \cdot z_p^*(t)\right) \end{aligned} \tag{6.8}$$

As stated previously, the purpose of a receiver is to recover the baseband signal, or spectrum, $z_1(t)$. By examining (6.8), it is clear that this is possible when $c_1 = -j \cdot d_1$ so that $z_1^*(t)$ is removed and $c_p = 0, d_p = 0$ for any $p > 1$ so that the harmonic images are removed. Note that the conjugated terms $z_p^*(t)$ constitute interference and are caused by I/Q imbalance. We refer to them as *I/Q imbalance images*. The appendix on page 129 gives the I/Q imbalance image suppression as function of $c_p - j \cdot d_p$ and $c_p + j \cdot d_p$.

Unfortunately, the above requirements are only met when the effective LO waveform is a perfect sine wave. A mixer based on switches cannot be used as this always leads to a pulse-like effective LO waveform. In fact, only a perfect multiplying mixer driven by a perfect sine wave will achieve the conditions. Unfortunately, both are impossible to realize exactly and very difficult to approximate well in practice.

Traditionally, receivers employ bandpass filters at the RF port of the mixer to remove the harmonic image signals. Direct-conversion receivers with a wide frequency range, such as desired for cognitive radios, would require a tunable RF filter [36] or a bank of selectable bandpass filters. However, a highly-selective tunable filter with a wide tuning range is very challenging, if not impossible, to make, owing to the many tunable components that are required. In addition, the frequency response of such filters tends to deviate from the optimum shape as they are tuned across the band,

thereby reducing their selectivity. Also, a bank of selectable bandpass filters is bulky, expensive and therefore unattractive in low-cost or highly integrated systems.

Given the above, it would seem that switching mixers or pulse-like LO waveforms cannot be used effectively in direct-conversion receivers. However, analog multi-path techiques exist that employ multiple mixers in parallel to obtain an effective LO waveform that lacks certain harmonics. Therefore, certain harmonic images, most notably the 3^{rd}, 5^{th} and all even-order harmonic images, are suppressed, thereby reducing the demands on the RF filter. This technique was demonstrated by [38] for transmitters and by [24] for receivers. The multi-path technique offers a typical suppression of around 40 dB. This figure is limited by mismatches within the analog circuits. To further enhance the harmonic image suppression of the analog frontend, we have proposed a digital compensator based on blind adaptive signal processing which increases the suppression of the strongest harmonic image [35], typically by 40 dB.

As these multi-path technique does not completely remove the targeted harmonic images. There will be residual energy from the harmonic images present in the base-band signal $r(t)$. Performing spectrum sensing using $r(t)$, based on the power spectral density, leads to the detection of signals related to the harmonic images, which are false positives as they these signals do not come from the band of interest, $z_1(t)$.

In this paper we describe a method for performing spectrum sensing based on cross-correlation of two baseband signals. The method detects signals in the desired spectrum[2] based on their power spectral density while disgarding signals from the harmonic images.

6.3 Spectrum sensing based on two baseband signals

The signal detection scheme is based on obtaining two discrete-time observations of the RF spectrum. The observation signals, $r_1(n)$ and $r_2(n)$ are produced by two quadrature mixers, as shown in Fig. 6.3. The local oscillators LO1 and LO2 are tuned to f_{LO} and $f_{LO} + \Delta f$ Hz, respectively. The A/D converters use a sampling rate of F_s samples per second. Therefore, the bandwidth, W_{bb}, of each complex-valued baseband signal is equal to F_s.

Owing to harmonic downmixing, $r_1(n)$ represens multiple parts of the RF spectrum simultaneously. In addition to representing an RF part centered around f_{LO} Hz, it will also represent RF signals centered around $k \cdot f_{LO}$ Hz, where k is any positive integer. Or more precisely, $r_1(n)$ contains signals from the following parts of the RF spectrum:

[2] In normal receiver applications we wish to obtain the desired signal. In spectrum sensing, however, we wish to obtain a desired spectrum, regardless whether there is an RF signal present or not. Note that the terms refer to the same baseband-equivalent signal $z_1(t)$.

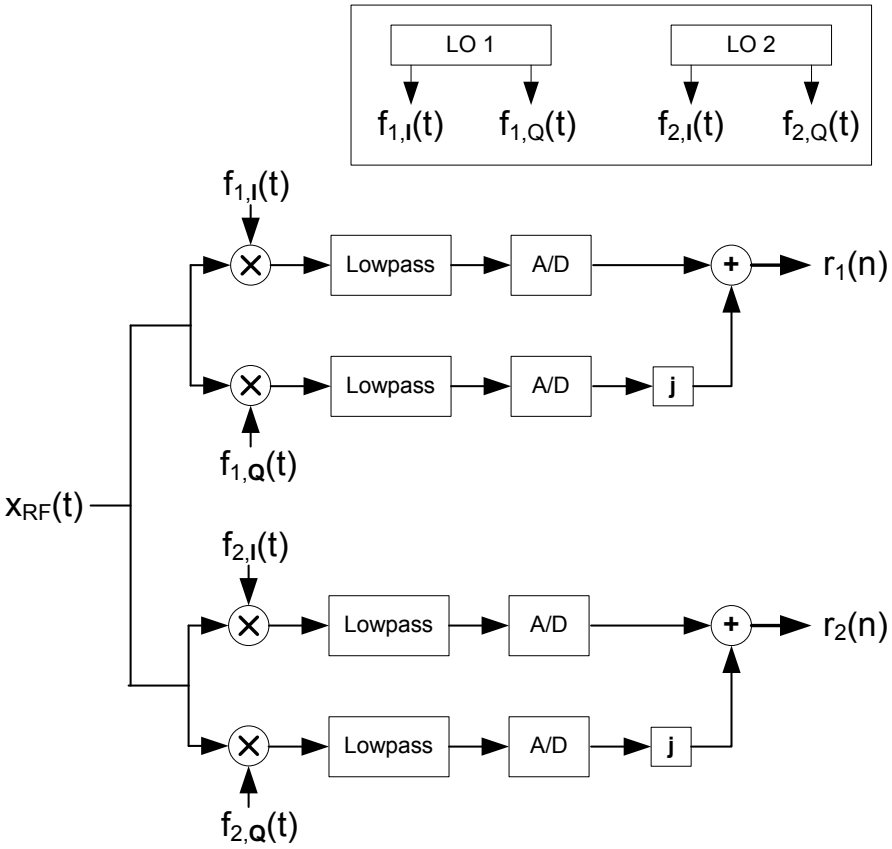

Figure 6.3: The proposed spectrum sensing frontend, which produces two discrete-time complex-valued baseband outputs $r_1(n)$ and $r_2(n)$.

$$\left\{ k \cdot f + x \;\middle|\; |x| < \frac{1}{2} W_{bb}, k \in [0, 1, 2, \ldots, \infty\rangle \right\} \tag{6.9}$$

The second baseband signal, $r_2(n)$ is generated using an LO frequency of $f_{LO} + \Delta f$ Hz, where Δf is a frequency offset. In effect, $r_2(n)$ represents a different part of the spectrum, namely:

$$\left\{ k(f + \Delta f) + x \;\middle|\; |x| < \frac{1}{2} W_{bb}, k \in [0, 1, 2, \ldots, \infty\rangle \right\} \tag{6.10}$$

By comparing (6.9) to (6.10), it can be seen that the harmonic images ($k > 1$) experience a greater frequency shift, namely $(k-1) \cdot \Delta f$ more, than the desired signal

spectrum ($k = 1$). This effect is exploited by our algorithm to discern the desired signal spectrum from the harmonic images.

By choosing Δf to be much smaller than W_{bb}, a large part of the desired signal spectrum in $r_2(n)$ overlaps with that in $r_1(n)$. The overlapping part is $W_{bb} - 2\Delta f$ Hz wide. Figure 6.4 illustrates the different shifting amounts of each harmonic image caused by the frequency offset. The desired signals, shown in black, shift by Δf, while the second harmonic image signal, shown in white, shifts by twice that amount.

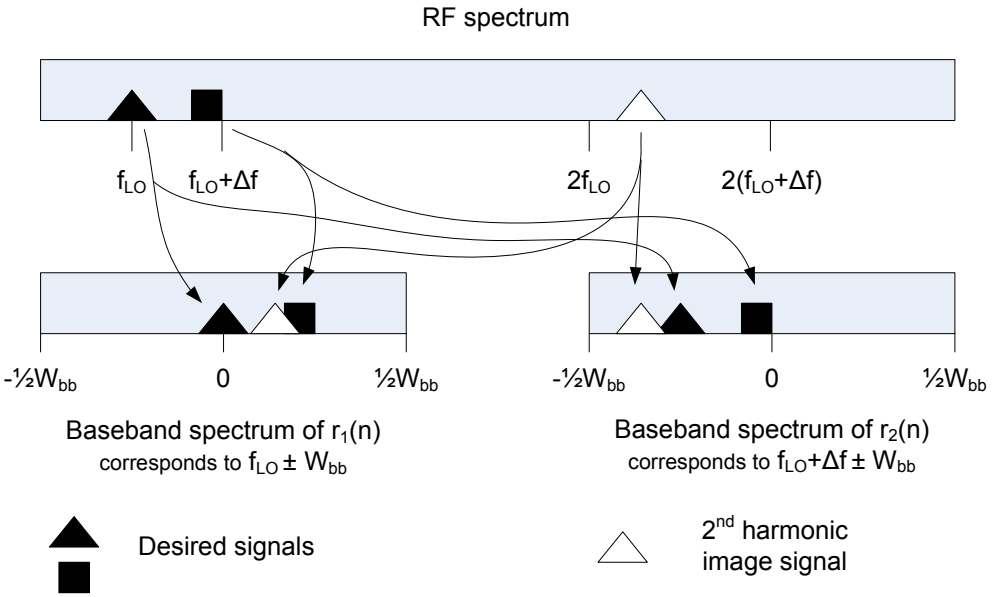

Figure 6.4: Position of $r_1(n)$ and $r_2(n)$ in the RF spectrum and their corresponding baseband spectra.

We will now restate the above in a mathematical sense.

6.3.1 Describing $r_1(n)$ and $r_2(n)$

The baseband signal $r_1(n)$ can be written as a weighted sum of the desired signal spectrum $z_1(n)$ and the harmonic images $\{z_p(n) \mid p > 1\}$:

$$r_1(n) = \sum_{p=1}^{\infty} \alpha_p \cdot z_p(n) + \beta_p \cdot z_p^*(n) \tag{6.11}$$

,where $\alpha_p = (c_p - j \cdot d_p)^*$ and $\beta_p = (c_p + j \cdot d_p)$. Furthermore, c_p and d_p are the fourier series coefficients of the quadrature mixer associated with LO1.

The second baseband signal, $r_2(n)$, can be written as a weighted sum of different baseband-equivalent signals, $\tilde{z}_p$.

$$r_2(n) = \sum_{p=1}^{\infty} \epsilon_p \cdot \tilde{z}_p(n) + \gamma_p \cdot \tilde{z}_p^*(n) \tag{6.12}$$

,where $\epsilon_p = (\tilde{c}_p - j \cdot \tilde{d}_p)^*$ and $\gamma_p = (\tilde{c}_p + j \cdot \tilde{d}_p)$. In addition, $\tilde{c}_p$ and $\tilde{d}_p$ are the fourier series coefficients of the quadrature mixer associated with LO2.

As $z_p(n)$ and $\tilde{z}_p$ must partially overlap in the RF frequency domain, $\tilde{z}_p$ is also partially defined by $z_p(n)$ and their relation can be described as follows:

$$\begin{aligned} \tilde{z}_p(n) = F_p \left\{ z_p(n) \cdot e^{-j2\pi \cdot \Delta f_d \cdot p \cdot n} \right\} \\ + \text{additional image components} \end{aligned} \tag{6.13}$$

,where $f_d = \frac{\Delta f}{F_s}$ and the $F_p\{\cdot\}$ operator filters any components that are not shared by both p^{th}-order baseband signals z_p and $\tilde{z}_p$. It is not neccessary to define the additional image components in detail, as they will not correlate with $z_p(n)$. Only their combined variance, σ^2_{add}, is of interest.

Given the signal descriptions presented above, we proceed to apply our algorithm, which is based on cross-correlation.

6.3.2 Cross-correlation based signal detection

Before applying a cross-correlation algorithm to $r_1(n)$ and $r_2(n)$, which detects the signal power of common signals in each subband, the desired spectrum within $r_2(n)$ must be frequency aligned. As shown by (6.13), the desired signal spectrum $z_1(n)$ is offset by Δf with respect to $\tilde{z}_1(n)$. By applying a frequency translation to $r_2(n)$, a frequency-aligned version, $s(n)$ is obtained:

$$\begin{aligned} s(n) = r_2(n) \cdot e^{j \cdot 2\pi \cdot f_d \cdot n} \\ + \text{additional image components} \end{aligned} \tag{6.14}$$

Note that the frequency shift caused by (6.14) is common for all signals within $r_2(n)$. Equation (6.14) can be written in terms of the baseband signals $z_p(n)$ using (6.13):

$$\begin{aligned} s(n) = \left\{ \sum_{p=1}^{\infty} \epsilon_p \cdot \tilde{z}_p(n) + \gamma_p \cdot \tilde{z}_p^*(n) \right\} \cdot e^{j \cdot 2\pi \cdot f_d \cdot n} \\ + \text{additional image components} \end{aligned} \tag{6.15}$$

,which can be further expanded to:

$$\begin{aligned} s(n) = &\left\{ \sum_{p=1}^{\infty} \epsilon_p \cdot F_p \left\{ z_p(n) \cdot e^{-j2\pi \cdot \Delta f_d \cdot p \cdot n} \right\} \right\} \cdot e^{j \cdot 2\pi \cdot f_d \cdot n} \\ &+ \left\{ \sum_{p=1}^{\infty} \gamma_p \cdot F_p \left\{ z_p^*(n) \cdot e^{j2\pi \cdot \Delta f_d \cdot p \cdot n} \right\} \right\} \cdot e^{j \cdot 2\pi \cdot f_d \cdot n} \\ &+ \text{additional image components} \end{aligned} \tag{6.16}$$

Moving the frequency translation into the sum leads to:

$$\begin{aligned} s(n) = &\sum_{p=1}^{\infty} \epsilon_p \cdot F_p \left\{ z_p(n) \cdot e^{-j2\pi \cdot \Delta f_d \cdot (p-1) \cdot n} \right\} \\ &+ \sum_{p=1}^{\infty} \gamma_p \cdot F_p \left\{ z_p^*(n) \cdot e^{j2\pi \cdot \Delta f_d \cdot (p+1) \cdot n} \right\} \end{aligned} \tag{6.17}$$

Note that for $p = 1$, (6.17) shows that $z_1(n)$ no longer has a frequency translation. However, owing to the fact that $z_1(n)$ is not represented in its entirety by $r_2(n)$ (and therefore $s(n)$), the $F_p\{\cdot\}$ operator is still needed. As stated previously, $r_2(n)$ and $r_1(n)$ overlap $W_{bb} - 2\Delta f$ Hz. Also note that the I/Q imbalance image, $z_1^*(n)$, in $s(n)$ does not align with itself in $r_1(n)$. The same holds for the harmonic images ($p > 1$).

The signals $r_1(n)$ and $s(n)$ are decomposed into subbands by a filterbank so that each subband can be cross correlated separately thereby producing frequency dependent cross-correlation information. The decomposition can be done efficiently using the Fast Fourier Transform (FFT). The FFT can be viewed as having N parallel subband channels, which share a common input $x(n)$. A single channel is shown in Fig. 6.5.

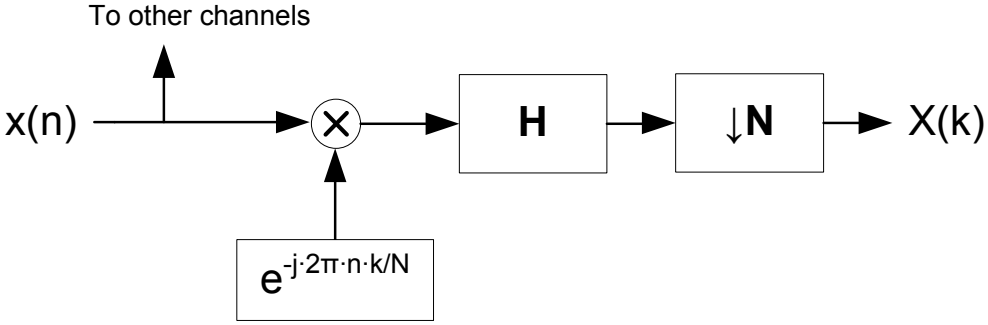

Figure 6.5: The k^{th} channel out of N channels of an N-point FFT.

Each channel consists of a complex multiplier, an N-point FIR filter H and a decimation-by-N stage. A new subband output, $X(k)$ is produced for every N input

samples of $x(n)$. The impulse response of the filter H is an N-point all-one vector, $[1, 1, 1, \ldots]$, known as a rectangular window. It is well-known that the bin-to-bin isolation of the rectangular window is poor as the first sidelobe is only 13 dB down, and that applying a non-rectangular window to the FFT input vector, $[x(n) \ldots x(n+N-1)]$ or $[y(n) \ldots y(n+N-1)]$, allows trading frequency resolution for better isolation.

As the main focus of this paper is not on filter banks, we will not go into the window design in great detail. We refer to [72] and for a thorough treatment of filter banks and [73] their application in cognitive radios.

Here, we limit ourselves to mention that we apply a Nutall window [74] given by (6.18), which has the first sidelobe at -93.3 dB. Unfortunately, it offers a frequency resolution which is four times lower. Figure 6.6 shows the spectrum of the rectangular window and the Nutall window, where the differences in mainlobe width and sidelobe level become evident.

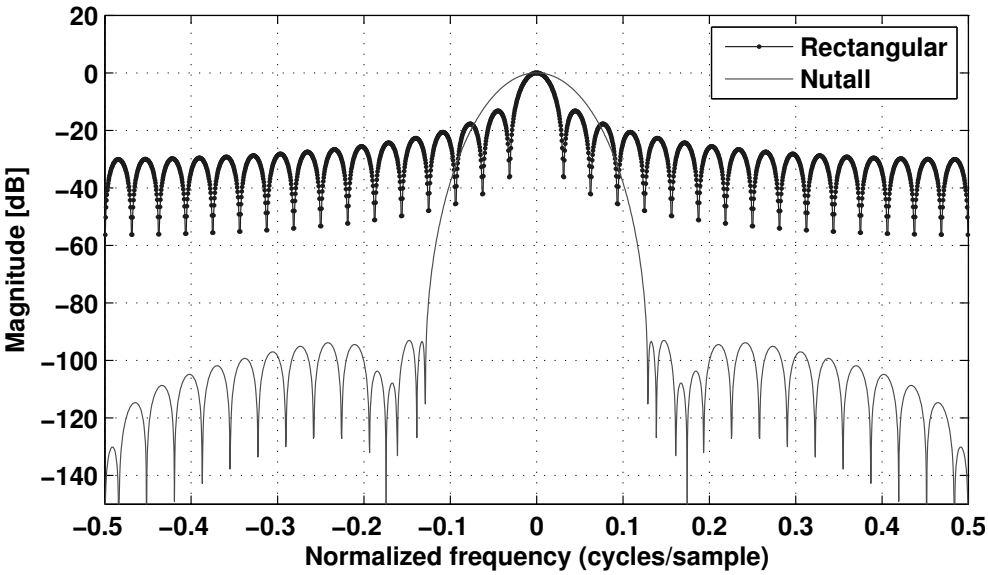

Figure 6.6: The spectrum of the rectangular window and a Nutall window, both are N=32 points long.

$$\begin{aligned} h_{nutall}(n) = a_0 &- a_1 \cdot \cos\left(\frac{2\pi \cdot n}{N-1}\right) \\ &+ a2 \cdot \cos\left(\frac{4\pi \cdot n}{N-1}\right) \\ &- a3 \cdot \cos\left(\frac{6\pi \cdot n}{N-1}\right) \\ a_0 = &0.355768 \qquad a_1 = 0.487396 \\ a_2 = &0.144232 \qquad a_3 = 0.012604 \end{aligned} \tag{6.18}$$

Given an N-point FFT and the Nutall window, each subband is approximately $\frac{8 \cdot W_{bb}}{N}$ Hz wide.

We proceed by cross correlating the k$^{\text{th}}$ subband of $r_1(n)$, which is denoted by $x_k(i)$, with the k$^{\text{th}}$ subband of $s(n)$, which is denoted by $y_k(i)$. As there are N subbands, the valid range of k is $[0, \ldots, N-1]$. Note that the sampling rate of $x_k(i)$ and $y_k(i)$ has been reduced to $\frac{F_s}{N}$ because of the decimation-by-N of the FFT, hence the need for the new time index, i.

The zero-lag cross-correlation of the complex signals x_k and y_k is defined as:

$$R_{x_k,y_k} = E\{x_k \cdot y_k^*\} \tag{6.19}$$

The cross-correlation can be estimated based on a limited number of samples of x_k and y_k. Given N samples of x_k and y_k, the following equation is used to obtain an unbiased estimate $\widehat{R_{x_k,y_k}}$ of R_{x_k,y_k}:

$$\widehat{R_{x_k,y_k}} = \frac{1}{N} \sum_{i=0}^{N-1} x_k(i) \cdot y_k(i)^* \tag{6.20}$$

See page 129 for proof relating to the unbiasedness of the estimator.

Let x_k denote the signals in the k$^{\text{th}}$ subband of r_1, y_k denote the signals in the k$^{\text{th}}$ subband of r_1, and let $z_{p,k}$ be the signals in the k$^{\text{th}}$ subband of the p$^{\text{th}}$ harmonic image. By choosing Δf to be a multiple of the subband spacing, $\frac{W_{bb}}{N}$, we can write

$$x_k(i) = \sum_{p=1}^{\infty} \alpha_p \cdot z_{p,k}(i \cdot N) + \beta_p \cdot z_{p,N-k-1}^*(i \cdot N) \tag{6.21}$$

and

$$\begin{aligned} y_k(i) = &\sum_{p=1}^{\infty} \epsilon_p \cdot F_p\left\{z_{p,k+(p-1)\cdot o}(i \cdot N)\right\} \\ &+ \sum_{p=1}^{\infty} \gamma_p \cdot F_p\left\{z_{p,N-k-1-(p+1)\cdot o}^*(i \cdot N)\right\} \\ &+ \text{additional image components} \end{aligned} \tag{6.22}$$

,where o is Δf expressed in the number of subband channels:

$$o = \frac{N \cdot \Delta f}{W_{bb}} \tag{6.23}$$

Note that the subband index can go below zero or above $N-1$ in (6.22). In that case, the baseband-equivalent signal is outside the baseband bandwidth and is equal to zero.

Assuming that the baseband signals $z_{p,k}$ are wide-sense stationary, the cross-correlation expression for each subband (6.20) can be written as:

$$\begin{aligned} R_{x_k,y_k} &= E\{x_k(i) \cdot y_k(i)^*\} \\ &= \alpha_p \cdot \epsilon_p^* \cdot |z_{p,k}|^2 \end{aligned} \tag{6.24}$$

The assumptions made in (6.24) are that subband signals $z_{p,k}$ and $z_{p,k+(p-1)*o}$ do not correlate unless $p = 1$ and that $z_{p,N-k-1}$ and $z^*_{p,N-k-1-(p+1)*o}$ never correlate, regardless of p. The assumptions will hold true if Δf is large enough that the subbands are independent, i.e. larger than the inter-channel spacing of the wireless standards being monitored. Whether this offset can be reduced to smaller values is a topic for further research.[3]

Note that the correlation (6.24) depends on ϵ_p and α_p, which are related to the mixers in the frontend. This fact can be used as a way to perform system identification of the mixers, which may be useful for calibration purposes. Also consider that changing the frequency shift, f_d, in (6.14) allows a different harmonic image to be selected instead of $z_1(n)$. The correlation (6.24) will provide information on the power of that harmonic image. Such information is useful in adaptive harmonic rejection schemes, such as [35].

After obtaining an estimate of the cross-correlation (6.24) for each subband using the estimator (6.20), the results are thresholded to decide whether the subband can be considered occupied or empty. The integration time given by the number of samples, M, should be chosen large.

A block diagram of the entire algorithm is given in Fig. 6.7. The time it takes the algorithm to produce an occupancy vector is equal to $\frac{N \cdot M}{F_s}$ seconds.

6.3.3 Implementation aspects

The algorithm from Fig. 6.7 need not be implemented as shown. For instance, when the LO offset Δf is chosen to be an integer multiple of the subband spacing of the FFT, then the downmixing action performed on $r_2(n)$ can be achieved by shifting the elements in the vector y_p.

[3]Consider that an OFDM signal consists of multiple carriers, of which most can be considered independently modulated. In such a case, a frequency offset smaller than the OFDM channel spacing will not result in significant correlation.

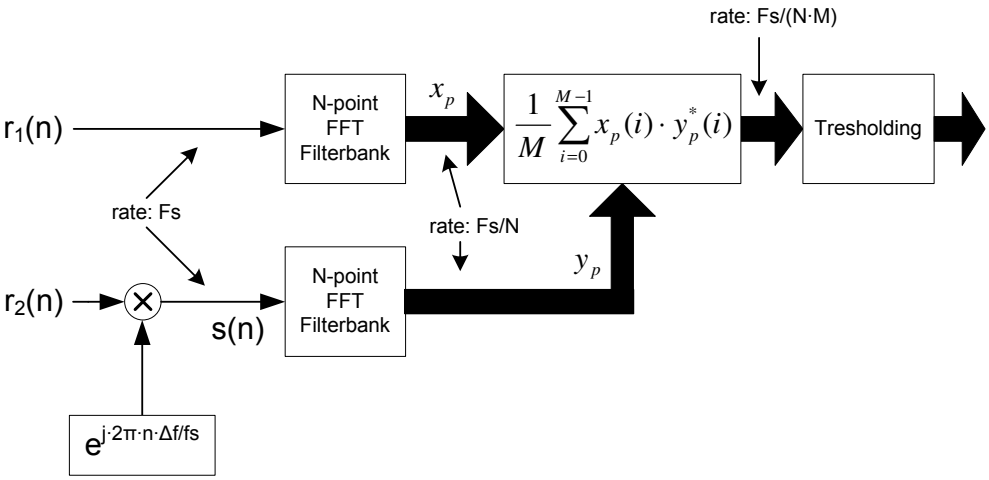

Figure 6.7: A block diagram of the baseband processing algorithm.

A further reduction in complexity is achieved by realizing that only the overlapping part of $r_1(n)$ and $r_2(n)$ provides correlative information about the desired signal spectrum. Therefore, not all elements from x_p and y_p need be taken into account when performing the cross-correlation. In effect, the number of correlators can be reduced from N to $N_{corr} = \left\lceil N\frac{W_{bb}-2\Delta f}{W_{bb}} \right\rceil$, where $\lceil\cdot\rceil$ denotes a ceiling operation.

A radix-2 FFT requires $2N \cdot \log_2(N)$ real multiplies and $3N \cdot \log_2(N)$ real adds. In addition to the FFT, a window must be applied. The windowing operation consists of $2N$ real multiplies. There are two FFTs and therefore two window operations necessary, bringing the count to $4N \cdot \log_2(N) + 4N$ multiplies and $6N \cdot \log_2(N)$ real additions. Each correlator performs one complex multiply, one complex add and a conjugation for each new x_p (or y_p) vector. The conjugation of y_p can be performed by the complex multiply. Therefore, a correlator equates to 4 real multiplies and 4 real adds. There are N_{corr} correlators, so the total complexity becomes $4N \cdot \log_2(N) + 4N_{corr} + 4N$ multiplies and $6N \cdot \log_2(N) + 4N_{corr}$ adds which must be performed $\frac{F_s}{N}$ times a second.

Figure 6.8 shows the total number of operations and the number of operations per sample as a function of the number of subbands, N. The number of correlators N_{corr} was chosen equal to N. The lower graphs shows that the number of operations per sample does not become prohibitively large for a large number of subbands. For every doubling of the number of subbands, the number of multiplies grows by four and the number of additions grows by 6. The increase is solely due to the FFT.

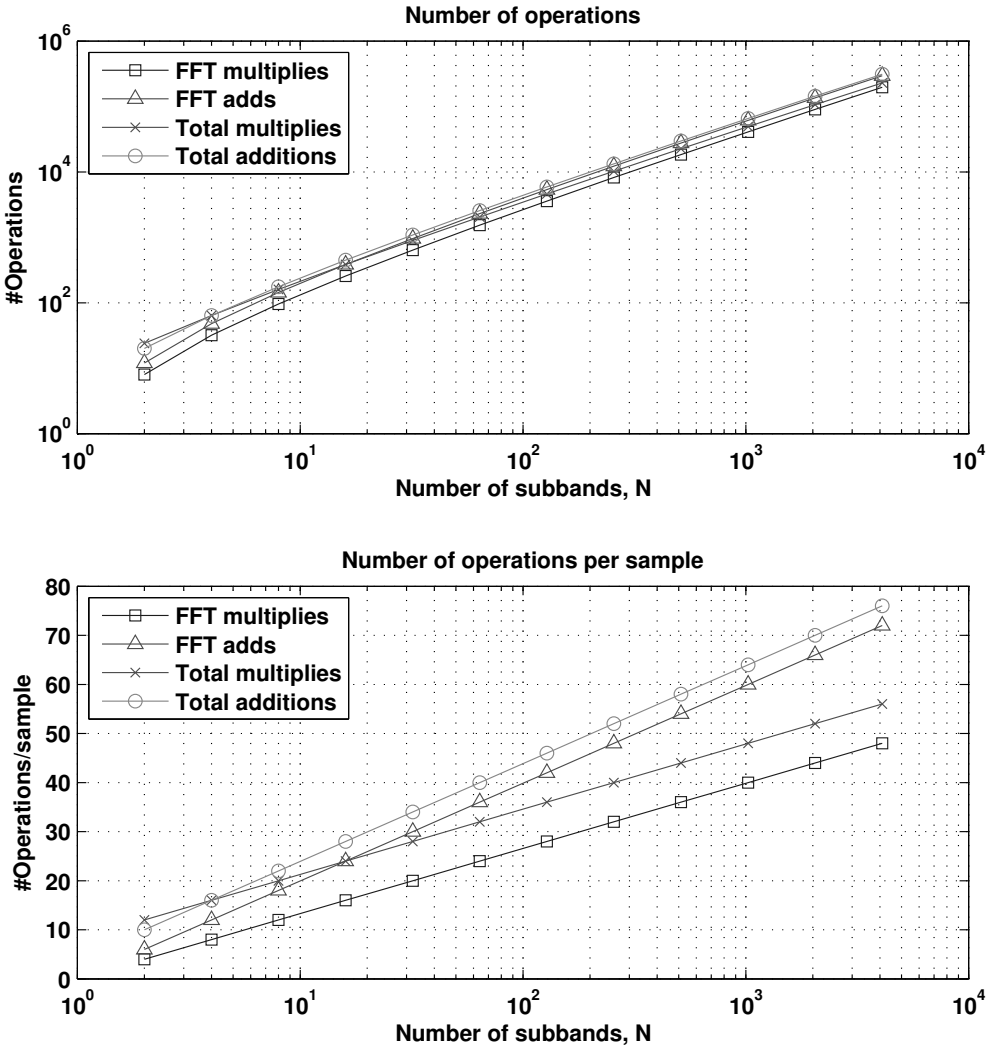

Figure 6.8: Algorithmic complexity as a function of the number of subbands, N. The number of correlators, N_{corr}, is equal to N.

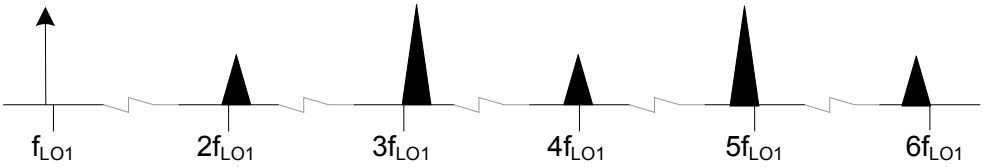

Figure 6.9: Graphical representation of the RF signals and their frequencies as given by Table 6.1.

6.4 Simulations

We performed simulations to demonstrate the effectiveness of the detection algorithm. The aim is to compare a traditional detector based on the power spectral density with our detection algorithm. The baseband-equivalent mixer model (6.11) was used to generate the baseband signals $r_1(n)$ and $r_2(n)$. The α_p and β_p coefficients were chosen to represent a switching mixer with a 50% duty cycle square wave:

$$\alpha_p = \begin{cases} 0 & \text{if } p \text{ is even,} \\ \frac{1}{p} & \text{if } p \text{ is odd} \end{cases} \tag{6.25}$$

$$\beta_p = 0 \tag{6.26}$$

The fact that $\beta_p = 0$ means that there is no I/Q imbalance.

The desired signal is a sinusoid and the harmonic image signals are all 64-QAM modulated using a random bitstreams. The 64-QAM signals occupy 1/16 of the baseband bandwidth. Their stength (standard deviation σ) and frequency are shown in Table 6.1 and Fig. 6.9. The signals were deliberately placed so that they overlap after downmixing. Futhermore, two of the image signals are 34 dB stronger (at the antenna) than the desired signal.

harmonic	frequency [cycles/sample]	strength [σ]
1	-0.015	1
2	0.01	1
3	0.02	50
4	-0.005	1
5	-0.015	50
6	0.025	1

Table 6.1: Frequency and strength of simulated signals

The number of subbands was set to $N = 1024$. Taking the spectral spreading of the Nutall window into account, this leads to a resolution of $1024/8 = 128$ distinct frequency bins. The frequency offset was set to $d_f = \frac{60}{1024}$, which equates to a distance of 60 FFT bins.

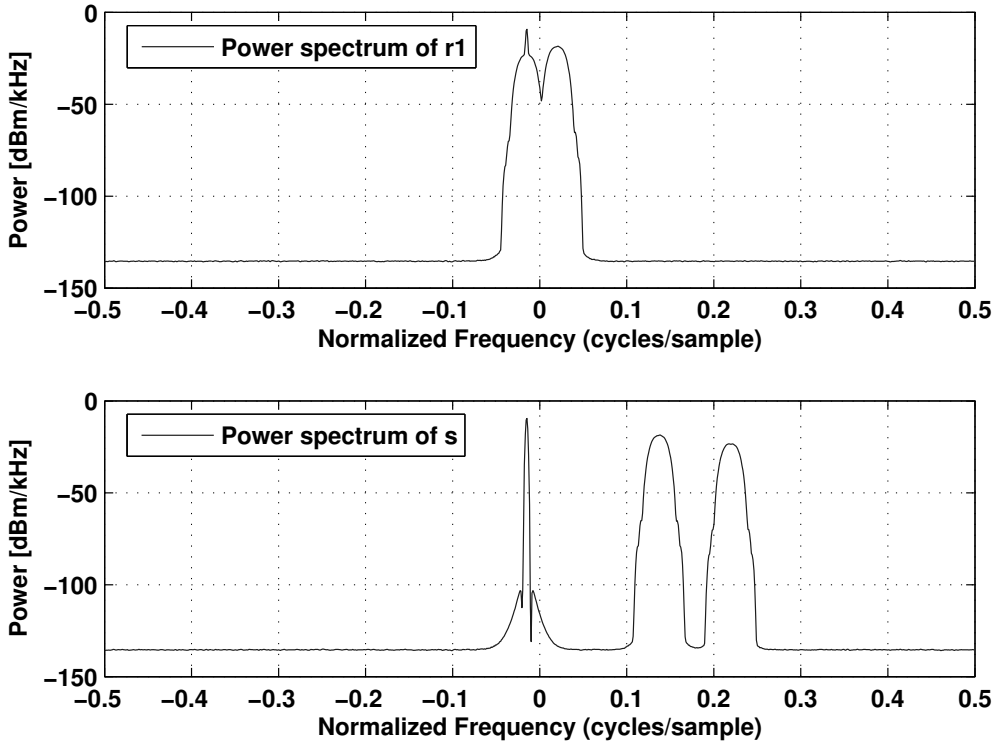

Figure 6.10: The power spectral density of $r_1(n)$ and $s(n)$. The quadrature downmixers do not suffer from I/Q imbalance.

Figure 6.10 shows the power spectral density (PSD) of $r_1(n)$ and $r_2(n)$. The PSD of $r_1(n)$ shows that almost all harmonic images are on top of each other and that the sinusoidal desired signal can be seen peaking just above them. In the baseband signal, $s(n)$, it is clear that the different harmonic images undergo different frequency shifts compared to $r_1(n)$. However, the desired signal undergoes no frequency shift. A detector based on the PSD will detect the presence of the harmonic images, as can be seen from Fig.6.10. Therefore, it is not suited for spectrum sensing, when harmonic images are present.

Our detector should be able to distinguish the harmonic images from the desired signal. That this is indeed the case, is shown by Fig. 6.11, which gives the power spectrum based on the cross-correlation for correlation length M=1,64 and 1024. As a reference, the PSD of $r_1(n)$ is also plotted.

Figure 6.12 is a zoomed in version of Fig. 6.11 which shows the spectrum around the sinusoidal signal present in the desired spectrum. The PSD curve shows that harmonic images are being detected, as the PSD response is only 9.3 dB (at 0.02 cycles/sample) below that of the sinusoid. Examining the cross-correlation curves

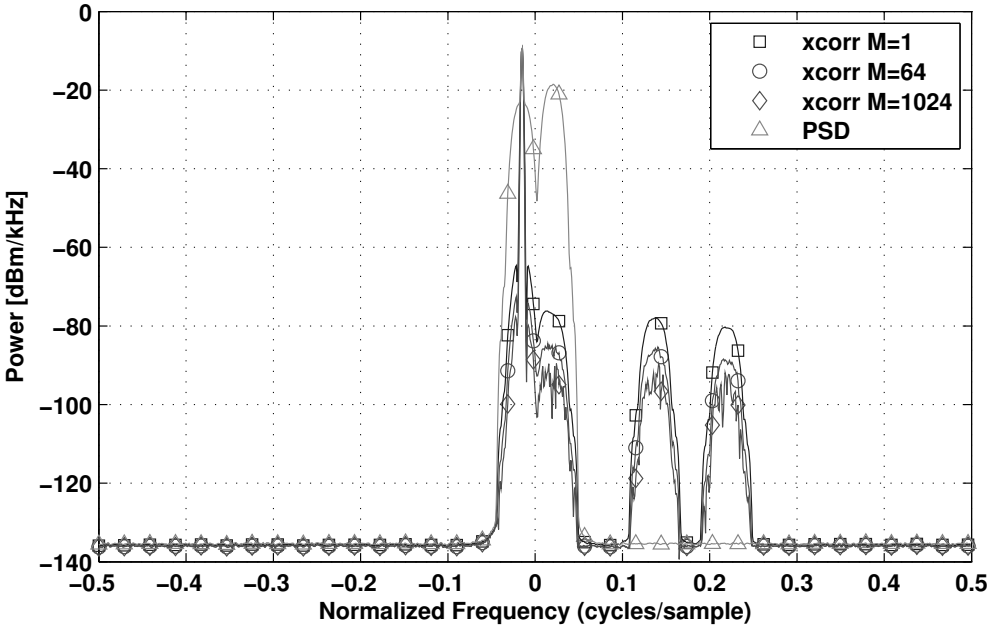

Figure 6.11: Power spectral density of $r_1(n)$ and the cross-correlation vectors for M=1,16 and 1024. The quadrature downmixers do not suffer from I/Q imbalance.

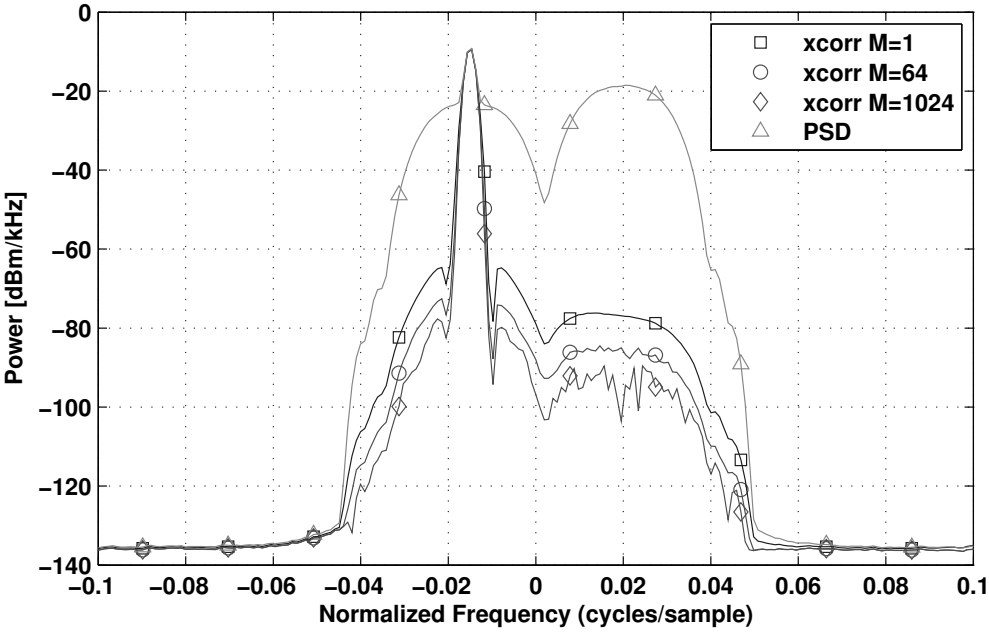

Figure 6.12: A zoomed in version of Fig. 6.11. The quadrature downmixers do not suffer from I/Q imbalance.

shows that the harmonic images have been rejected by more than 61.5 dB for $M = 1$ to more than 80 dB for $M = 1024$ at 0.02 cycles/sample. Note that the large rejection for $M = 1$ dB is owing to the fact that there is no signal present at 0.02 cycles/sample in $s(n)$.

The harmonic images are suppressed by 61.5 dB for $M = 1$ and every 1000-fold increase of M will add 15 dB of suppression. As the averaging is done in the power domain, not the amplitude domain, we cannot expect more. Given enough samples, the non-correlating peaks will disappear in the noise and our cross-correlation algorithm will be able to separate the harmonic images from the desired spectrum. However, this may take an unrealistic number of samples.

The previous simulation did not take into account the fact that imperfections in the analog frontend, such as an amplitude or phase mismatch between the I and Q paths of r_1 or r_2, cause I/Q imbalance. When I/Q imbalance is present, the complex conjugated terms in (6.21) and (6.22) come into play. We performed the above simulations again, this time with $\beta_p = 0.01 \cdot e^{j \cdot 2\pi \cdot \phi}$, where the phase angle ϕ was arbitrarily chosen to equal 0.1. The I/Q imbalance image rejection of this quadrature downmixer is 40 dB.

The I/Q imbalance images can clearly be seen in the PSD plot of $s(n)$, see Fig. 6.13. However, the I/Q imbalance images in $r(n)$ are disguised by the harmonic images and the desired signal. By comparing Fig. 6.10 to Fig. 6.13, the rejection of the harmonic images remains the same. This is easily explained as the I/Q imbalance images manifest themselves in subbands different from the harmonic images. Therefore, they are not seen by the same correlators. The I/Q imbalance images experience the same rejection of 15 dB per 1000-fold increase in the number of correlator samples, M.

While the number of correlation samples, M, needed to fully reject the harmonic images may prove prohibitively large, our method may still be useful. Consider the fact that if the PSD, which is obtainable from fewer samples, indicates no signal presence in a frequency bin, the cross-correlation information of that bin can be disgarded. However, when the PSD indicates the presence of a signal in a bin, the signal's origin must be checked. To check the origin of the signal, we can compare two cross-correlation vectors. One obtained using $M = 64$ and averaged in magnitude 16 times and the other obtained using $M = 1024$. If the power in the bin reduces by approximately $10 \cdot \log_{10}(\frac{1024}{64}) = 6$ dB, it must be occupied by a harmonic image. If the attenuation is less, there is correlative energy and a signal from the desired spectrum is also present. Whether this solution is feasible, is a topic for further investigation.

Another way to make use of our cross-correlation method, is to apply a multi-path harmonic-rejection mixer [24], which offers about 40 dB of harmonic image rejection without the use of an RF filter. As the harmonic images are already rejected by a fair amount, the cross-correlation algorithm need not provide as much rejection as without a harmonic-rejection mixer. A rejection of 40 dB reduces the required number of correlation samples by a factor of 10^8, which is an extremely large reduction. Note that 40 dB is still not enough as harmonic images can be more than 100 dB above

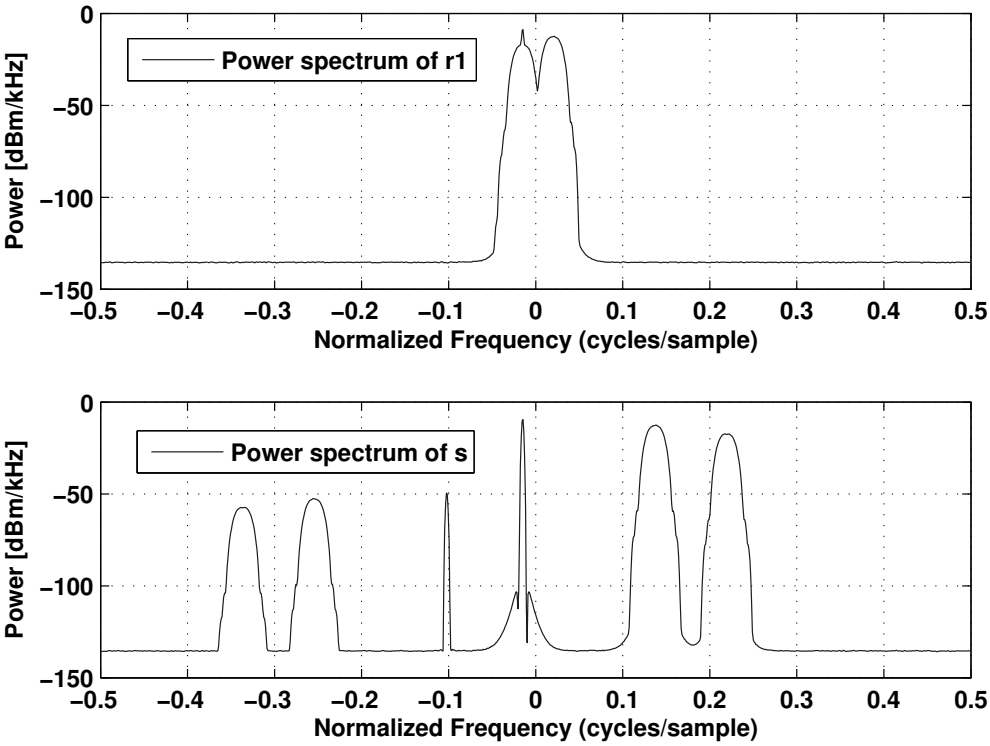

Figure 6.13: The power spectral density of $r_1(n)$ and $s(n)$. The quadrature downmixers have I/Q imbalance. The I/Q imbalance image rejection is 40 dB.

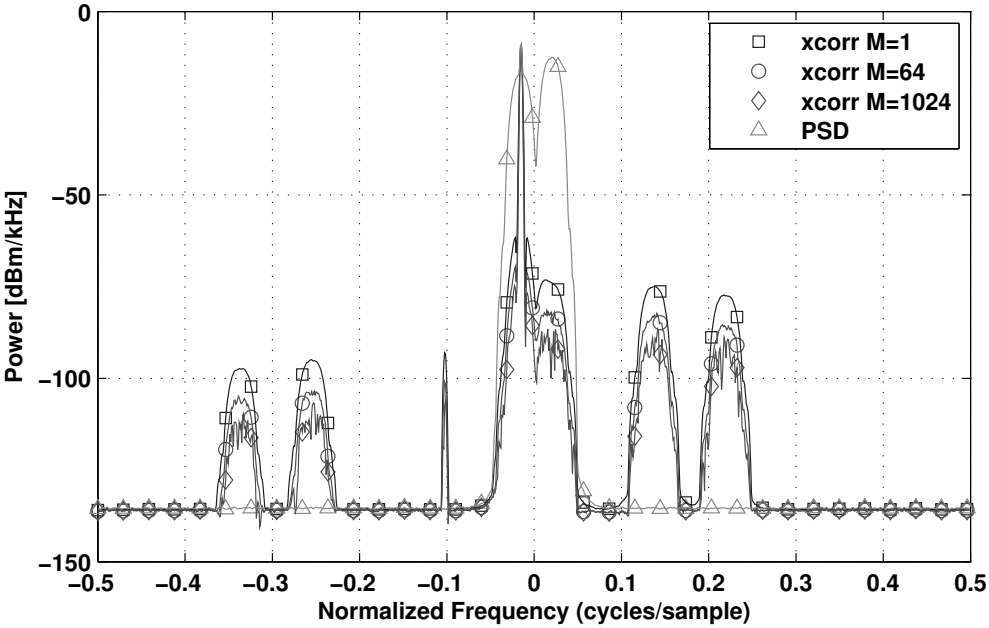

Figure 6.14: Power spectral density of $r_1(n)$ and the cross-correlation vectors for M=1,16 and 1024. The quadrature downmixers have I/Q imbalance. The I/Q imbalance image rejection is 40 dB.

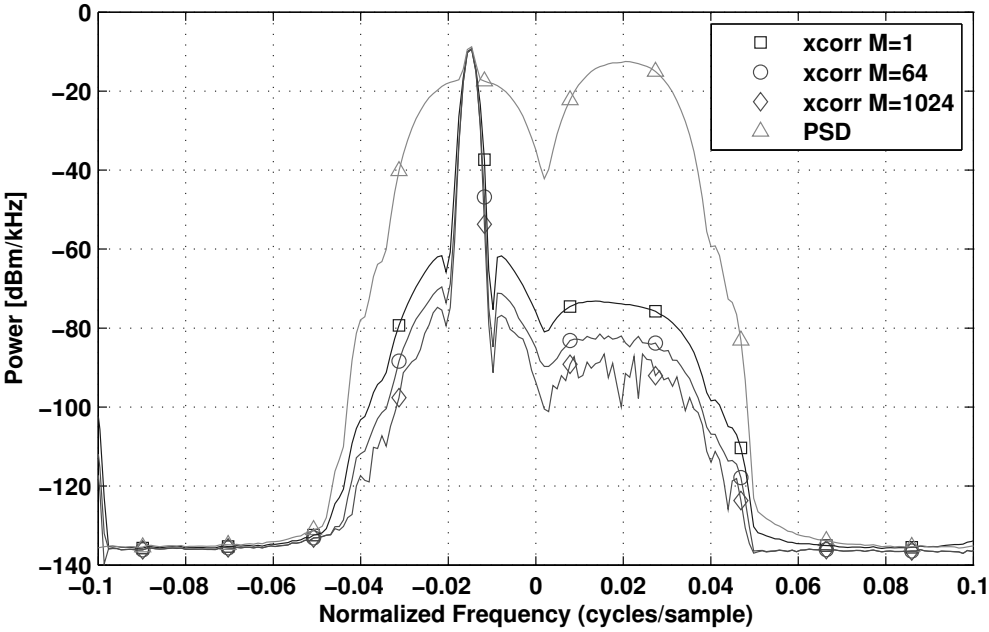

Figure 6.15: A zoomed in version of Fig. 6.14. The quadrature downmixers have I/Q imbalance. The I/Q imbalance image rejection is 40 dB.

the noise floor.

In addition to rejecting the harmonic images, the cross-correlation method will also reject spurious signals that find their way into r_1 and r_2. These spurious signals can come from other parts of the receiver circuitry, such as the frequency synthesizer, the clock generators and the digital baseband processor. Spurious signals can also enter the receiver circuity from the power supply terminals of the IC. The rejection occurs because the digital-domain frequency translation will decorrelate them.

6.5 Conclusions

We have introduced the important problem of harmonic downmixing in the context of normal receiver operation and spectrum sensing applications, such as cognitive radios. Harmonic downmixing is the result of harmonics in the effective LO waveform, which cause RF signals found at multiples of the LO's fundamental frequency to be downconverted to baseband.

In cognitive radio, power spectral density (PSD) measurements are used to perform spectrum sensing. However, given the presence of harmonic images in the baseband signal of the sensing receiver, a PSD-based algorithm will mistakenly identify the frequency as occupied. In this paper we presented an algorithm based on cross-correlation, which is able to reject the harmonic images making correct occupancy identification possible.

The algorithm uses two baseband observations, $r_1(n)$ and $r_2(n)$, which are generated by two quadrature mixers. The LO frequencies of the mixers are offset by Δf Hz. Because of this, the harmonic images undergo different frequency shifts with respect to the desired signal spectrum and each other. This causes a decorrelation of the harmonic images, while the desired signal spectrum remains correlated. A subband cross-correlator is used to identify which frequency bins are occupied by a signal within the desired spectrum.

The complexity of the algorithm was analyzed. A 1024-band measurement needs 48 real multiplications and 64 real additions per sample. At positions where the harmonic images are present and detected by the PSD method, the cross-correlation method is able to reject these signals by more than 80 dB. This figure is not affected by I/Q imbalance.

In addition to rejecting the harmonic images, any spurious signals entering the receiver through the analog baseband inputs will also be rejected.

Acknowledgments

The authors would like to thank Zhiyu Ru and Mark Oude Alink for the many fruitful discussions.

Appendix: Proof of the unbiasedness of the cross-correlation estimator

We will show that the estimator (6.20) is unbiased when x and y are jointly wide-sense stationary. To prove this, we must show that the expected value of the estimate $\widehat{R_{xy}}$ is equal to R_{xy}.

We begin by writing out the expectation of the estimator:

$$E\{\widehat{R_{xy}}\} = E\left\{\frac{1}{N}\sum_{n=0}^{N-1} x(n)\cdot y(n)^*\right\} \tag{6.27}$$

We proceed by moving the expectation operator into the sum:

$$E\{\widehat{R_{xy}}\} = \frac{1}{N}\sum_{n=0}^{N-1} E\{x(n)\cdot y(n)^*\} \tag{6.28}$$

As the expectation of the terms $E\{x(n)\cdot y(n)^*\}$ are all equal to R_{xy} when x and y are jointly wide-sense stationary, we may simplify the above to:

$$E\{\widehat{R_{xy}}\} = \frac{1}{N}\sum_{n=0}^{N-1} R_{xy}, \tag{6.29}$$

which can be reduced to:

$$E\{\widehat{R_{xy}}\} = R_{xy} \tag{6.30}$$

Hence, the estimator (6.20) is unbiased.

Appendix: I/Q Imbalance and Harmonic Rejection parameters

The relation between the complex-valued baseband output, the baseband-equivalent signals $z_p(t)$ and the fourier coefficients of the quadrature LO waveforms, $\{c_0, c_1, \ldots, c_\infty\}$ and $\{d_0, d_1, \ldots, d_\infty\}$, see (6.8), may be restated as:

$$r(t) = \frac{1}{2}\sum_{p=1}\left(\alpha_p\cdot z_p(t) + \beta_p\cdot z_p^*(t)\right), \tag{6.31}$$

where $\alpha_p = (c_p - j\cdot d_p)^*$ and $\beta_p = (c_p + j\cdot d_p)$.

The magnitudes $|\beta_p|$ and $|\alpha_p|$ give the amount of harmonic image suppression. The suppression of the p$^{\text{th}}$ harmonic image with respect to the desired spectrum can be defined as

$$L_{harmonic,p} = \frac{|\alpha_1|^2}{|\alpha_p|^2}, \tag{6.32}$$

or in decibels:

$$L_{harmonic,p} = 10 \cdot \log_{10}\left(\frac{|\alpha_1|^2}{|\alpha_p|^2}\right) \quad \text{dB} \tag{6.33}$$

Each harmonic image has an associated I/Q imbalance image, owing to I/Q imbalance in the receiver. The I/Q imbalance image suppression of the p^{th} harmonic image is defined as

$$L_{quad,p} = \frac{|\alpha_p|^2}{|\beta_p|^2} \tag{6.34}$$

In decibel it is given by (6.35).

$$L_{quad,p} = 10 \cdot \log_{10}\left(\frac{|\alpha_p|^2}{|\beta_p|^2}\right) \quad \text{dB} \tag{6.35}$$

This is an extension of the formulation of L_{quad} given by [32].

Chapter 7

Summary and Conclusions

This final chapter summarizes the work described in Chapters 2 through 6 in Section 7.1. Section 7.3 lists the original contributions. Then, Section 7.4 gives suggestions for future work.

7.1 Summary

Switch-based mixers have a linearity advantage over other types of mixers and are relatively easy to implement in digitally oriented CMOS IC technology. However, the harmonically rich local oscillator signals of switch-based mixers cause multiple (harmonically related) RF signals to be down-mixed to baseband in addition to the desired signal, causing harmonic down-mixing interference.

The harmonically related RF signals, also termed *harmonic images*, can comprise more than 0 dBm of interference power, requiring harmonic rejection figures in excess of 100 dB in order to suppress the interference to below the noise floor. This shows the extent of the harmonic down-mixing problem.

In narrow-band receivers, harmonic down-mixing interference is avoided by placing an off-chip RF filter before the mixer. However, wide-band receivers such as the single-chip software-defined radios targeted by this work would require many such RF filters, which is not advantageous in terms of cost and system size.

The number of RF filters can be reduced by employing switch-based harmonic rejection mixers. These mixers typically attenuate the harmonic down-mixing interference of the third and fifth harmonic images[1] by 30 to 40 dB without using RF filters. The attenuation is limited by mismatches within the analog circuitry. Thus, additional attenuation is required.

[1] This requires and eight-phase harmonic rejection mixer.

This thesis focuses on the development of signal processing algorithms that remove, compensate or reduce sensitivity to harmonic down-mixing interference. The algorithms envisioned are blind in the sense that they do not use features such as modulation format, pilot tones, or training sequences of the desired or interference signals to achieve their goal. Digitally assisted calibration techniques of the analog front-end are not considered as they complicate system integration. Where needed, adaptive algorithms are used to better cope with (unknown) mismatches, which normally limit the overall harmonic rejection performance of the receiver.

The harmonic down-mixing phenomenon is introduced more formally in Chapter 3: the received signal is formulated as a weighted baseband-equivalent mixture of the desired signal and the harmonic images. The weights are derived from the Fourier series coefficients of the effective local oscillator (LO) waveform. Thus, this model ties together the shape of the effective LO waveform and the achievable harmonic rejection offered by the harmonic rejection mixer. By modelling mismatches as slight deviations in the effective LO waveform, their effect on the harmonic rejection can be analyzed.

Adaptive interference cancelling (AIC) in the digital domain can be used to increase the harmonic rejection in a front-end employing switch-based harmonic rejection mixers, see Chapter 3. This method does not require any knowledge of the mismatches in the analog front-end, neither does it require knowledge about the received signal nor the interference. The AIC technique subtracts an estimate of the harmonic image interference $v(n)$ from the received signal $r(n)$, thereby reducing the interference to the desired signal. Before subtraction, the interference estimate is treated by a two-coefficient adaptive filter to equalize the estimate with the interference in the received signal. This way, (unkown) amplitude or phase mismatches are greatly reduced, thereby increasing the rejection of the interference. It can be shown that the rejection of the interference is only dependent on the interference-to-signal ratio of the interference estimate and the adaptive step size parameter μ.

The required interference estimate signal $v(n)$ is generated from two complex-valued baseband signals ($IQ_1(n)$ and $IQ_2(n)$) which have a 45-degree phase relation pertaining to the desired signal. The third and fifth order harmonic images undergo a phase rotation of 135 and 225 degrees respectively. After converting the baseband signals to the digital domain using four ADCs, two for each complex baseband signal, a reverse 45 degree rotation to the second baseband signal is applied. Subtracting it from the first cancels the desired signal but leaves the third and fifth order harmonic images. Again, owing to phase and amplitude mismatches, the cancelling of the desired signal is not perfect. Thus, under strong interference conditions and good desired signal rejection, the interference estimate contains mostly energy from the third and fifth order harmonic image bands.

A simple two-coefficient adaptive filter is used to equalize (in phase and amplitude) the interference estimate $v(n)$ with the interference in the received signal. The adaptive filter uses the Least Mean Squares (LMS) algorithm [25] to obtain its filter coefficients by minimizing the interference contribution at the output of the canceller. The

optimal filter coefficients for the third and fifth harmonic image bands differ owing a different phase relationship between the interference estimate $v(n)$ and received signal $r(n)$. Given that the canceler aims to minimize the interference power at its output, the canceller will mostly reject the image band containing the strongest interference. As with any LMS-based adaptive interference cancelling scheme, the effectiveness is determined by the interference-to-signal ratio of the generated interference estimate signal.

When there is hardly harmonic image interference, the interference estimate will contain a relatively large amount of desired signal energy. In this case the interference estimate is of poor quality and the canceller must be disabled in order to avoid cancelling the desired signal. When the power of the interference estimate is smaller than the received signal, the system is operating in this unfavorable regime.

When implemented using fully differential circuitry, harmonic rejection mixers have good even order rejection, often in excess of 60 dB. Assuming that a strong interferer only exists in one of the two targeted odd-order image bands, the first problematic harmonic image band is of the seventh order. This and higher bands must still be filtered out using a pre-mixer RF filter. The requirements on this filter are very relaxed compared to those required by a wideband receiver without enhanced harmonic rejection mixers.

The adaptive interference cancelling scheme was tried out in practice using two different analog front-ends.

The first front-end was developed from off-the-shelf ICs by the author and is described in Chapter 4. It is a frequency scaled experiment to show the feasibility of the AIC based cancelling technique. Using this front-end up to 75 dB of total harmonic rejection was measured, with 35 dB attributed to the mixer and up to 40 dB to the digital harmonic rejection technique.

The second front-end was developed by Dr. Z. Ru [75] in a 65-nm IC process and contains a fully integrated multi-phase harmonic rejection mixer stage with accompanying baseband amplification. This architecture is described in Chapter 5. By design, the harmonic rejection of the analog front-end is limited to approximately 36 dB by using a $2 : 3 : 2$ weighting scheme instead of a $1 : \sqrt{2} : 1$ scheme. The former ratio allows a unit element implementation approach, which is less sensitive to process spread and leads to tighter amplitude and phase matching between the four baseband signals. The adaptive interference canceller is able to increase the third or fifth harmonic image rejection from 36 dB to over 80 dB when a single harmonic image band is dominating; an increase of 44 dB. These figures were measured with a -66.1 dBm desired signal, a -20.1 dBm harmonic image and using 10 randomly selected chips.

In addition to regular receiving applications, harmonic image interference is also undesirable in spectrum sensing applications. Among other things, spectrum sensing is used to discover unused parts of the radio spectrum, termed *white spaces*. Because usable unallocated radio spectrum is becoming more and more scarce, opportunistic exploitation of white spaces is an active research area.

Harmonic down-mixing interference causes classic energy-based white space detectors to classify unoccupied parts of the spectrum as occupied. To reduce the sensitivity to the detection of harmonic image interference, a receiver architecture consisting of two parallel quadrature down-converters is proposed, see Chapter 6. The quadrature down-converters employs harmonic rejection mixers, which typically give 30 to 40 dB of rejection to the third and fifth harmonic images.

Of the two down-converters, the second down-converter has a frequency offset of Δf with respect to the first. This causes the desired signal band to be shifted by Δf. The harmonic image bands, however, are moved by a factor equal to $n \cdot \Delta f$, where n is the harmonic number. In the digital domain, the baseband signal of the second down-converter is shifted back by $-\Delta f$ by a digital oscillator and multiplier. This frequency shift affects the desired image band and the harmonic images equally. Thus, between the first and second (processed) baseband signals, only the desired signal band is frequency aligned.

Cross-correlation of the two baseband signals is used to detect the presence of energy in the desired signal band. The unaligned harmonic image bands do not affect the cross-correlation. Before cross-correlating, a filter bank is used to divide the baseband signals into subbands to increase the frequency resolution of the algorithm.

Simulations show the approach works in theory and an analysis of the complexity is given. The suppression of the harmonic image energy depends on the integration time of the cross-correlator. Per 1000-fold increase of the number of samples, the rejection is increased by 15 dB.

7.2 Conclusions

This work started on the premise that (adaptive) digital signal processing can be used to reduce interference problems in analog front-ends that suffer from harmonic down-mixing. Two approaches of dealing with harmonic image interference were presented, one based on adaptive interference cancelling for regular receive applications and one based on cross-correlation for spectrum sensing purposes.

The adaptive interference cancelling (AIC) approach works well when a good interference estimate can be generated. The less desired signal energy in the interference estimate the better the performance of the canceller: the signal-to-interference ratio (SIR) at the output of the canceller is approximately[2] equal to the interference-to-signal ratio (ISR) of the interference estimate.

In our proposed system, the interference estimate is based on two complex baseband signals with an accurate 45-degree phase difference and the same amplitudes. The better the phase and amplitude conditions are met, the better the desired signal is

[2]LMS misadjustment and non-dominant harmonic image band energy reduce the achievable rejection.

rejected and the higher the interference-to-signal ratio of the interference estimate. Thus, good analog design and layout practice is key.

The AIC harmonic rejection scheme works well: Measurements on a 65-nm CMOS front-end show that a single strong harmonic image band can be suppressed by over 80 dB without off-chip RF filtering. These figures were measured with a -66.1 dBm desired signal, a -20.1 dBm harmonic image and for 10 randomly selected chip. Under these conditions, the AIC scheme is able to decrease the harmonic image interference by more than two orders of magnitude (44 dB).

To explain these results, consider that the interference is 46 dB stronger than the desired signal at the antenna. The analog HR mixer stage provides approximately 40 dB of rejection. Thus, in the digital domain, the interference is roughly 6 dB stronger than the desired signal. If the desired signal is rejected by a practically achievable 35 dB when generating the interference estimate, the interference-to-signal ratio is around 41 dB. The best achievable signal-to-noise ratio at the output of the canceller is thus of the same order. This would result in a 46+41 = 87 dB harmonic rejection figure.

The interference estimate does not contain much even order harmonic image band energy. Because of this, the even order harmonic rejection figures cannot be increased with our proposed system. Introducing additional interference estimates[3] that do contain even order harmonic image energy will allow these to be cancelled. Simultaneous cancelling of the third and fifth order harmonic images is also possible by additional interference estimates.

Given the above, one can conclude that (adaptive) digital signal processing techniques can be an enabling technology to achieve harmonic rejection figures greater than 80 dB without using off-chip RF filters.

For spectrum sensing applications a cross-correlation method is proposed that uses two quadrature down-converter front-ends with a frequency offset. In contrast with the AIC methods for regular receive applications, the cross-correlation method can handle all harmonic images, including the even order harmonic image bands. The cross-correlation method was analyzed but not verified in a practical setting by the author. Recently, Dr. M. Oude Alink showed that this principle does indeed work in practice [23].

[3]This requires more LO phases and additional ADCs.

7.3 Original Contributions

This section briefly lists the original contributions of this work.

- A theoretical analysis of harmonic down-mixing in quadrature down-converters employing switching mixers was performed, leading to a baseband model describing their system-level behavior.
- Two methods for generating an interference estimate signal were presented. One method directly obtains the signal by using two different LO waveforms, the other indirectly produces the signal by post-processing two quadrature baseband signals having a 45-degree phase shift.
- A simple LMS-based algorithm to cancel the harmonic down-mixing interference, including its I/Q imbalanced image, was presented and tested using two different analog front-ends.
- A method based on cross-correlation and a frequency offset was introduced to reduce the sensitivity to the presence of harmonic images in spectrum sensing applications.
- A PC-based harmonic rejection signal processing backend was built that allows real-time monitoring of the harmonic rejection performance and the associated interference canceller parameters.

7.4 Future Work

The front-ends presented in this work are not yet fully developed. For instance, they do not have variable gain amplifiers (VGAs) to make sure the ADCs are driven within their optimal dynamic range. In effect, the RF to baseband gain is not signal dependent and neither were the gain imbalances. When VGAs are included, it is expected that the gain imbalances will also vary when the gain is varied. The current adaptive interference canceller will continually need to adapt to these changing imbalances. During the adaptation, the harmonic rejection will not be optimal. To reduce or even avoid this transitory period, the adaptive algorithm can be extended to incorporate the VGA gain settings and learn dependency of the filter coefficients as a function of the gain setting.

The work on interference cancelling was limited to an 8-phase system and two I/Q pairs. More harmonic image bands can simultaneously be cancelled when more distinct interference estimate signals are available. The additional interference estimates needed can be generated by increasing the number of phases. The number of I/Q pairs and phases could even be varied dynamically, depending on the interference scenario. This would benefit the power consumption of the system.

The harmonic rejection schemes presented here all assume that the amplitude imbalances are constant over the entire baseband spectrum. In systems with a relatively

large baseband bandwidth, such as ultra-wideband receivers, this assumption does not hold. To compensate the frequency dependent nature of these imbalances, the adaptive canceller must employ multi-tap, instead of single-tap, filters. The baseband gain variations are expected to vary slowly with frequency, which means that the number of taps needed is small. This hypothesis should be investigated further.

When increased overall harmonic rejection is required, the interference-to-signal (ISR) ratio of the interference estimate should be increased. The ISR is currently limited by the amplitude and phase relation accuracy between two baseband signals (IQ_1 and IQ_2) in the analog front-end. When the amplitude and phase errors are known, the 45-degree phase rotation block can be adjusted to compensate for them, thereby increasing the ISR. Measurement of the error can be done by injecting an RF signal in the desired signal band at the antenna. Given that IQ_1 and IQ_2 are sampled at the same time, the signal shape is irrelevant and need not be known but must occupy the desired signal band only; the phase and amplitude errors can be obtained by cross-correlation.

Appendix A

Mathematical derivations

A.1 Mean and variance of the sample variance estimator

The sample variance estimator of a sequence $x(n)$ drawn from a zero mean process X is defined as:

$$T: \frac{1}{N}\sum_{n=1}^{N} x^2(n), \tag{A.1}$$

where N is the number of samples in the sequence.

The mean of the sample variance estimator T is equal to the variance of X:

$$\begin{aligned}
\mathbf{E}\{T\} &= \mathbf{E}\left\{\frac{1}{N}\sum_{n=1}^{N} x^2(n)\right\} \\
&= \frac{1}{N}\sum_{n=1}^{N} \mathbf{E}\{x^2(n)\} \\
&= \mathbf{E}\{x^2\} \quad \text{if X is stationary} \\
&= \text{var}(x) \quad \text{if X is zero mean.}
\end{aligned} \tag{A.2}$$

The variance of an estimator is a quality measure. The variance of the sample variance estimator T is tends to zero as the number of samples in the sequence tends to infinity. Proving this is most easily done by transforming the sequence $x^2(n)$ into a new sequence consisting of two components: $y(n) = y_0(n) + \mu_y$, where μ_y is the variance of X and $y_0(n)$ is the zero-mean residual sequence. The sample variance estimator can now be conveniently rewritten as:

$$T: \frac{1}{N}\sum_{n=1}^{N} y_0(n) + \mu_y.$$

By definition, the variance of the estimator is given by:

$$\text{var}(T) = \mathbf{E}\{T^2\} - \mathbf{E}\{T\}^2, \tag{A.3}$$

in which the two expectations can be expanded as:

$$\begin{aligned}\mathbf{E}\{T\}^2 &= \mathbf{E}\left\{\frac{1}{N}\sum_{n=1}^{N}(y_0(n)+\mu_y)\right\}^2 \\ &= \left(\mu_y + \frac{1}{N}\sum_{n=1}^{N}\mathbf{E}\left\{y_0(n)\right\}\right)^2 \\ &= \mu_y^2\end{aligned} \tag{A.4}$$

and

$$\begin{aligned}\mathbf{E}\{T^2\} &= \mathbf{E}\left\{\frac{1}{N^2}\cdot\left(\sum_{n=1}^{N}y_0(n)+\mu_y\right)\cdot\left(\sum_{m=1}^{N}y_0(m)+\mu_y\right)\right\} \\ &= \frac{1}{N^2}\sum_{n=1}^{N}\sum_{m=1}^{N}\mathbf{E}\{y_0(n)\cdot y_0(m)\} + \dots \\ &\quad \frac{2}{N^2}\sum_{n=1}^{N}\sum_{n=1}^{N}\mathbf{E}\{y_0(n)\cdot\mu_y\} + \dots \\ &\quad \frac{1}{N^2}\sum_{n=1}^{N^2}\mu_y^2.\end{aligned} \tag{A.5}$$

Assuming the samples of $x(n)$ are independent, $y_0(n)$ are also independent, and the above result can be simplified to:

$$\mathbf{E}\{T^2\} = \mu_y^2 + \frac{1}{N}\mathbf{E}\left\{y_0^2\right\}, \tag{A.6}$$

which, together with (A.4) results in the following variance of the sample variance estimator:

$$\text{var}(T) = \frac{1}{N}\mathbf{E}\left\{y_0^2\right\}. \tag{A.7}$$

Finally, the variance of the estimator may be re-stated as a function of the original

variable x:

$$\begin{aligned}\mathrm{var}(T) &= \frac{1}{N}\mathbf{E}\left\{y_0^2\right\} \\ &= \frac{1}{N}\mathbf{E}\left\{(y-\mu_y)^2\right\} \\ &= \frac{1}{N}\left[\mathbf{E}\left\{y^2\right\} - 2\cdot\mu_y\cdot\mathbf{E}\left\{y\right\} + \mu_y^2\right] \\ &= \frac{1}{N}\left[\mathbf{E}\left\{x^4\right\} - 2\cdot\mathrm{var}(x)\cdot\mathbf{E}\left\{x^2\right\} + \mathrm{var}^2(x)\right] \\ &= \frac{1}{N}\left[\mathbf{E}\left\{x^4\right\} - \mathrm{var}^2(x)\right] \end{aligned} \tag{A.8}$$

When the process X is a zero-mean normally distributed process with variance σ^2, the variance of the sample variance estimator is equal to:

$$\frac{1}{N}\left(3\sigma^4 - \sigma^4\right) = \frac{2\sigma^4}{N}.$$

This outcome is in accordance with by numerical simulations done in MATLAB.

A.2 Stochastic gradient of the single-tap adaptive filter cost function

The single-tap adaptive filter used as an interference canceller is shown in Fig. A.1. A desired signal contaminated with interference, $r(n)$, enters the filter. The interference estimate, $v(n)$, is equalized (scaled and rotated in the complex plane) to the contaminating interference found in $r(n)$. A subtraction removes the interference, leaving the desired signal in the output of the interference canceller, $e(n)$

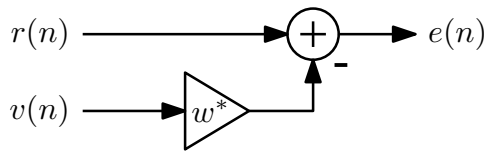

Figure A.1: The single-tap adaptive filter.

The stochastic cost function of the single-tap adaptive filter is given as the variance of $e(n)$ which can be expressed as[1]:

$$\begin{aligned}\mathbf{E}\{|e(n)|^2\} &= \mathbf{E}\{e(n)\cdot e^*(n)\} \\ &= \mathbf{E}\{(r(n) - w^*(n)\cdot v(n))\cdot(r^*(n) - w(n)\cdot v^*(n))\}, \end{aligned} \tag{A.9}$$

[1]This assumes that both $v(n)$ and $r(n)$ are drawn from zero-mean processes. If this is not the case, the signals must be preprocessed by a high-pass filter to make them zero mean.

This can be further rewritten as:

$$\begin{aligned}\mathbf{E}\{|e(n)|^2\} &= \mathbf{E}\{|r(n)|^2\} \\ &\quad - w^*(n) \cdot \mathbf{E}\{v(n) \cdot r^*(n)\} + w(n) \cdot \mathbf{E}\{v^*(n) \cdot r(n)\} \\ &\quad + |w(n)|^2 \cdot \mathbf{E}\{|v(n)|^2\}. \end{aligned} \tag{A.10}$$

To obtain the gradient, the above expression is split into a real and imaginary part and both parts are treated separately. Each part is differentiated with respect to the filter coefficient. After much manipulation, the following partial derivatives are obtained:

$$\begin{aligned}\frac{\partial}{\partial w_I(n)}\mathbf{E}\{|e(n)|^2\} &= -2 \cdot \Re\{\mathbf{E}\{v(n) \cdot r^*(n)\}\} + 2 \cdot w_I(n) \cdot \mathbf{E}\{|v(n)|^2\} \\ \frac{\partial}{\partial w_Q(n)}\mathbf{E}\{|e(n)|^2\} &= -2 \cdot \Im\{\mathbf{E}\{v(n) \cdot r^*(n)\}\} + 2 \cdot w_Q(n) \cdot \mathbf{E}\{|v(n)|^2\} \end{aligned} \tag{A.11}$$

The gradient is now simply:

$$\begin{aligned}\frac{\partial}{\partial w(n)}\mathbf{E}\{|e(n)|^2\} &= \frac{\partial}{\partial w_I(n)}\mathbf{E}\{|e(n)|^2\} + j \cdot \frac{\partial}{\partial w_Q(n)}\mathbf{E}\{|e(n)|^2\} \\ &= -2 \cdot \mathbf{E}\{v(n) \cdot r^*(n)\} + 2 \cdot w(n) \cdot \mathbf{E}\{|v(n)|^2\}. \end{aligned} \tag{A.12}$$

It is often more convenient to express this gradient in terms of $e(n)$. Remember that

$$e(n) = r(n) - w^*(n) \cdot v(n).$$

as shown in Fig. A.1 and that therefore

$$e^*(n) \cdot v(n) = v(n) \cdot r^*(n) - w(n)^* \cdot |v(n)|^2,$$

so that the gradient can also be written as:

$$\frac{\partial}{\partial w(n)}\mathbf{E}\{|e(n)|^2\} = 2 \cdot \mathbf{E}\{e^*(n) \cdot v(n)\}.$$

A.3 Steepest descent stability: the single-tap adaptive filter

The steepest descent algorithm weight update rule for the single-tap adaptive filter is:

$$w(n+1) = w(n) - 2\mu \cdot \left[w(n) \cdot \mathbf{E}\{|v(n)|^2\} - \mathbf{E}\{v(n) \cdot r^*(n)\}\right]. \tag{A.13}$$

which can be written as:

$$w(n+1) = c \cdot w(n) + 2\mu \cdot \mathbf{E}\{v(n) \cdot r^*(n)\}, \tag{A.14}$$

with

$$c = 1 - 2\mu \cdot \mathbf{E}\{|v(n)|^2\}.$$

This feedback system has a pole on the real axis at c. Thus, it must be within the unit circle to result in a stable system. In addition, integrator action is needed, which further restricts the pole location to the positive real half of the z-plane. Therefore, the steepest descent algorithm will converge if and only if:

$$0 < c < 1, \tag{A.15}$$

which gives:

$$0 < \mu < \frac{1}{2 \cdot \mathbf{E}\{|v(n)|^2\}} \tag{A.16}$$

A.4 Fourier series of a pulse wave

The effective waveforms of the harmonic rejection switching mixers are staircase shaped pulse waves. The Fourier coefficients of these waves are used in Chapter 3 to determine the mixer baseband response to the RF signals at its input.

The staircase shaped LO waveforms can be built using a summation of repeating pulses. One such pulse $f(t)$ is shown in Fig. A.2.

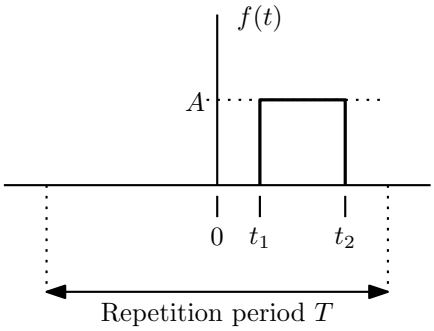

Figure A.2: A repeating rectangular pulse of amplitude A and with repetition time T. The defining period extents from -$\frac{T}{2}$ to $\frac{T}{2}$. The pulse starts at time t_1 and ends at t_2.

The Fourier series of a repeating waveform $f(t)$ that extends from $-\frac{T}{2}$ to $\frac{T}{2}$ is defined as:

$$F(n) = \frac{1}{T}\int_{-\frac{T}{2}}^{\frac{T}{2}} f(t)\cdot\exp\left(-j\cdot\frac{2\pi}{T}\cdot n\cdot t\right)\,dt, \tag{A.17}$$

where n is the harmonic number.

Reconstruction of the wave in the time domain is achieved by the inverse transform:

$$f(t) = \sum_{n=1}^{\infty}\left(F^*(n)\exp\left(-j\cdot 2\pi\frac{t}{T}n\right) + F(n)\exp\left(j\cdot 2\pi\frac{t}{T}n\right)\right)\ldots \\ + \text{DC offset}, \tag{A.18}$$

where '$*$' denotes the complex conjugate.

In case of the constant amplitude pulse shown in Fig. A.2, (A.17) can be simplified to:

$$F_{pulse}(n,t_1,t_2) = -\frac{A}{j\cdot 2\pi\cdot n}\left\{\exp\left(-j\frac{2\pi\cdot n\cdot t_1}{T}\right) - \exp\left(-j\frac{2\pi\cdot n\cdot t_2}{T}\right)\right\} \tag{A.19}$$

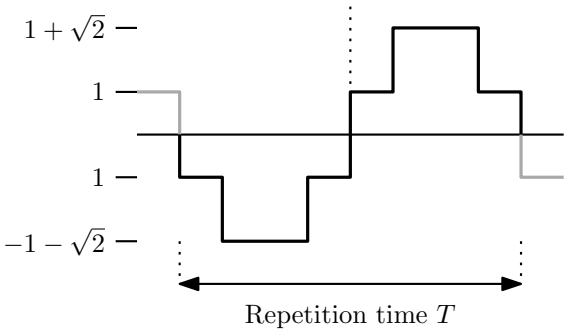

*Figure A.3: A staircase approximation to a sine wave using two amplitude levels (*1 *and* $1+\sqrt{2}$*). This shape forms the basis of the local oscillator waveform in Chapters 3 and 4.*

n	$F_{sin}(n)$	$F_{cos}(n)$
1	$-j \cdot 1.273240$	1.273240
2	0	0
3	0	0
4	0	0
5	0	0
6	0	0
7	$-j \cdot 0.181891$	-0.181891

Table A.1: Fourier series coefficients $F_{sin}(n)$ belonging to the waveform in Figure A.3 and the corresponding cosine wave (not shown) coefficients $F_{cos}(n)$.

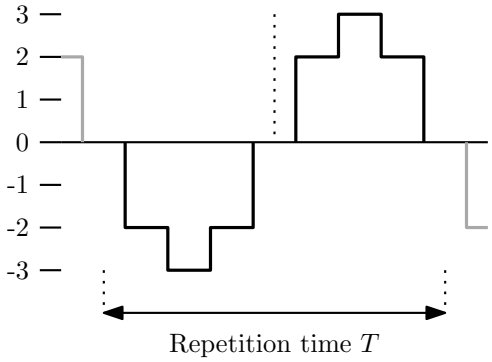

*Figure A.4: A staircase approximation to a sine wave using three amplitude levels (*0, 2 *and* 3*). This shape forms the basis of the local oscillator waveform in Chapter 5.*

n	$F_{sin}(n)$	$F_{cos}(n)$
1	$-j \cdot 1.419944$	1.419944
2	0	0
3	$j \cdot 0.033637$	0.033637
4	0	0
5	$-j \cdot 0.020182$	0.020182
6	0	0
7	$j \cdot 0.202849$	0.202849

Table A.2: Fourier series coefficients $F_{sin}(n)$ belonging to the waveform in Figure A.4 and the corresponding cosine wave (not shown) coefficients $F_{cos}(n)$.

Bibliography

[1] "IEEE standard for information technology–telecommunications and information exchange between systems local and metropolitan area networks–specific requirements part 11: Wireless LAN medium access control (MAC) and physical layer (PHY) specifications," *IEEE Std 802.11-2012 (Revision of IEEE Std 802.11-2007)*, pp. 1–2793, 2012.

[2] 3GPP members. (2013, Jun.) The 3GPP wireless specifications. [Online]. Available: http://www.3gpp.org/specifications

[3] J. Mitola, "The software radio architecture," *IEEE Commun. Mag.*, vol. 33, no. 5, pp. 26–38, 1995.

[4] R. Bagheri, A. Mirzaei, S. Chehrazi, M. E. Heidari, M. Lee, M. Mikhemar, W. Tang, and A. A. Abidi, "An 800-MHz-6-GHz Software-Defined Wireless Receiver in 90-nm CMOS," *IEEE J. Solid-State Circuits*, vol. 41, no. 12, pp. 2860–2276, Dec. 2006.

[5] V. Giannini, P. Nuzzo, C. Soens, K. Vengattaramane, M. Steyaert, J. Ryckaert, M. Goffioul, B. Debaillie, J. V. Driessche, J. Craninckx, and M. Ingels, "A 2mm2 0.1-to-5 GHz SDR receiver in 45nm digital CMOS." in *ISSCC Digest of technical papers*. IEEE, 2009, pp. 408–409.

[6] D. Manstretta, N. Laurenti, and R. Castello, "A reconfigurable narrow-band MB-OFDM UWB receiver architecture," *Circuits and Systems II: Express Briefs, IEEE Transactions on*, vol. 55, no. 4, pp. 324 –328, april 2008.

[7] R. R. A. Morton, "A simple d.c. to 10 Mc/s analogue multiplier," *Journal of Scientific Instruments*, vol. 43, no. 3, p. 165, 1966. [Online]. Available: http://stacks.iop.org/0950-7671/43/i=3/a=310

[8] Z. Ru, "Frequency translation techniques for interference-robust software-defined radio receivers," Ph.D. dissertation, University of Twente, 2009.

[9] M. Soer, "Switched-rc beamforming receivers in advanced cmos," Ph.D. dissertation, University of Twente, 2012.

[10] J. Mitola and G. Q. Maguire, "Cognitive radio: making software radios more personal," *Personal Communications, IEEE*, vol. 6, no. 4, pp. 13–18, Aug. 1999.

[11] J. Weldon, R. Narayanaswami, J. Rudell, L. Lin, M. Otsuka, S. Dedieu, L. Tee, K.-C. Tsai, C.-W. Lee, and P. Gray, "A 1.75-GHz highly integrated narrow-band CMOS transmitter with harmonic-rejection mixers," *Solid-State Circuits, IEEE Journal of*, vol. 36, no. 12, pp. 2003–2015, 2001.

[12] M. Gupta, S. Lerstaveesin, D. Kang, and B.-S. Song, "A 48-to-860MHz CMOS direct-conversion TV tuner," in *ISSCC Digest of technical papers*, 2007.

[13] F. Gatta, R. Gomez, Y. Shin, T. Hayashi, H. Zou, J. Y. C. Chang, L. Dauphinee, J. Xiao, D. S. H. Chang, T. H. Chih, M. Brandolini, D. Koh, B. J. J. Hung, T. Wu, M. Introini, G. Cusmai, L. Tan, B. Currivan, L. He, P. Cangiane, and P. Vorenkamp, "An embedded 65nm CMOS low-IF 48MHz-to-1GHz dual tuner for DOCSIS 3.0," in *Solid-State Circuits Conference - Digest of Technical Papers, 2009. ISSCC 2009. IEEE International*, 2009, pp. 122–123,123a.

[14] Z. Ru, E. A. M. Klumperink, G. Wienk, and B. Nauta, "A software-defined radio receiver architecture robust to out-of-band interference," in *Solid-State Circuits Conference - Digest of Technical Papers, 2009. ISSCC 2009. IEEE International*, 2009, pp. 230–231,231a.

[15] Z. Ru, E. A. M. Klumperink, B. Nauta, and H. Brekelmans, "Polyphase harmonic rejection mixer," Patent EP 091 000 095.0, February, 2009.

[16] M. Valkama, M. Renfors, and V. Koivunen, "Advanced methods for I/Q imbalance compensation in communication receivers," *Signal Processing, IEEE Transactions on*, vol. 49, no. 10, pp. 2335–2344, 2001.

[17] N. A. Moseley and C. H. Slump, "A low-complexity feed-forward I/Q imbalance compensation algorithm," in *17th Annual Workshop on Circuits, Veldhoven, The Netherlands*. Utrecht: Technology Foundation STW, November 2006, pp. 158–164.

[18] E. Keehr and A. Hajimiri, "Equalization of im3 products in wideband direct-conversion receivers," in *Solid-State Circuits Conference, 2008. ISSCC 2008. Digest of Technical Papers. IEEE International*, 2008, pp. 204–607.

[19] S.-Y. Lee, Y.-S. Lee, S.-H. Hong, H.-S. Choi, and Y.-H. Jeong, "An adaptive predistortion rf power amplifier with a spectrum monitor for multicarrier wcdma applications," *Microwave Theory and Techniques, IEEE Transactions on*, vol. 53, no. 2, pp. 786–793, 2005.

[20] R. N. Ghose, *Interference Mitigation*. IEEE Press, 1996.

[21] IEEE. (2013, Jun.) The IEEE online digital library. [Online]. Available: http://ieeexplore.ieee.org

[22] T. Yamaji, J. Matsuno, H. Aoyama, M. Furuta, T. Takida, I. Akita, A. Kuroda, T. Itakura, and N. Itoh, "A 6-phase harmonic rejection down-converter with digital assist," in *VLSI Circuits (VLSIC), 2010 IEEE Symposium on*, 2010, pp. 181–182.

[23] M. Oude Alink, A. Kokkeler, E. Klumperink, Z. Ru, W. Cheng, and B. Nauta, "Improving harmonic rejection for spectrum sensing using crosscorrelation," in *ESSCIRC (ESSCIRC), 2012 Proceedings of the*, 2012, pp. 361–364.

[24] Z. Ru, E. A. M. Klumperink, and B. Nauta, "A discrete-time mixing receiver architecture with wideband harmonic rejection," in *ISSCC Digest of technical papers*, Feb. 2008.

[25] S. Haykin, *Adaptive filter theory*, 4th ed. Upper Saddle River, NJ, USA: Prentice Hall, 2002.

[26] S. M. Kuo and D. R. Morgan, *Active Noise Control Systems*. Wiley Interscience, 1996.

[27] M. C. Jeruchim, P. Balaban, and K. S. Shanmugan, Eds., *Simulation of Communication Systems: Modeling, Methodology and Techniques*, 2nd ed. Norwell, MA, USA: Kluwer Academic Publishers, 2000.

[28] W. Tranter, *Principles of communication systems simulation with wireless applications*. Upper Saddle River, NJ, USA: Prentice Hall, 2004.

[29] A. Carlson, *Communication systems: an introduction to signals and noise in electrical communication*, 3rd ed. McGraw-Hill, 1986.

[30] J. D. Foley, A. van Dam, S. K. Feiner, and J. F. Hughes, *Computer graphics: principles and practice (2nd ed.)*. Boston, MA, USA: Addison-Wesley Longman Publishing Co., Inc., 1990.

[31] S. Haykin, *Unsupervised Adaptive Filtering: Blind deconvolution*. Wiley, 2000.

[32] M. Valkama, M. Renfors, and V. Koivunen, "Advanced methods for I/Q imbalance compensation in communication receivers," *IEEE Trans. Signal Process.*, vol. 49, no. 10, pp. 2355–2344, Oct. 2001.

[33] E. Cho and M. J. Cho, "Variance of the sample variance," in *Proceedings of the Joint Statistical Meetings*, vol. Section on Survey Research Methods. American Statistical Association, 2008, pp. 1291–1293.

[34] B. Widrow et al., "Adaptive noise cancelling: Principles and applications," *Proc. IEEE*, vol. 63, no. 12, pp. 1692–1717, Dec 1975.

[35] N. Moseley, E. A. M. Klumperink, and B. Nauta, "A two-stage approach to harmonic rejection mixing using blind interference cancellation," *Circuits and Systems II: Express Briefs, IEEE Transactions on*, vol. 55, no. 10, pp. 966–970, 2008.

[36] J.R. Tourret et al., "Sip tuner with integrated LC tracking filter for both cable and terrestrial TV reception," *Solid-State Circuits, IEEE Journal of*, vol. 42, no. 12, pp. 2809–2821, Dec. 2007.

[37] E. Klumperink, R. Shrestha, E. Mensink, V. Arkesteijn, and B. Nauta, "Cognitive radios for dynamic spectrum access - polyphase multipath radio circuits for dynamic spectrum access," *Communications Magazine, IEEE*, vol. 45, no. 5, pp. 104–112, May 2007.

[38] J. A. Weldon, R. S. Narayanaswami, J. C. Rudell, L. Lin, M. Otsuka, S. Dedieu, L. Tee, K.-C. Tsai, C.-W. Lee, and F. Paul R. Gray, "A 1.75-GHz highly integrated narrow-band CMOS transmitter with harmonic-rejection mixers," *IEEE J. Solid-State Circuits*, vol. 36, no. 12, pp. 2003–2015, Dec. 2001.

[39] R. C. H. van de Beek, E. A. M. Klumperink, C. S. Vaucher, and B. Nauta, "Low-jitter clock multiplication: A comparison between PLLs and DLLs," *IEEE Trans. Circuits Syst. II*, vol. 49, no. 8, pp. 555–566, Aug. 2002.

[40] M. Windisch and G. Fettweis, "Blind estimation and compensation of I/Q imbalance in OFDM receivers with enhancements through kalman filtering," *Statistical Signal Processing, 2007. SSP '07. IEEE/SP 14th Workshop on*, pp. 754–758, 26-29 Aug. 2007.

[41] E. A. M. Klumperink and B. Nauta, "Systematic comparison of HF CMOS transconductors," *IEEE Trans. Circuits Syst. II*, vol. 50, no. 10, pp. 728–741, Oct. 2003.

[42] Y. Huang, J. Benesty, and J. Chen, *Acoustic MIMO Signal Processing.* Springer, 2006.

[43] N. Moseley, E. A. M. Klumperink, and B. Nauta, "Experimental verification of a harmonic-rejection mixing concept using blind interference canceling," in *Wireless Technology, 2008. EuWiT 2008. European Conference on*, 2008, pp. 210–213.

[44] A. A. Abidi, "Direct-conversion radio transceivers for digital communications," *IEEE Trans. Syst. Sci. Cybern.*, vol. 30, no. 12, pp. 1399–1410, Dec 1995.

[45] Z. Ru, N. Moseley, E. A. M. Klumperink, and B. Nauta, "Digitally enhanced software-defined radio receiver robust to out-of-band interference," *Solid-State Circuits, IEEE Journal of*, vol. 44, no. 12, pp. 3359–3375, 2009.

[46] V. Giannini, P. Nuzzo, C. Soens, K. Vengattaramane, M. Steyaert, J. Ryckaert, M. Goffioul, B. Debaillie, J. Van Driessche, J. Craninckx, and M. Ingels, "A 2mm2 0.1-to-5GHz SDR receiver in 45nm digital CMOS," in *Solid-State Circuits Conference - Digest of Technical Papers, 2009. ISSCC 2009. IEEE International*, 2009, pp. 408–409.

[47] R. Bagheri, A. Mirzaei, S. Chehrazi, M. Heidari, M. Lee, M. Mikhemar, W. Tang, and A. Abidi, "An 800-MHz to 6-GHz software-defined wireless receiver in 90-nm CMOS," *Solid-State Circuits, IEEE Journal of*, vol. 41, no. 12, pp. 2860–2876, 2006.

[48] S. Lerstaveesin, M. Gupta, D. Kang, and B.-S. Song, "A 48 to 860 MHz CMOS low-IF direct-conversion DTV tuner," *Solid-State Circuits, IEEE Journal of*, vol. 43, no. 9, pp. 2013–2024, 2008.

[49] S. Blaakmeer, E. A. M. Klumperink, D. M. W. Leenaerts, and B. Nauta, "The blixer, a wideband balun-LNA-I/Q-mixer topology," *Solid-State Circuits, IEEE Journal of*, vol. 43, no. 12, pp. 2706–2715, 2008.

[50] D. Leenaerts, R. van de Beek, J. Bergervoet, H. Kundur, G. Van Der Weide, A. Kapoor, T. Y. Pu, Y. Fang, Y. J. Wang, B. Mukkada, H. S. Lim, M. Kiran, C. S. Lim, S. Badiu, and A. Chang, "A 65nm CMOS inductorless triple-band-group WiMedia UWB PHY," in *Solid-State Circuits Conference - Digest of Technical Papers, 2009. ISSCC 2009. IEEE International*, 2009, pp. 410–411,411a.

[51] D. Manstretta, N. Laurenti, and R. Castello, "A reconfigurable narrow-band MB-OFDM UWB receiver architecture," *Circuits and Systems II: Express Briefs, IEEE Transactions on*, vol. 55, no. 4, pp. 324–328, 2008.

[52] T. Sowlati *et al.*, "Single-chip multiband WCDMA/HSDPA/HSUPA/EGPRS transceiver with diversity receiver and 3G DigRF interface without SAW filters in transmitter / 3G receiver paths," in *Solid-State Circuits Conference - Digest of Technical Papers, 2009. ISSCC 2009. IEEE International*, 2009, pp. 116–117,117a.

[53] O. Gaborieau, S. Mattisson, N. Klemmer, B. Fahs, F. Braz, R. Gudmundsson, T. Mattsson, C. Lascaux, C. Trichereau, W. Suter, E. Westesson, and A. Nydahl, "A SAW-less multiband WEDGE receiver," in *Solid-State Circuits Conference - Digest of Technical Papers, 2009. ISSCC 2009. IEEE International*, 2009, pp. 114–115,115a.

[54] V. Aparin and L. Larson, "Modified derivative superposition method for linearizing FET low-noise amplifiers," *Microwave Theory and Techniques, IEEE Transactions on*, vol. 53, no. 2, pp. 571–581, 2005.

[55] W.-H. Chen, G. Liu, B. Zdravko, and A. Niknejad, "A highly linear broadband CMOS LNA employing noise and distortion cancellation," *Solid-State Circuits, IEEE Journal of*, vol. 43, no. 5, pp. 1164–1176, 2008.

[56] E. A. M. Klumperink and B. Nauta, "Systematic comparison of HF CMOS transconductors," *Circuits and Systems II: Analog and Digital Signal Processing, IEEE Transactions on*, vol. 50, no. 10, pp. 728–741, 2003.

[57] H. Darabi, "A blocker filtering technique for SAW-less wireless receivers," *Solid-State Circuits, IEEE Journal of*, vol. 42, no. 12, pp. 2766–2773, 2007.

[58] Z. Ru, E. A. M. Klumperink, and B. Nauta, "A discrete-time mixing receiver architecture with wideband harmonic rejection," in *Solid-State Circuits Conference, 2008. ISSCC 2008. Digest of Technical Papers. IEEE International*, 2008, pp. 322–616.

[59] N. Moseley, Z. Ru, E. A. M. Klumperink, and B. Nauta, "A 400-to-900 MHz receiver with dual-domain harmonic rejection exploiting adaptive interference cancellation," in *Solid-State Circuits Conference - Digest of Technical Papers, 2009. ISSCC 2009. IEEE International*, 2009, pp. 232–233,233a.

[60] N. Moseley, E. A. M. Klumperink, and B. Nauta, "A two-stage approach to harmonic rejection mixing using blind interference cancellation," *Circuits and Systems II: Express Briefs, IEEE Transactions on*, vol. 55, no. 10, pp. 966–970, 2008.

[61] B. Razavi, *RF microelectronics*. Upper Saddle River, NJ, USA: Prentice-Hall, Inc., 1998.

[62] W. Redman-White and D. M. W. Leenaerts, "1/f noise in passive cmos mixers for low and zero if integrated receivers," in *Solid-State Circuits Conference, 2001. ESSCIRC 2001. Proceedings of the 27th European*, 2001, pp. 41–44.

[63] M. Valla, G. Montagna, R. Castello, R. Tonietto, and I. Bietti, "A 72-mw cmos 802.11a direct conversion front-end with 3.5-db nf and 200-khz 1/f noise corner," *Solid-State Circuits, IEEE Journal of*, vol. 40, no. 4, pp. 970–977, 2005.

[64] D. Kaczman, M. Shah, M. Alam, M. Rachedine, D. Cashen, L. Han, and A. Raghavan, "A single-chip 10-band WCDMA/HSDPA 4-band GSM/EDGE SAW-less CMOS receiver with DigRF 3G interface and + 90 dBm IIP2," *Solid-State Circuits, IEEE Journal of*, vol. 44, no. 3, pp. 718–739, 2009.

[65] B. Razavi, *Design of Analog CMOS Integrated Circuits*, 1st ed. New York, NY, USA: McGraw-Hill, Inc., 2001.

[66] T. H. Lee, *The Design of CMOS Radio-Frequency Integrated Circuits*. Cambridge University Press, 2004.

[67] Z. Ru, "Frequency-translation techniques for interference-robust software-defined radio receivers in CMOS," Ph.D. dissertation, University of Twente, The Netherlands, 2009.

[68] S. Rabii and B. Wooley, "A 1.8-V digital-audio sigma-delta modulator in 0.8-μm CMOS," *Solid-State Circuits, IEEE Journal of*, vol. 32, no. 6, pp. 783–796, 1997.

[69] A. Maxim, R. Poorfard, M. Reid, J. Kao, C. Thompson, and R. Johnson, "A DDFS driven mixing-DAC with image and harmonic rejection capabilities," in *Solid-State Circuits Conference, 2008. ISSCC 2008. Digest of Technical Papers. IEEE International*, 2008, pp. 372–621.

[70] H.-K. Cha, S.-S. Song, H.-T. Kim, and K. Lee, "A CMOS harmonic rejection mixer with mismatch calibration circuitry for digital TV tuner applications," *Microwave and Wireless Components Letters, IEEE*, vol. 18, no. 9, pp. 617–619, 2008.

[71] N. Moseley, E. Klumperink, and B. Nauta, "A spectrum sensing technique for cognitive radios in the presence of harmonic images," in *New Frontiers in Dynamic Spectrum Access Networks, 2008. DySPAN 2008. 3rd IEEE Symposium on*, 2008, pp. 1–10.

[72] P. P. Vaidyanathan, *Multirate Systems and Filter Banks*. Prentice Hall, 1993.

[73] B. Farhang-Boroujeny, "Filter bank spectrum sensing for cognitive radios," *IEEE Trans. Signal Process.*, vol. 56, no. 5, pp. 1801–1811, May 2008.

[74] A. Nuttall, "Some windows with very good sidelobe behavior," *IEEE Trans. Acoust., Speech, Signal Process.*, vol. 29, no. 1, pp. 84–91, Feb 1981.

[75] Z. Ru, E. Klumperink, G. Wienk, and B. Nauta, "A software-defined radio receiver architecture robust to out-of-band interference." in *ISSCC Digest of technical papers*. IEEE, 2009, pp. 230–231.

List of Publications

N. A. Moseley and C. H. Slump. A low-complexity feed-forward i/q imbalance compensation algorithm. In *17th Annual Workshop on Circuits, Veldhoven, The Netherlands*, pages 158–164, Utrecht, November 2006. Technology Foundation STW.

N.A. Moseley, E. A M Klumperink, and B. Nauta. Experimental verification of a harmonic-rejection mixing concept using blind interference canceling. In *Wireless Technology, 2008. EuWiT 2008. European Conference on*, pages 210–213, 2008.

N.A. Moseley, E. A M Klumperink, and B. Nauta. A spectrum sensing technique for cognitive radios in the presence of harmonic images. In *New Frontiers in Dynamic Spectrum Access Networks, 2008. DySPAN 2008. 3rd IEEE Symposium on*, pages 1–10, 2008.

N.A. Moseley, E. A M Klumperink, and B. Nauta. A two-stage approach to harmonic rejection mixing using blind interference cancellation. *Circuits and Systems II: Express Briefs, IEEE Transactions on*, 55(10):966–970, 2008.

N.A. Moseley, Z. Ru, E. A M Klumperink, and B. Nauta. A 400-to-900 MHz receiver with dual-domain harmonic rejection exploiting adaptive interference cancellation. In *Solid-State Circuits Conference - Digest of Technical Papers, 2009. ISSCC 2009. IEEE International*, pages 232–233,233a, 2009.

Z. Ru, N.A. Moseley, E. A M Klumperink, and B. Nauta. Digitally enhanced software-defined radio receiver robust to out-of-band interference. *Solid-State Circuits, IEEE Journal of*, 44(12):3359–3375, 2009.

R. Schiphorst, N.A. Moseley, A.C. Aarden, M. Heskamp, and Cornelis H. Slump. A T-DAB field trial using a low-mast infrastructure. *Broadcasting, IEEE Transactions on*, 54(3):356–370, 2008.

Acknowledgements

The thesis before you is the result of a long journey during which many people contributed and helped me along the way.

First, I would like to thank my daily supervisor, Eric Klumperink, for his constructive criticism, support and patience over the years. I would also like to thank Zhiyu Ru, who was assigned to the WiCOMM project together with me. You did a smashing job designing the harmonic rejection analog front-end! Thank you for letting me use it. I'm sorry we could not present our work at the ISSCC together due to politics.

Furthermore, many thanks go to Prof. Bram Nauta who, despite a very busy schedule, always found time to read my papers or to discuss things. I would also like to thank the staff and students of the Integrated Circuit Design group for the excellent working environment, specifically Gerard Wienk for the PCB design, Henk de Vries for keeping the lab up and running and Gerdien Lammers for making sure things get done.

Then I would like to thank my office mates who had to deal with my idiosyncrasies; Fabian van Houwelingen and Xiang Gao. It was a pleasure.

Of course, this work would have never been possible without Tupewo Samyl. Thank you for your selflessness.

Special thanks to Dr. Nirvana Meratnia and Prof. Paul Havinga of the Pervasive Systems group for providing me with the final push and time to finish my thesis.

This acknowledgement would not be complete without mentioning Prof. Kees Slump, who was instrumental in getting me started on my journey, which I greatly appreciate.

Last but by no stretch least, a great many thanks to you, Joyce Dakhorst, for being who you are.